



Terms and Conditions of Use of Digitised Theses from Trinity College Library Dublin

Copyright statement

All material supplied by Trinity College Library is protected by copyright (under the Copyright and Related Rights Act, 2000 as amended) and other relevant Intellectual Property Rights. By accessing and using a Digitised Thesis from Trinity College Library you acknowledge that all Intellectual Property Rights in any Works supplied are the sole and exclusive property of the copyright and/or other IPR holder. Specific copyright holders may not be explicitly identified. Use of materials from other sources within a thesis should not be construed as a claim over them.

A non-exclusive, non-transferable licence is hereby granted to those using or reproducing, in whole or in part, the material for valid purposes, providing the copyright owners are acknowledged using the normal conventions. Where specific permission to use material is required, this is identified and such permission must be sought from the copyright holder or agency cited.

Liability statement

By using a Digitised Thesis, I accept that Trinity College Dublin bears no legal responsibility for the accuracy, legality or comprehensiveness of materials contained within the thesis, and that Trinity College Dublin accepts no liability for indirect, consequential, or incidental, damages or losses arising from use of the thesis for whatever reason. Information located in a thesis may be subject to specific use constraints, details of which may not be explicitly described. It is the responsibility of potential and actual users to be aware of such constraints and to abide by them. By making use of material from a digitised thesis, you accept these copyright and disclaimer provisions. Where it is brought to the attention of Trinity College Library that there may be a breach of copyright or other restraint, it is the policy to withdraw or take down access to a thesis while the issue is being resolved.

Access Agreement

By using a Digitised Thesis from Trinity College Library you are bound by the following Terms & Conditions. Please read them carefully.

I have read and I understand the following statement: All material supplied via a Digitised Thesis from Trinity College Library is protected by copyright and other intellectual property rights, and duplication or sale of all or part of any of a thesis is not permitted, except that material may be duplicated by you for your research use or for educational purposes in electronic or print form providing the copyright owners are acknowledged using the normal conventions. You must obtain permission for any other use. Electronic or print copies may not be offered, whether for sale or otherwise to anyone. This copy has been supplied on the understanding that it is copyright material and that no quotation from the thesis may be published without proper acknowledgement.

**Studies of the Oxidation of Mo(110): A
Method for Nanowire Growth**

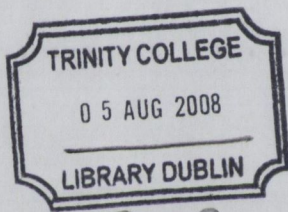
Kevin Patrick Radican

A thesis submitted to the University of Dublin, Trinity College

in partial fulfillment of the requirements for the degree of

Doctor of Philosophy

October 2007

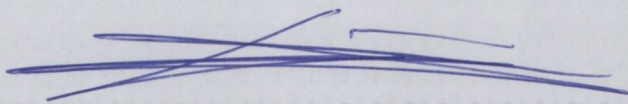


THOSIS
8514.

Declaration

I, the undersigned, declare that this work has not previously been submitted to this or any other University, and that unless otherwise stated, it is entirely my own work.

I, the undersigned, agree that Trinity College Library may lend or copy this thesis upon request.



Kevin Patrick Radican

Dated: October 2007



Summary

In this dissertation the oxidation of the molybdenum (110) surface was studied at 900 and 1000 °C and 1×10^{-6} Torr oxygen pressure. Through the use of low energy electron diffraction (LEED), Auger electron spectroscopy (AES), scanning tunneling microscopy (STM) and density functional theory (DFT) we have fully characterised the growth of the surface oxide phase as well as the 3-D oxide growth. It was found that a bulk-like surface oxide of MoO₂ (010) grows epitaxially on the surface at 1000 °C and 1×10^{-6} Torr oxygen pressure. LEED and STM data were used to give a detailed analysis of the oxide surface structure. From this experimental data, a model was built and through the use of DFT calculations, we showed that a strained bulk-like MoO₂(010) film is in excellent agreement with the experimental data.

Furthermore, it was found that while this oxide phase readily grew into thicker 3-dimensional MoO₂ single crystalline thin films, only the surface oxide was stable up to 1000 °C in ultra high vacuum (UHV). This indicates that there is an increase in thermodynamic stability given by the adhesion energy. The origin of this strong adhesion between the film and substrate can be related to the charge redistribution at the interface. An electron density difference map of the interface is used to illustrate the charge redistribution for this system. Furthermore, we employed DFT

calculations to estimate the work of adhesion for this system and there is indeed a strong interaction between the film and substrate as expected. The calculated work of adhesion was around 7 J / m^2 .

By continuing to anneal this surface at $900 \text{ }^\circ\text{C}$ and 1×10^{-6} Torr oxygen, MoO_2 nanowires begin to form. These wires grow at a constant rate until a maximum size of $\sim 30 \text{ nm}$ by $\sim 6 \text{ nm}$ is reached. Through the use of LEED, AES, STM and DFT we have fully characterised the growth of these wires. The general idea is that the initial MoO_2 (010) layer is close enough to the interface such that a charge redistribution at the interface can sufficiently modify the surface charge density and stabilize the film. This effect is such that the film fully wets the substrate. As the oxide grows thicker however, this (010) oxide surface orientation can be classified as a polar, Tasker type III surface, and requires a surface modification to be energetically favourable.

As this film continues to grow it develops various sizes of nanowires and eventually transforms into a periodically faceted surface made of MoO_2 (0 2 1) and (0 2 -1) faces. Using DFT calculations, we show that this faceted surface has a lower surface free energy than the initial growth orientation. Furthermore, with the use of the theory of periodically faceted surfaces, we show that it is likely that the periodicity of the facets is related to the equilibrium state for this surface.

We also show that the oxidation rate of MoO_2 on $\text{Mo}(110)$ under these conditions is linear. With the use of the Cabrera and Mott theory of the oxidation of metals we show that this linear rate is most likely related to the rate of adsorption or dissociation of oxygen at the surface of the MoO_2 .

Furthermore, we show that magnetron sputtered $\text{Mo}(110)$ thin films

grown on Al_2O_3 can be of high quality. These films show promise for the production of MoO_2 nanowires on an insulating substrate.

Acknowledgements

First I would like to thank my thesis adviser, Prof. Igor V. Shvets for the opportunity and support I have received during my dissertation research. Also, I would sincerely like to thank my friends and colleagues of the Nanomag group, Dr. Giuseppe Manai, Dr. Roman Kantor, Dr. Nikolai Berdunov, and Dr. Shane Murphy for their encouragement and help in completing my research. I also have to thank everyone in the Physics Dept. at Trinity College, for they have made a warm and friendly environment to work in.

I am extremely grateful to my parents for their never ending help and support. I must also thank their friend Michael Schwarz for his invaluable advice "stay in school as long as you can!" And I have.

I would also like to thank everyone that proofread the text to fix all of my dodgy Texas English, and to Nikolai Berdunov for fixing my dodgy Texas Physics.

Throughout the course of this work, all work and no play would make Kevin go crazy. I especially I have to thank Dr. G Manai for being ready at any moment of SUN! for a trip to the Pav to restore our Iron and vitamin D levels. Dr. Roman Kantor, who was the only one around late at night when all the real work gets done, was always willing to make it to the pub for "just one" at last call. I am also grateful for Dr. Brian

Jester, who not only drove across Britain to collect me and my dog in London, was always up for some good old American style fun. Lastly, I would like to thank all of my climbing friends, the parties and climbing trips were always a welcomed escape.

I am also grateful to my PhD examiners for the time they will spend reading and correcting the thesis.

Some of the calculations in this thesis were made with the computing facilities at Trinity Centre for High Performance Computing. I would like to thank the staff at TCHPC, especially Jimmy Tang, as well as their supporters IITAC, the HEA, the National Development Plan and the Trinity Centre for High Performance Computing.

The research described in this dissertation has been sponsored in part through SFI and CRANN.

For those who might follow in my footsteps in Igor's group, I hope you will find something helpful to you in this Thesis.

Kevin Patrick Radican

University of Dublin, Trinity College

October 2007

Contents

Summary	v
Acknowledgements	ix
List of Tables	xvii
List of Figures	xix
Chapter 1 Introduction	1
1.1 Motivation	1
1.2 Organization	3
Bibliography	5
I Instrumentation and Theory	7
Chapter 2 Description of the Experimental Techniques and the Ultra High Vacuum System	9
2.1 Auger Electron Spectroscopy	9
2.2 Low Energy Electron Diffraction	10
2.3 Scanning Tunneling Microscopy	15
2.3.1 Theory of Tunneling Effect	16
2.3.2 The Scanning Tunneling Microscope	19

2.4	DC Magnetron Sputtering	20
2.5	Ultra-high vacuum	22
2.5.1	Vacuum requirements	22
2.5.2	Pumping	24
2.6	The UHV System	28
2.7	The Preparation Chamber	29
2.7.1	The resistive heater	30
2.7.2	The e ⁻ -beam heater	31
2.7.3	The Ar ⁺ ion gun	32
2.8	Auger Electron Spectroscopy Set-Up	33
2.9	Low Energy Electron Diffraction	34
2.10	The Room Temperature STM	36
2.10.1	Modifications to STM	37
2.10.2	STM Tips	39
	Bibliography	41
Chapter 3 Density Functional Theory		43
3.1	Born-Oppenheimer Approximation and Bloch's Theorem	44
3.2	Hohenberg-Kohn Theorem	46
3.3	Kohn-Sham (KS) Equations	47
3.3.1	Local Density Approximation	50
3.3.2	Exchange-Correlation	51
3.4	Pseudopotential Theory	52
3.4.1	Projector Augmented-Wave Method	52
3.5	Relaxation of the Ionic System	54
3.5.1	The Hellmann-Feynman Theorem	55
	Bibliography	57

Chapter 4 Oxidation Theory	58
4.1 The Oxidation Process	59
4.1.1 Oxygen Adsorption	59
4.1.2 Oxygen Incorporation	61
4.1.3 Oxide Nucleation and Growth	62
4.2 Oxide Film Growth	63
4.3 Rate Limiting Models for Oxidation Processes	65
4.3.1 Ion and Electron Current Density	66
4.3.2 The Electronic Tunnel Current	67
4.3.3 The Thermal Electron Current	69
4.3.4 The Current For Ion Diffusion	71
4.4 Linear Rate Laws	74
4.4.1 Deal and Grove Rate Law	74
4.4.2 Surface-Controlled Linear Growth	76
4.5 Oxidation Studies of Molybdenum	77
Bibliography	79

II Experimental Results 81

Chapter 5 Background	83
5.1 Molybdenum	83
5.1.1 The Mo(110) Surface	84
5.2 MoO ₂	87
5.2.1 Crystal Structure	87
5.2.2 Electronic Structure	89
5.2.3 Calculated Electronic Density of States and Band Structure of MoO ₂	91
5.3 The Optical Properties of MoO ₂	94

5.3.1	DFT Calculated Optical Spectra of MoO ₂	94
	Bibliography	97
Chapter 6	Surface Oxide Growth on Mo(110)	98
6.1	Experimental Procedure	99
6.2	Experimental Results	99
6.2.1	LEED Analysis	99
6.2.2	STM Analysis	101
6.2.3	MoO ₂ Surface Oxide Model	103
6.3	DFT Calculations	108
6.3.1	DFT Geometry Optimization	109
6.3.2	DFT STM Simulations	113
	Bibliography	116
Chapter 7	Formation of MoO₂ Nanowires on Mo(110)	118
7.1	Experimental Procedure	119
7.2	Experimental Results	120
7.2.1	STM Analysis	121
7.2.2	Auger Data	121
7.2.3	LEED Analysis	124
7.2.4	LEED Spot Splitting	125
7.3	Nanowire Model	128
7.3.1	Surface Energy Calculations	132
7.3.2	Theory of Periodic Faceting	133
	Bibliography	137
Chapter 8	The Oxidation Rate of MoO₂	139
	Bibliography	148

Chapter 9 MoO₂ Nanowire Growth on Mo(110)/Al₂O₃(11-	149
20)	
9.1 Mo Film Growth	150
9.2 Film Characterisation	150
9.3 MoO ₂ Wires Grown on Mo(110)/Al ₂ O ₃	156
Bibliography	160
Chapter 10 Conclusions and Future Work	161
10.1 Conclusions	161
10.2 Future Work	164
Appendix 1	165
Publication List	166

List of Tables

2.1	Various ranges of vacuum	22
2.2	n , λ , R and τ_m at various P for N_2 at 300 K	24
5.1	Wyckoff positions of the atoms in the MoO_2 unit cell. . .	88
5.2	Dimensions of the bulk MoO_2 unit cell.	88
5.3	Atomic positions of the Mo and O atoms in the bulk MoO_2 crystal.	89
5.4	Dimensions of the MoO_2 unit cell after DFT relaxation. .	90
5.5	Atomic positions of the Mo and O atoms after DFT relax- ation of the MoO_2 crystal.	90
6.1	DFT Geometry Calculations	111
7.1	The percent concentration on Mo and O from Auger of an MoO_2 oxide film.	124
7.2	DFT Calculated surface energy.	133
9.1	Auger Concentrations	152
9.2	Auger Concentrations	155

List of Figures

1.1	Introduction	1
1.2	Background	2
1.3	Methodology	3
1.4	Results	4
1.5	Discussion	5
1.6	Conclusion	6
1.7	References	7
1.8	Appendix	8
1.9	Index	9
1.10	Summary	10
1.11	Notes	11
1.12	Footnotes	12
1.13	Tables	13
1.14	Figures	14
1.15	References	15
1.16	Appendix	16
1.17	Index	17
1.18	Summary	18
1.19	Notes	19
1.20	Footnotes	20
1.21	Tables	21
1.22	Figures	22
1.23	References	23
1.24	Appendix	24
1.25	Index	25
1.26	Summary	26
1.27	Notes	27
1.28	Footnotes	28
1.29	Tables	29
1.30	Figures	30
1.31	References	31
1.32	Appendix	32
1.33	Index	33
1.34	Summary	34
1.35	Notes	35
1.36	Footnotes	36
1.37	Tables	37
1.38	Figures	38
1.39	References	39
1.40	Appendix	40
1.41	Index	41
1.42	Summary	42
1.43	Notes	43
1.44	Footnotes	44
1.45	Tables	45
1.46	Figures	46
1.47	References	47
1.48	Appendix	48
1.49	Index	49
1.50	Summary	50
1.51	Notes	51
1.52	Footnotes	52
1.53	Tables	53
1.54	Figures	54
1.55	References	55
1.56	Appendix	56
1.57	Index	57
1.58	Summary	58
1.59	Notes	59
1.60	Footnotes	60
1.61	Tables	61
1.62	Figures	62
1.63	References	63
1.64	Appendix	64
1.65	Index	65
1.66	Summary	66
1.67	Notes	67
1.68	Footnotes	68
1.69	Tables	69
1.70	Figures	70
1.71	References	71
1.72	Appendix	72
1.73	Index	73
1.74	Summary	74
1.75	Notes	75
1.76	Footnotes	76
1.77	Tables	77
1.78	Figures	78
1.79	References	79
1.80	Appendix	80
1.81	Index	81
1.82	Summary	82
1.83	Notes	83
1.84	Footnotes	84
1.85	Tables	85
1.86	Figures	86
1.87	References	87
1.88	Appendix	88
1.89	Index	89
1.90	Summary	90
1.91	Notes	91
1.92	Footnotes	92
1.93	Tables	93
1.94	Figures	94
1.95	References	95
1.96	Appendix	96
1.97	Index	97
1.98	Summary	98
1.99	Notes	99
1.100	Footnotes	100

List of Figures

2.1	Schematic of the Auger emission process	11
2.2	Schematic of the Bragg condition for a 1D lattice.	12
2.3	Schematic of the Ewald sphere construction.	14
2.4	Schematic of the tunneling process.	17
2.5	Diagram of a Magnetron sputtering set-up	21
2.6	Top view schematic of the ultra high vacuum (UHV) system.	29
2.7	Schematic illustration of the resistive heater	30
2.8	Schematic illustration of the e ⁻ -beam heater	32
2.9	Schematic of the cylindrical mirror Auger analyser	33
2.10	Schematic of the four-grid optics operating in LEED mode	35
2.11	Schematic of a STM head similar to the RT-STM	36
2.12	Schematic of the STM I-V converter	38
2.13	Electrochemical etching set-up used to prepare the W STM tips.	39
3.1	Schematic diagram showing the principle of the local den- sity approximation	50
4.1	Diagram of the band structure of a metal-oxide-oxygen system.	68

5.1	A diagram of the Mo(110) surface. The centered rectangular unit cell is highlighted by the black box. The grey and black spheres represent the surface and second atomic layer atoms, respectively.	84
5.2	LEED image of the clean Mo(110) surface taken at 147eV. The Mo[001] direction is marked by the arrow.	86
5.3	AES spectra of a clean Mo(110) surface. The main Mo peaks are at 180 and 220eV	86
5.4	The crystal structure of MoO ₂ . Note the pairing of the metal atoms parallel to the monoclinic <i>a</i> axis.	88
5.5	A schematic of the energy level diagram of MoO ₂ restricted to the interactions between the atomic Mo 4d and the O 2p orbitals.	91
5.6	Diagram of the first Brillouin zone of the simple monoclinic lattice with high symmetry lines shown.	92
5.7	The calculated total and partial DOS of MoO ₂ . The black, red, and green lines represent the total, oxygen 2p and Mo 4d densities, respectively.	93
5.8	The calculated total and partial DOS of MoO ₂ from Eyert <i>et al</i> (7)	93
5.9	The calculated band structure of MoO ₂	94
5.10	The calculated band structure of MoO ₂ from Eyert <i>et al</i> (14)	94
5.11	The frequency dependent dielectric matrix of MoO ₂ calculated using VASP.	96
5.12	The frequency dependent dielectric matrix of MoO ₂ measured by optical reflectivity (10)	96

5.13	Frequency dependent reflectivity constant calculated by DFT.	96
5.14	Frequency dependent reflectivity constant on MoO ₂ by optical measurments.	96
6.1	The LEED pattern of the oxide overlayer on Mo(110) taken at 103eV	100
6.2	Real and reciprocal space diagrams of this system	102
6.3	STM image of the MoO ₂ /Mo(110) surface	104
6.4	The MoO ₂ (010) surface	106
6.5	Top view of the MoO ₂ (010) overlayer unit cell as determined by STM, LEED and DFT calculations	108
6.6	Model unit cell used for DFT calculations	109
6.7	DFT geometry optimizations of MoO ₂ (010)	110
6.8	Electron density difference for the 3-fold and on-top configuration	112
6.9	The high resolution STM image compared with a DFT STM simulation	114
6.10	Overlay of an STM simulation at 0.05V for the 3-fold case	115
7.1	LEED, STM, and line profiles of the Mo(110) surface after annealing in an oxygen	122
7.2	STM image of the profile of a large oxide wire	123
7.3	Auger spectra of the MoO ₂ oxide surface.	123
7.4	LEED pattern taken at 78eV	125
7.5	Ewald sphere diagram for the MoO ₂ “hill and valley” surface.	126
7.6	Graph od the LEED spot profile at changing energy	127

7.7	Diagram showing the epitaxy of the MoO ₂ (010) layer on Mo(110).	129
7.8	Diagram of the MoO ₂ building block.	130
7.9	Diagram of the various MoO ₂ wire sizes measured with STM.	131
7.10	An atomic model of the side and top views, respectively, of the oxide facet structure with the planes identified. . .	131
7.11	A diagram of the oxide facet structure with the planes identified.	132
7.12	Illustration of a faceted surface.	134
8.1	Graph of the nanowire height and thickness of an equivalent flat MoO ₂ film over time.	141
8.2	Illustration of Mo ions traveling up through the diffusion paths between the wires	142
8.3	Illustration of the oxidation reaction occurring with the oxygen reaching the metal surface through the diffusion paths	142
8.4	STM image showing wires growing on top of existing wires	143
8.5	AES spectra of a sample cooled abruptly and after annealing in oxygen	145
8.6	STM after stopping the annealing process more abruptly, i.e. in oxygen after 30 min.	146
8.7	STM after annealing the sample in oxygen at 250 °C at 1 x 10 ⁻⁶ Torr for one hour.	146
8.8	Possible growth mechanism once the diffusion paths are filled.	147

9.1	LEED images of Mo(100) films on Al ₂ O ₃	151
9.2	Auger spectra of as received, annealed and flashed Mo(110) films on Al ₂ O ₃	153
9.3	STM image of the Mo(110) film surface grown on Al ₂ O ₃ after annealing	154
9.4	STM and LEED images after annealing at 1000 °C, with flashes to 1300 °C	155
9.5	STM image of the Mo(110) film surface grown on Al ₂ O ₃ after flashing	156
9.6	LEED and STM image of the Mo(110) film surface grown on Al ₂ O ₃ after annealing and flashing	157
9.7	The STM and LEED image of Mo(110) film oxidized at 1 x 10 ⁻⁶ Torr oxygen at 900 °C for 30 min.	158
9.8	STM images of oxidized Mo(110) film. (a) is in UHV. (b) is in N ₂ . (c) is in air.	158
1	Circuit diagram of the inline box to switch the STM current gain by 10 and divide the tunneling bias by 1/10. . .	165

List of abbreviations

- 1D - one dimensional
- 2D - two dimensional
- 3D - three dimensional
- AES - Auger electron spectroscopy
- AFM - atomic force microscope
- BNC - bayonet Neill-Concelman
- CMA - cylindrical mirror analyser
- DFT - density functional theory
- DOS - density of states
- e^- -beam - electron beam
- ECM - electron counting model
- E_F - Fermi energy
- EM - electrostatic model
- FWHM - full width at half maximum
- GGA - generalized gradient approximation
- HOPG - highly oriented pyrolytic graphite
- KS - Kohn-Sham
- LDA - local-density approximation
- LDOS - local density of states
- LEED - low energy electron diffraction
- MBE - molecular beam epitaxy
- NEG - non evaporable getter
- PAW - projector augmented wave
- PDOS - partial density of states
- PLD - pulsed laser deposition

PTFE - poly-tetrafluoro ethylene (teflon)
PZT - lead zirconium titanate
RHEED - reflection high energy electron diffraction
RFA - retarding field analyser
RT - room temperature
RT-STM - room temperature scanning tunneling microscope
S/N - signal to noise ratio
STM - scanning tunneling microscopy
TM - transition metal
TSP - titanium sublimation pump
UHV - ultra high vacuum
UPS - ultraviolet photoemission spectroscopy
VASP - Vienna ab-initio simulation package
XPS - X-ray photoelectron spectroscopy
XRD - X-ray diffraction

Chapter 1

Introduction

The focus of this dissertation is the application of existing experimental and electronic structure methods for the study of the oxidation of the molybdenum (110) surface. Broadly, this dissertation is divided into two parts. The first part describes the methods and theories relevant to our experimental data, namely experimental techniques and ultra-high vacuum systems followed by density functional theory and oxidation theory. The second part briefly gives a background on the properties of molybdenum followed by a discussion of the results from experimental data obtained.

1.1 Motivation

The oxide formation on transition metal (TM) surfaces has received considerable attention in recent years (1; 2; 3; 4). Understanding the mechanisms of the initial growth stages of these oxides is necessary for both the fundamental understanding of the science and advancing related technologies. These oxides are important in many areas of industry, including surface coatings, materials science, and for industrial catalysts used in ox-

idation reactions for fuel processing, chemical production, and pollution clean-up. Recently, considerable steps have been made in the microscopic understanding of oxide formation on TM surfaces. With new advances in computer technology, researchers have gained a vast insight into the formation of these oxides by combining experimental data with density functional theory (DFT) calculations (1; 2; 3; 4; 5; 6; 7; 8; 9; 10). These calculations have lead to some rather complex models for the initial oxide formation that may or may not represent the bulk oxide.

For late transition metals and noble metals such as Pd and Ag, it is now known that the oxidation process proceeds through ultrathin oxide layers that are thermodynamically stable (11; 12; 13; 14). It is unclear whether the same holds true for TMs that are positioned further left on the periodic table. In response to this, we focused on the lighter metals of the 4d series to establish if a bulk-like surface oxide exists on the molybdenum surface; and if so, then what is the epitaxial relationship between the film and substrate. In doing so, we discovered a method that produces regular arrays of conducting MoO_2 nanowires on the Mo(110) surface.

Currently, there is an extraordinary amount of effort placed on developing new methods and techniques to build nanoscale structures and devices (15; 16; 17; 18; 19). The formation of quantum dots and wires of epitaxially grown thin solid films has been attracting attention as a very promising area of nanotechnology that could lead to a new generation of electronic devices. As MoO_2 is a metallic oxide, this means that these conductive wires are not only applicable for fundamental research but also for industrial technologies.

1.2 Organization

As briefly mentioned, this thesis is divided into two parts. Part I presents the theories and instrumental techniques used in this work. The first chapter (Chapter 2), gives a brief description of the theory of as well as a description of the instrumentation used. The following two chapters give a detailed description of density functional theory (DFT) and the theory of the oxidation of metals.

In part II we begin with a background of the materials used in this thesis as well as verifying the validity of the DFT methods used. This verification is done by comparing our calculated values for the structural and electronic properties of MoO_2 with that of experimental measurements in the literature.

In Chapter 6, we present the experimental results and describe a model for the MoO_2 surface oxide structure formed on $\text{Mo}(110)$. It was found that a bulk-like oxide of MoO_2 (010) grows epitaxially on the surface at $1000\text{ }^\circ\text{C}$ and 1×10^{-6} Torr oxygen pressure. LEED and STM data are used to give a detailed analysis of the oxide surface structure. From this experimental data, a model was built and through the use of DFT calculations, we show that a strained bulk-like $\text{MoO}_2(010)$ film is in excellent agreement with the experimental data.

The next step was to investigate the oxidation of $\text{Mo}(110)$ beyond the surface oxide phase. In Chapter 7, we present an inexpensive and robust technique of forming uniform nanowire arrays comprised of molybdenum oxide. In order to explain the nanowire growth, we employed a concept recently proposed by A. A. Golovin et. al. for the mechanism for the formation of quantum dots on the surface of thin solid films (20). We demonstrate experimentally that MoO_2 grown on $\text{Mo}(110)$ meets the

criteria for this mechanism, and show its application for the formation of regular arrays of structures at nanoscale dimensions. Furthermore, using an elastic theory of periodically faceted surfaces together with DFT calculations, we explain the critical size of these wires.

In Chapter 8 we describe the oxidation process of MoO_2 on the $\text{Mo}(110)$ surface under experimental conditions. This is done using the established theories of the oxidation of metals in addition to the experimental results in Chapters 7 and 6.

To conclude we present in Chapter 9, preliminary results of using this method to produce nanowires arrays of MoO_2 on an insulating substrate. This is a necessary step to enable one to study the metallic properties of these nanowires.

Bibliography

- [1] J. Gustafson et al., Phys. Rev. Lett. **92**, 126102 (2004).
- [2] J. Gustafson et al., Phys. Rev. B **71**, 115442 (2005).
- [3] C. T. Campbell, Phys. Rev. Lett. **96**, 066106 (2006).
- [4] M. Todorova et al., Phys. Rev. Lett. **89**, 096103 (2002).
- [5] A. Stierle et al., Science **303**, 1652 (2004).
- [6] D. J. Siegel, L. G. Hector, and J. B. Adams, Phys. Rev. B **65**, 085415 (2002).
- [7] R. Benedek, M. Minkoff, and L. H. Yang, Phys. Rev. B **54**, 7697 (1996).
- [8] M. W. Finnis, J. Phys.: Condens. Matter **8**, 5811 (1996).
- [9] J. Purton, S. C. Parker, and D. W. Bullett, J. Phys.: Condens. Matter **9**, 5709 (1997).
- [10] R. Benedek et al., Phys. Rev. Lett. **84**, 3362 (2000).
- [11] C. I. Carlisle, D. A. King, M.-L. Bocquet, J. Cerdá, and P. Sautet, Phys. Rev. Lett. **84**, 3899 (2000).
- [12] E. Lundgren et al., Phys. Rev. Lett. **88**, 246103 (2002).
- [13] W.-X. Li, C. Stampfl, and M. Scheffler, Phys. Rev. Lett. **90**, 256102 (2003).
- [14] K. Reuter and M. Scheffler, Appl. Phys. A **78**, 793 (2004).
- [15] H. Ibach, Surf. Sci. Rep. **29**, 195 (1997).
- [16] A. Mugarza et al., Phys. Rev. B **66**, 245419 (2002).
- [17] V. A. Shchukin and D. Bimberg, Rev. Mod. Phys. **71**, 1125 (1999).
- [18] R. Notzel et al., Nature **392**, 56 (1998).
- [19] D. Qin et al., Adv. Mater. **11**, 1433 (1999).
- [20] A. A. Golovin, M. S. Levine, T. V. Savina, and S. H. Davis, Phys. Rev. B **70**, 235342 (2004).

Bibliography

- [1] J. Guckenheimer and P. Holmes, *Bifurcation and Normal Form Theory*, Springer-Verlag, New York, 1983.
- [2] J. Guckenheimer and P. Holmes, *Bifurcation and Normal Form Theory*, Springer-Verlag, New York, 1983.
- [3] C. T. Campbell, *Phase Space Analysis of Nonlinear Systems*, Springer-Verlag, New York, 1983.
- [4] J. Guckenheimer and P. Holmes, *Bifurcation and Normal Form Theory*, Springer-Verlag, New York, 1983.
- [5] J. Guckenheimer and P. Holmes, *Bifurcation and Normal Form Theory*, Springer-Verlag, New York, 1983.
- [6] J. Guckenheimer and P. Holmes, *Bifurcation and Normal Form Theory*, Springer-Verlag, New York, 1983.
- [7] J. Guckenheimer and P. Holmes, *Bifurcation and Normal Form Theory*, Springer-Verlag, New York, 1983.
- [8] J. Guckenheimer and P. Holmes, *Bifurcation and Normal Form Theory*, Springer-Verlag, New York, 1983.
- [9] J. Guckenheimer and P. Holmes, *Bifurcation and Normal Form Theory*, Springer-Verlag, New York, 1983.
- [10] J. Guckenheimer and P. Holmes, *Bifurcation and Normal Form Theory*, Springer-Verlag, New York, 1983.
- [11] J. Guckenheimer and P. Holmes, *Bifurcation and Normal Form Theory*, Springer-Verlag, New York, 1983.
- [12] J. Guckenheimer and P. Holmes, *Bifurcation and Normal Form Theory*, Springer-Verlag, New York, 1983.
- [13] J. Guckenheimer and P. Holmes, *Bifurcation and Normal Form Theory*, Springer-Verlag, New York, 1983.
- [14] J. Guckenheimer and P. Holmes, *Bifurcation and Normal Form Theory*, Springer-Verlag, New York, 1983.
- [15] J. Guckenheimer and P. Holmes, *Bifurcation and Normal Form Theory*, Springer-Verlag, New York, 1983.
- [16] J. Guckenheimer and P. Holmes, *Bifurcation and Normal Form Theory*, Springer-Verlag, New York, 1983.
- [17] J. Guckenheimer and P. Holmes, *Bifurcation and Normal Form Theory*, Springer-Verlag, New York, 1983.
- [18] J. Guckenheimer and P. Holmes, *Bifurcation and Normal Form Theory*, Springer-Verlag, New York, 1983.
- [19] J. Guckenheimer and P. Holmes, *Bifurcation and Normal Form Theory*, Springer-Verlag, New York, 1983.
- [20] J. Guckenheimer and P. Holmes, *Bifurcation and Normal Form Theory*, Springer-Verlag, New York, 1983.

Part I

Instrumentation and Theory

Chapter 2

Description of the Experimental Techniques and the Ultra High Vacuum System

2.1 Auger Electron Spectroscopy

Auger electron spectroscopy (AES) is a powerful surface-sensitive technique used to determine the chemical composition of the surface layers of conducting or semiconducting samples (1; 2). With this technique, the sample is exposed to a monochromatic electron beam of energy between 2 and 30 KeV to promote the excitation of the so-called “Auger electrons”. By exposing the sample to incident electrons with sufficient energy to eject a core level K electron of the sample with energy E_K , the hole is filled by an electron from the level L_1 , with energy E_{L_1} . This transition generates an energy equal to $E_K - E_{L_1}$, which can either be

emitted as a X-ray photon (X-ray fluorescence) or transferred to a third electron, the “Auger electron”, at a level $E_{L_{2,3}}$, as shown in the example in Fig. 2.1. This electron is emitted with a kinetic energy $E_{KL_1L_{2,3}}$, equal to the energy difference between the three levels involved minus the sample work function ϕ , as indicated in equation 2.1. This is described graphically in Fig. 2.1.

$$E_{KL_1L_{2,3}} = E_K - E_{L_1} - E_{L_{2,3}} - \phi \quad (2.1)$$

Auger spectroscopy is based upon the measurement of the kinetic energies of the emitted electrons. The energies of these electrons are characteristic of each element and allow qualitative and quantitative identification of the elements present in the first 2-10 atomic layers (in the range of the inelastic mean free path of the Auger electrons).

2.2 Low Energy Electron Diffraction

Low energy electron diffraction (LEED) is one of the principal techniques for the determination of the surface structure of solids (3). A conducting sample with a well-ordered crystalline surface structure is exposed to a monochromatic beam of low energy electrons (20 to 300eV) normal to the surface. The impinging electrons are back-scattered by the Bragg planes of the crystal onto a fluorescent screen, which displays the diffraction pattern of the surface. Since the electrons are charged particles, they will be scattered by regions of high localised electron density, i.e. the surface atoms, by electrostatic Coulomb forces. Therefore, the surface atoms can be considered to act as point scatterers. By the principles of wave-particle duality, the beam of electrons may be equally regarded as

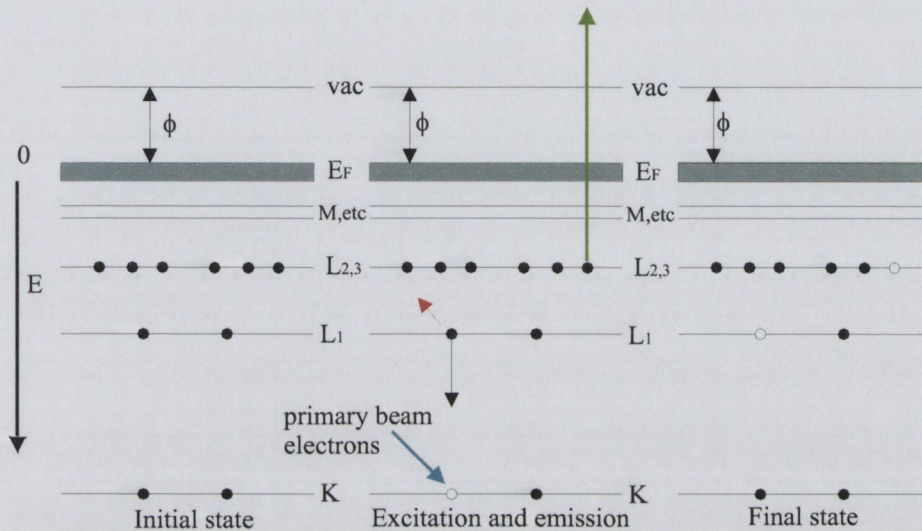


Fig. 2.1: Schematic of the Auger emission process. The ground state is shown on the left. Centre: an incident electron is ejected by the primary energy beam (blue arrow) creating a hole in the core level, K. Relaxation occurs resulting in an electron from the L_1 levels filling the core level hole and releasing an energy, $E_K - E_{L_1}$. This energy may be emitted as a photon (red arrow), or may be transferred to a secondary electron, which is then emitted from the crystal (green arrow). The state following emission, (Final state), is shown on the right.

a succession of electron waves incident normally to the sample.

The wavelength of the electrons is given by the de Broglie relation :

$$\lambda = \sqrt{150/E_0} \quad (2.2)$$

where λ is in \AA and E_0 is in eV.

In the simplest kinematical example, a diffraction pattern is formed analogous to that of a diffraction grating. In this example, only simple scattering from the surface is considered. This allows us to describe the shape and size of the surface unit cell, but it gives us no information about the atomic arrangement inside the unit cell. Furthermore, with

LEED we assume that only the elastically-scattered electrons contribute to the diffraction pattern; the lower energy (secondary) electrons are removed by energy-filtering grids placed in front of the fluorescent screen. Considering the atoms as point particles, the incident plane wave will be scattered in all directions. For an ordered crystal surface, interference will restrict the net flux to those directions where the scattered waves are in phase. This condition is met only when the scattered waves from neighbouring unit cells differ by an integral number of wavelengths λ . For the simple case of a 1D lattice, this in-phase condition for constructive interference is illustrated in Fig. 2.2, where the sample is normal to the incoming beam. Therefore, the positions at which diffraction spots occur is defined by the Bragg equation.

$$n\lambda = d \sin \theta \quad (2.3)$$

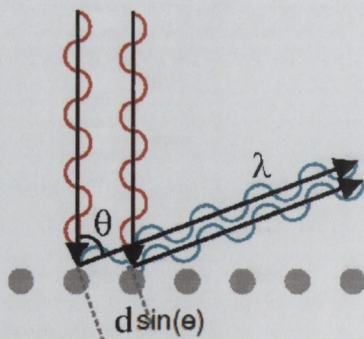


Fig. 2.2: Schematic of the Bragg condition for a 1D lattice. Only in the case of coherent interference between the scattered rays is it possible to detect a diffracted beam.

The LEED pattern consists of spots, in agreement with the Bragg law, that appear on the screen giving an image of the reciprocal lattice of the surface. The real space lattice parameter \vec{a} is related to the reciprocal

space lattice parameter \vec{a}^* by $\vec{a}^* = 2\pi/\vec{a}$.

For surface diffraction to occur in a 2D system, with translational vectors \vec{h} and \vec{l} , the incoming electron beam must conserve both its energy and the component of its momentum parallel to the surface:

$$\vec{k}_{\parallel}^2 + \vec{k}_{\perp}^2 = \vec{k}'_{\parallel}{}^2 + \vec{k}'_{\perp}{}^2, \quad \vec{k}'_{\parallel} = \vec{k}_{\parallel} + \vec{g}_{hl} \quad (2.4)$$

where \vec{k}_{\parallel} and \vec{k}_{\perp} are the parallel and perpendicular momentum components of the incident beam, respectively; while \vec{k}'_{\parallel} and \vec{k}'_{\perp} are those of the diffracted beam. The reciprocal lattice vector, now labelled \vec{g}_{hl} , is related to the beam energy E_{eV} , the electron mass m_e , and the diffraction angle θ by:

$$|\vec{g}_{hl}| = |h\vec{a}^* + l\vec{b}^*| = |\vec{k}| \sin\theta = \frac{\sqrt{2m_e E_{eV}}}{\hbar} \sin\theta \quad (2.5)$$

where \vec{a}^* and \vec{b}^* are the reciprocal lattice primitive net vectors. These are related to the real space vector \vec{a} and \vec{b} by (3):

$$\vec{a} \cdot \vec{a}^* = \vec{b} \cdot \vec{b}^* = 2\pi \quad \vec{a} \cdot \vec{b}^* = \vec{b} \cdot \vec{a}^* = 0 \quad (2.6)$$

This shows the direct correspondence between the observed diffraction pattern and the reciprocal lattice of the surface. The reciprocal lattice vector \vec{g}_{hl} lies in a direction that is orthogonal to the plane of the real space lattice which is denoted by the Miller indices h and l . The Miller indices of the diffracting planes are used to index the diffraction spots of the LEED pattern.

The diffraction pattern can easily be described graphically in reciprocal space by the Ewald sphere construction (fig. 2.2). A sphere with radius $1/\lambda$ is drawn through the origin of the reciprocal lattice. For each

reciprocal lattice rod that is located on the Ewald sphere of reflection, the Bragg condition is satisfied and diffraction arises.

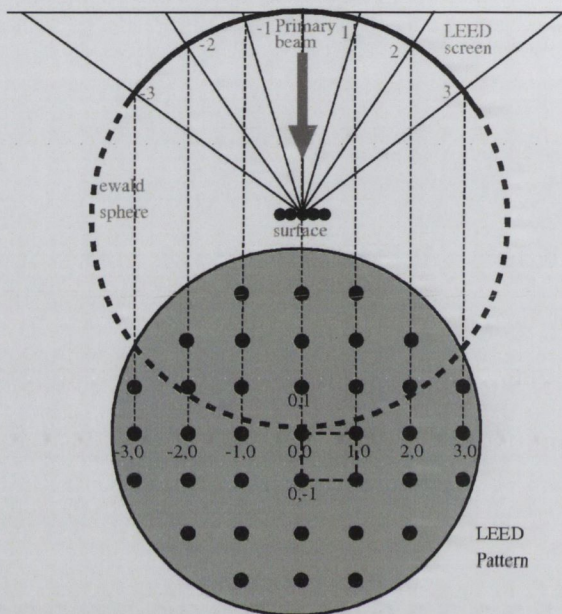


Fig. 2.3: Schematic of the Ewald sphere construction of a diffraction pattern.

In general for LEED experiments, the sample is normal to the incoming beam. This means that $k_{\parallel} = 0$ for the incident electrons. Therefore, the observed diffraction pattern will be an image of the reciprocal lattice of the surface. LEED patterns of surfaces are taken at the energy range between 20 and 200 eV. In this energy range, the de Broglie wavelength of electrons have the same order of magnitude as the interatomic distances of the crystals. The electron mean free path is of the order of $\sim 5-10 \text{ \AA}$, resulting in a technique that is sensitive only to the surface layers.

The observation of a LEED pattern does not guarantee that the whole surface is ordered. There is an instrumental limit to the diameter of the coherently scattering area on the surface called the coherence length. The significance is that interference will be strong within a coherent length of

the source, but not beyond it. The coherence of an e-beam is limited by δE and the beam divergence. The coherent length of a standard LEED optics is only 10 to 20 nm. Structures with a lower periodicity than that can therefore be imaged in the diffraction pattern. Naturally only structures which extend over at least (10 x 10) nm can produce Bragg reflexes. Furthermore, the diameter of the electron beam is about 1 mm², thus LEED averages over a large surface area.

Further information regarding crystal lattice structure may be obtained by both the position and the intensity of the spots. The position of the spots yields information on the size, symmetry and rotational alignment of the surface layers with respect to the symmetry of the bulk crystal. The intensities of the various diffracted beams which can be recorded as a function of the incident electron beam energy, generate the so-called I-V curves. By comparison with theoretical curves, the I-V curves may provide accurate information on atomic positions. While this is an extremely powerful technique, unfortunately, we do not have the experimental set-up to perform such measurements. Therefore, all of the LEED descriptions in this thesis are restricted to the simple kinematical approach.

2.3 Scanning Tunneling Microscopy

The scanning tunneling microscope (STM) invented by Binnig and Rohrer in 1981 (4), is without doubt, the most important instrument developed in surface science in recent years. The possibility to image the atomic structure of conducting and semiconducting materials has revolutionised the field, enabling the study of the properties of material surfaces

in direct space. In reality, the technique probes the electronic structure of the atoms at the surface and topographic information is derived from that. STMs are based on the principle of quantum mechanical tunneling.

2.3.1 Theory of Tunneling Effect

The principle behind the operation of a STM is the quantum tunneling effect. To understand this effect, consider an electron with energy E moving in a potential $U(z)$. In classical mechanics, it is described by the equation (5; 6):

$$\frac{p_z^2}{2m} + U(z) = E \quad (2.7)$$

where m is the mass of the electron and p its momentum. In quantum mechanics, the state of the same electron is described by the equation:

$$-\frac{\hbar^2}{2m} \frac{d^2}{dz^2} \psi(z) + U(z)\psi(z) = E\psi(z) \quad (2.8)$$

In the classical case, it is possible to distinguish 2 situations: (i) The allowed region, where $E > U(z)$ and the electron has a nonzero momentum p_z and (ii) the forbidden region, with $E < U(z)$ which the electron cannot penetrate. In the quantum mechanics case in the region where $E > U(z)$, equation 2.8 has solutions:

$$\psi(z) = \psi(0)e^{\pm ikz} \quad (2.9)$$

where k is the wave vector and is equal to $k = \sqrt{2m(E - U)}/\hbar$. In the region where $E < U(z)$, i.e. the tunneling region, the equation 2.8 has the solution:

$$\psi(z) = \psi(0)e^{-\kappa z} \quad (2.10)$$

where κ is a decay constant and is equal to: $\kappa = \sqrt{2m(U - E)}/\hbar$.

The probability density of finding an electron near a point $+z$ is proportional to $|\psi(0)|^2 e^{-2\kappa z}$, which has a nonzero value in the barrier region and thus a nonzero probability to penetrate the barrier. An analogous solution describes an electron state in the $-z$ direction $\psi(z) = \psi(0)e^{\kappa z}$.

This simple model explains some basic features of the one-dimensional metal-vacuum-metal tunneling effect (a more detailed treatment can be found in (7)), shown in figure 2.4. Now consider a metal surface and a

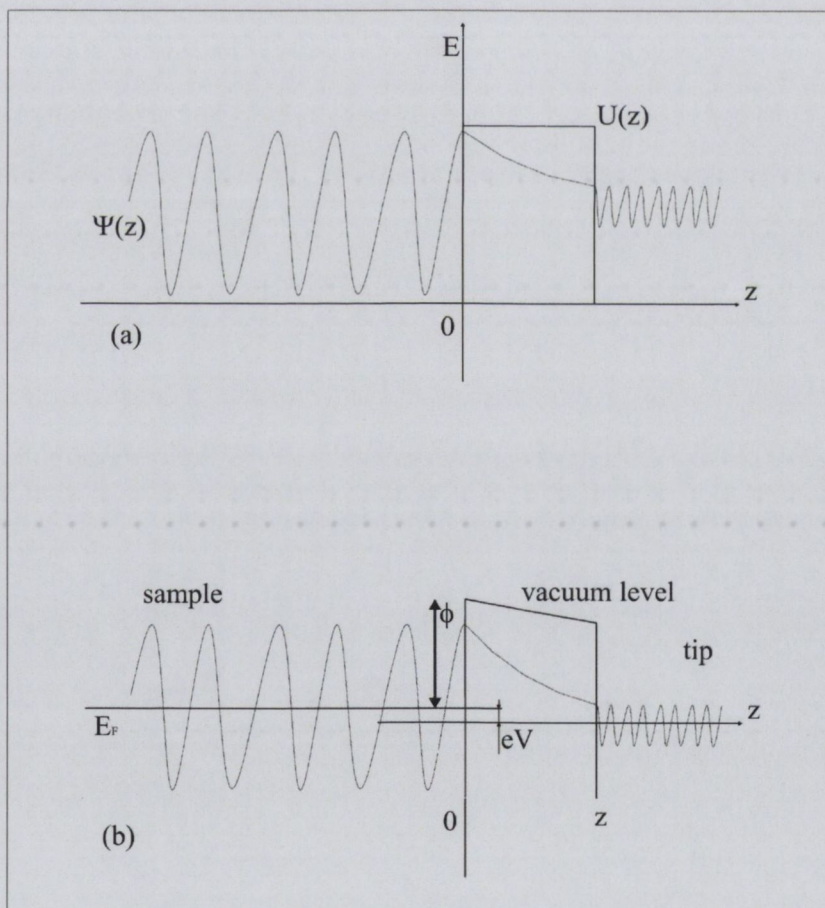


Fig. 2.4: a) General tunneling barrier for an electron described by the wavefunction $\psi(z)$ in a one-dimensional potential $U(z)$. b) Schematic of a STM tunneling junction under the applied bias voltage V .

sharp metal tip placed within a few angstroms of it. The work function

ϕ of the metal surface is the minimum energy required to remove an electron from the sample/tip to the vacuum level and the Fermi level E_F is the upper limit of the occupied states in the metal if thermal excitation is neglected. If the vacuum level is considered as the reference point of energy, then $E_F = -\phi$. Considering the simple case in which the work functions of sample and tip are equal, an electron can tunnel between them. Nevertheless, a bias voltage V_b is necessary to have a net tunneling current I_t . Applying V_b to the tip, a sample state ψ_n with energy E_n lying between $E_F - eV_b$ and E_F , has a probability to tunnel into the tip. Assuming that $eV_b \ll \phi$ the energy level of all the sample states of interest are very close to the Fermi level, $E_n \approx -\phi$. The probability w to find an electron at the tip surface $z = W$, is given by:

$$w \propto |\psi_n(0)|^2 e^{-2\kappa W} \quad (2.11)$$

where the decay constant κ is now given by $\kappa = \sqrt{2m\phi}/\hbar$. The states on the sample surface within the energy interval given by eV_b are responsible for the tunnel current I_t and determine I_t as follows:

$$I_t \propto \sum_{E_n=E_F-eV_b}^{E_F} |\psi_n(0)|^2 e^{-2\kappa W} \quad (2.12)$$

For small V_b , the sum in equation 2.12 can be written using the local density of states (LDOS) at the Fermi level. At a location z , the LDOS $\rho_S(z, E)$ of the sample is defined as $\rho_S(z, E) \equiv \frac{1}{\epsilon} \sum_{E_F-\epsilon}^{E_F} |\psi_n(z)|^2$ for a sufficiently small energy, ϵ . The value of the LDOS near the Fermi level is an indicator of whether the surface is metallic or not. The I_t can be

conveniently written in terms of the LDOS of the sample:

$$I_t \propto V_b \rho_S(0, E_F) e^{-2\kappa W} \quad (2.13)$$

The dependence of the logarithm of I_t with respect to distance W is a measure of the work function ϕ , or the tunneling barrier height. It is also clear that the I_t is very sensitive to small variations in the distance between tip and sample.

2.3.2 The Scanning Tunneling Microscope

An atomic sharp metal tip is brought to within 1 nm of the surface of a conducting or semiconducting sample. A voltage is applied across the two electrodes, tunneling is established and a tunneling current is detected. As demonstrated above, the tunneling current I_t can be expressed by Eq. 2.13. In reality, the tunneling current is also dependent on the LDOS of the tunneling tip. The significance of the tip contribution can be accounted for through a time-dependent perturbation model of a metal-insulator-metal tunneling, proposed by Bardeen (8). In this approach a transfer Hamiltonian H_T is used to describe the tunneling of an electron, from a sample state ψ , to a tip state χ . The tunnel current is a convolution of the sample LDOS ρ_S and the tip LDOS ρ_T .

$$I_t = \frac{4\pi e}{\hbar} \int_0^{eV} \rho_S(E_F - eV + E) \rho_T(E_F - E) |M|^2 dE \quad (2.14)$$

The tunneling current I_t also includes a tunneling matrix element M , which describes the amplitude of electron transfer across the tunneling barrier, as a function of the overlap between sample states (ψ) and tip

states (χ).

$$M = \frac{\hbar}{2m} \int (\chi^* \frac{\partial \psi}{\partial z} - \psi \frac{\partial \chi^*}{\partial z}) dS \quad (2.15)$$

It is determined by a surface integral on the medium separating the two electrodes. If M is constant over the voltage range probed, the tunnel current is determined by a convolution of the LDOS of the two electrodes, the tip and the sample.

Once tunneling is established, the tip is scanned mechanically across the surface. There are two basic modes for the scanning process, namely, constant current or constant height. The most commonly used mode is the constant current mode. In this case, the tunneling current is kept constant in the range from a few pA to 1-2 nA, by a feedback control unit that changes the tip-sample separation in response to a change in the tunneling current. However, in the constant height mode, the tip to sample distance is kept constant and the tunneling current recorded as a function of the tip position. In this thesis, the STM was operated in the constant current mode for all the measurements performed.

2.4 DC Magnetron Sputtering

DC magnetron sputtering is a physical vapour deposition (PVD) process in which gas ions from a plasma are accelerated towards a "target"; i.e. the material to be deposited. The target material is ejected or "sputtered" and deposited on a substrate in the vicinity. This process takes place in a high vacuum environment with a base pressure of 10^{-8} Torr. The sputtering process involves a gas, usually argon, being released into the chamber at a pressure of between 10^{-6} to 10^{-5} Torr. By natural cosmic radiation there are always some ionized Ar^+ ions available. In

the DC-sputtering process, a negative potential U , up to some hundred volts, is applied to the target. As a result, the Ar-ions are accelerated towards the target and on impact sputter away some material. The collisions of these ions also produce secondary electrons. These electrons cause a further ionisation of the gas. By placing a ring magnet below the target the electrons are trapped in its field forming cycloids over the target's surface. This gives the electrons a longer time to dwell in the gas causing a higher ionisation probability and hence produce a plasma ignition at pressures which can be up to one hundred times lower than for conventional sputtering. This set-up is called a magnetron (Fig. 2.5). With a magnetron, higher deposition rates can be realized. However, the longer mean free path of the sputtered material means a larger kinetic energy on impact with the substrate. Furthermore, the substrate can be heated to increase the mobility of the arriving material and in some cases produce higher quality films.

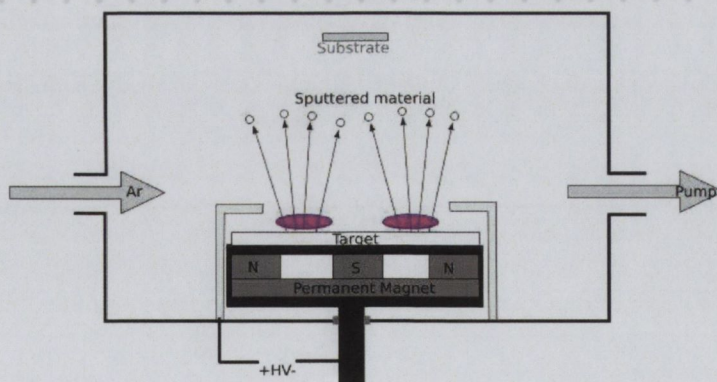


Fig. 2.5: Diagram of a Magnetron sputtering set-up

	-Low-	-Med.-	-HV-	-UHV-	-XHV
P(mbar)	10^3	1	10^{-3}	10^{-6}	10^{-12}
P(Pa)	10^5	10^2	10^{-1}	10^{-4}	10^{-10}

Table 2.1: The various ranges of vacuum, defined in units of *mbar* and *Pa*, where 1 atmosphere = 760 Torr = 1013 millibar = 1.013×10^5 pascal. HV, UHV and XHV refer to high-, ultra-high and extreme-high vacuum, respectively. Reproduced from (9).

2.5 Ultra-high vacuum

2.5.1 Vacuum requirements

The presence of adsorbates on a surface can have a variety of effects such as altering surface stress, causing surface reconstruction, quenching magnetic moments, etc. Therefore, the presence of contaminants can significantly affect results obtained with surface-sensitive techniques such as STM, LEED, AES, ESD, etc. Consequently, a high degree of surface cleanliness (≤ 1 at%) is required during the observation time of an experiment in order to obtain a meaningful result.

The period during which the surface contamination will be within an acceptable limit is determined primarily by the rate at which gas particles (atoms or molecules) impinge upon the sample surface, given by equation 2.16:

$$R = \frac{P}{\sqrt{2\pi mk_B T}} \quad [m^{-2}s^{-1}] \quad (2.16)$$

At constant temperature, this is largely dependent upon the gas pressure within the experimental environment. Reducing this gas pressure will increase the longevity of a clean surface. As a result, most surface sensitive techniques require a vacuum environment for operation. Table 2.1 lists the various ranges of vacuum.

When considering vacua, it is useful to calculate the molecular mean

free path, λ , which is the average distance travelled by a gas particle before it collides with another particle.

$$\lambda = \frac{1}{\sqrt{2}\pi d^2 n} \quad [\text{m}] \quad (2.17)$$

where πd^2 represents the collision cross-section of the particle, d is the particle diameter and n is the number density of particles, given by:

$$n = \frac{P}{k_B T} \quad [m^{-3}] \quad (2.18)$$

A monolayer formation time, τ_m , is defined as the time taken to form a complete particle layer on the surface. In addition to the impingement rate, τ_m will depend on the sticking probability, $s(\theta)$, of the gas particle on the surface. For sub-monolayer coverages, this can be expressed as:

$$s(\theta) = s_0(1 - \theta) \quad (2.19)$$

The sticking probability is dependent upon the fraction of the surface already covered, θ . Beginning with an initial sticking probability, s_0 , it falls off as the fraction of available adsorption sites $(1 - \theta)$ decreases. Assuming that the sticking probability is constant and that when the gas particle strikes the surface there is a one-to-one correspondence between the gas and surface atoms, the monolayer formation time τ_m is:

$$\tau_m = \frac{n_s}{RN s_0} \quad (2.20)$$

where n_s is the total number of surface atoms and N is the number of atoms per gas particle.

As an example the monolayer formation time is calculated for N_2

P (mbar)	P (Pa)	n (m^{-3})	λ (m)	R ($m^{-2}.s^{-1}$)	τ_m
1013	1.013×10^5	2.5×10^{25}	6.6×10^{-8}	2.9×10^{27}	1.7 ns
1.33×10^{-3}	0.133	3.2×10^{19}	5.1×10^{-2}	3.8×10^{21}	1.3 ms
1.33×10^{-6}	1.33×10^{-4}	3.2×10^{16}	5.1	3.8×10^{18}	1.3 s
1.33×10^{-9}	1.33×10^{-7}	3.2×10^{13}	5.1×10^4	3.8×10^{15}	22 min.
1.33×10^{-11}	1.33×10^{-9}	3.2×10^{11}	5.1×10^6	3.8×10^{13}	36.5 hrs.

Table 2.2: Gas particle density n , mean free path λ , arrival rate R and monolayer formation time τ_m on the W(100) surface at various pressures for N_2 at 300K.

adsorption on the W(100) surface at room temperature for various pressures in Table 2.2. The sticking coefficient is assumed to be equal to unity, while the molecular mass is taken as 4.65×10^{-26} kg and the molecular diameter is taken as 3.7 Å(10). The lattice parameter of bcc tungsten is 3.165 Å, so that the atomic density of the W(100) surface n_s is $9.98 \times 10^{18} m^{-2}$.

For surface studies of transition metals such as Fe, Mo and W, which are highly reactive, with a particularly strong affinity for oxygen, a high degree of surface cleanliness can only be achieved for long periods under ultra-high vacuum (UHV) conditions.

2.5.2 Pumping

The pumping time required to reach a specific vacuum pressure depends on the gas flow rate from the chamber being evacuated. The gas flow rate, or throughput Q is given by:

$$Q = \frac{d(PV)}{dt} \quad [Pa.m^3.s^{-1}] \quad (2.21)$$

which is related to the *mass flow rate* by:

$$\frac{dM}{dt} = \frac{mQ}{k_B T} \quad [kg.s^{-1}] \quad (2.22)$$

while Q is related to the *volume flow rate* S by:

$$Q = SP \quad (2.23)$$

There are three main gas flow regimes, all of which are encountered during a pump-down from atmospheric pressure to UHV. These are the (1) turbulent, (2) viscous or laminar and (3) molecular flow regimes. The factors which determine the particular regime are:

- The magnitude of the flow rate.
- The pressure difference across the vessel through which there is gas flow.
- The surface finish and geometry of this vessel.
- The nature of the gas being pumped (molecular weight, etc.).

The nature of the gas flow can be defined by two dimensionless numbers, the Reynolds number, R_e , and the Knudsen number, K_n , where:

$$R_e = \frac{\rho v D}{\eta}, \quad K_n = \frac{\lambda}{D} \quad (2.24)$$

where ρ is the gas density ($kg \cdot m^{-3}$), v is the flow velocity ($m \cdot s^{-1}$), η is the gas viscosity ($N \cdot s \cdot m^{-2}$) and D is the diameter of the vessel.

Turbulent flow: This regime is encountered very briefly during the initial stages of pump-down. At this point, there is a high pressure gradient between the pump inlet and the main body of the vessel. The mean free path for particle collisions is much smaller than the dimensions of the vessel. With a Reynolds number $R_e > 2100$, it is characterised by chaotic flow with many eddies and vortices.

Laminar or viscous flow: With a Reynolds number $R_e < 1100$ ¹ and a Knudsen number $K_n < 0.001$, this flow regime is encountered in the early stages of pump-down, at moderate pressure gradients. It is characterised by ordered flow which is proportional to the pressure gradient and the viscosity. The viscosity limits the flow since collisions between gas particles occur more frequently than collisions with the vessel walls. Only particles near the walls collide with them, so that the velocity decreases near these surfaces.

Molecular flow: As the mean free path of the gas particles approaches the dimensions of the vessel, the flow reaches an intermediate stage between viscous and molecular flow. However, when $K_n > 1$, more collisions occur with the vessel walls than with other gas particles. This is the molecular flow regime, where the motion of the gas particles is random but there is a net flow from regions of higher to lower particle concentration. Pumping in this regime is based on the concept of capturing the particles that stray into the pump inlet.

The various pipes through which the vessel is pumped offer resistance to all forms of gas-flow, resulting in a pressure gradient ΔP between its opposite ends. The conductance of a pipe or bellows is the reciprocal of this resistance and is defined as:

$$C = \frac{Q}{\Delta P} \quad [m^3 \cdot s^{-1}] \quad (2.25)$$

Capacitance C and pumping speed S are conventionally given in units of $L \cdot s^{-1}$ (or equivalently in $m^3 \cdot hour^{-1}$). For the conductance of pipes in

¹A Reynolds number in the range $1200 < R_e < 2200$ can correspond to either turbulent or laminar flow, depending on the surface roughness and geometry of the vessel.

parallel, the total conductance C_T is:

$$C_T = C_1 + C_2 + \dots + C_n \quad [L \cdot s^{-1}] \quad (2.26)$$

while for pipes in series:

$$\frac{1}{C_T} = \frac{1}{C_1} + \frac{1}{C_2} + \dots + \frac{1}{C_n} \quad (2.27)$$

For a pump with nominal pumping speed S ($L \cdot s^{-1}$) connected to a pipe of conductance C , the effective pumping speed is limited by the conductance of the pipe as:

$$\frac{1}{S_{eff}} = \frac{1}{S} + \frac{1}{C} \quad (2.28)$$

It is clear that the conductance of a pipe will depend upon its surface finish and geometry, while the smallest conductance between the pump and the chamber will determine the effective pumping speed within it.

The ultimate pressure in a system is obtained when equilibrium is reached between the throughput due to pumping and the throughputs due to processes which deliver gas particles into the system. These are:

- Leaks from the atmosphere side through misaligned flanges or cracked welds.
- Virtual leaks from trapped air pockets, such as those formed when a screw is threaded into a blind hole. Gas escapes slowly along the helical path of the thread.
- Surface and volume out-gassing of gas particles which have been adsorbed onto and absorbed into materials present inside the chamber - the major adsorbed contaminant is water. All materials chosen for vacuum applications have an extremely low vapour pressure so that they will not

sublime or evaporate in vacuum. The speed at which the out-gassing process is completed is usually increased by thermal activation through baking of the vacuum system.

- The materials used for construction of vacuum systems such as glass, stainless steel, viton rubber, etc. are partially permeable to the lighter elements. For example hydrogen can diffuse through stainless steel. This is a continuous process as gas particles can enter the vacuum system from the atmosphere side by diffusion.

A more detailed discussion of these topics, including flow calculations is available in references (11) and (12).

2.6 The UHV System

The Ultra High Vacuum (UHV) system used in this work consists of three main chambers: the preparation chamber, the Room Temperature STM (RT-STM) chamber and the LEED and Auger chamber. The layout of the system is shown in Fig. 2.6.

A detailed description of the different chambers has been given elsewhere (13; 14; 15) and as a result, only a brief introduction of the RT-STM chamber and the Preparation Chamber will be given in the following section. Every chamber can be isolated by closing a valve (valved off) and independently brought to atmospheric pressure without disrupting the vacuum in the other chambers. This is done via a series of UHV gate valves (16). A fast entry loadlock allows the transfer of tips and samples in and out of the preparation chamber without disrupting the vacuum (17). A differential $20 \ell \cdot s^{-1}$ ion pump (17) keeps the vacuum at a pressure of 10^{-8} Torr. Transferring samples and tips inside the UHV system

is done by means of wobblesticks and magnetically coupled linear drives (18) with access to each sample stage. The pressure in each chamber is monitored by nude Bayard-Alpert type ionisation gauges (17). The whole system is supported on a stainless steel frame which can be floated on pneumatic dampers to minimise vibration during STM measurements.

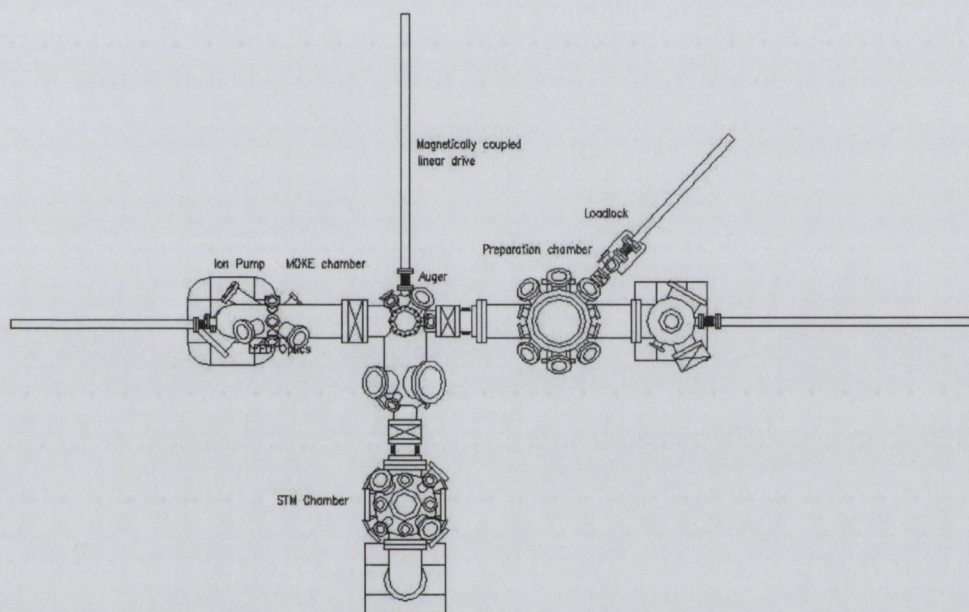


Fig. 2.6: Top view schematic of the ultra high vacuum (UHV) system.

2.7 The Preparation Chamber

Several different pumps can be employed to attain and maintain the system in UHV ($10^{-10} - 10^{-11}$ Torr). A $260 \text{ l} \cdot \text{s}^{-1}$ turbomolecular pump (19) backed by a $0.7 \text{ l} \cdot \text{s}^{-1}$ two-stage rotary vane pump, generates the vacuum in the chamber. Then, a double-ended $240 \text{ l} \cdot \text{s}^{-1}$ differential ion pump (17) maintains the system in UHV conditions. A liquid nitrogen cryoshroud, together with a titanium sublimation pump (TSP), is inserted in the base flange of the ion pump and a non-evaporable get-

ter (NEG) pump (20) is positioned mid-way along the chamber. Inside the chamber, different facilities are present that allow tip and sample preparation. A resistive heater, an Ar^+ gun, precision leak valves for the introduction of high purity gases, a triple evaporator with integral flux monitor (21) and a quartz crystal deposition monitor (22) are present for routine cleaning and treatment of samples and tips. The preparation chamber also contains a cylindrical mirror analyser (CMA) based Auger electron spectroscopy subsystem (17).

2.7.1 The resistive heater

The resistive heater was designed by C. Kempf and its schematic is shown in Fig. 2.7.

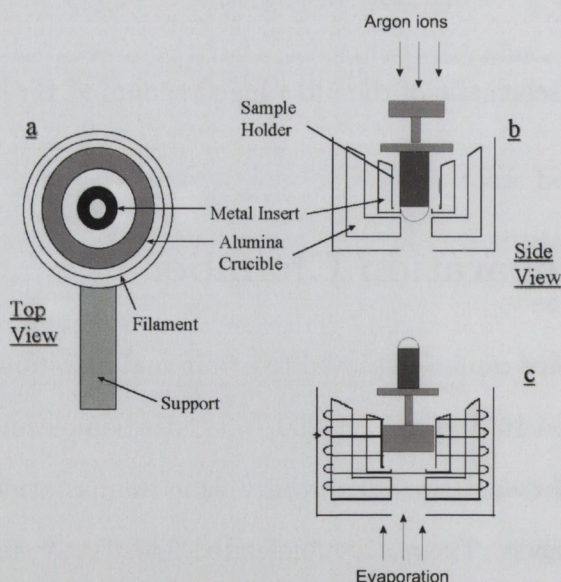


Fig. 2.7: Schematic illustration of the resistive heater. a) Top view. b) Side view. The sample, or tip, is inserted face-up for ion etching. c) Side view. The sample can sit face-down in the heater for evaporation experiments. Reproduced from (23)

It consists of an alumina crucible with a spiral groove machined along its circumference, along which a 0.2 mm thick tungsten wire is wrapped. It also acts as a sample stage for the Ar^+ etching and thin film deposition. The sample holder sits inside a tantalum insert fitted inside the crucible. The sample holder consists of a tantalum cap that screws onto a molybdenum body. The crucible is supported by a stainless steel can, which is attached to a feedthrough for the quartz crystal monitor. The feedthrough comprises two water cooling pipes and a BNC feedthrough to carry the signal from the in-situ quartz crystal to the ex-situ monitor. A separate feedthrough carries the connections to the heater filament and a K-type thermocouple spot-welded to the tantalum insert. The thermocouple enables the calibration of the resistive heater each time the filament is replaced, obtaining a temperature (K) versus power (W) calibration curve. The temperature range of the resistive heater is 350 K to 1000 K.

2.7.2 The e^- -beam heater

The electron beam heater was designed and build by Dr. J. Osing (14) and its schematic is shown in Fig. 2.8.

This heater is used for annealing at high temperatures up to 2500 K. The sample holder is inserted into a tantalum stage kept at +1 kV. A DC current is driven through a grounded thoriated tungsten filament (diameter 0.15 mm, 1 % thorium), which generates thermionic emission of electrons. The filament is positioned very close to one side of the sample cap so that electrons, accelerated by the positive bias, collide with the sample transferring their kinetic energy as heat. A temperature gradient is therefore present across the sample due to the position of the

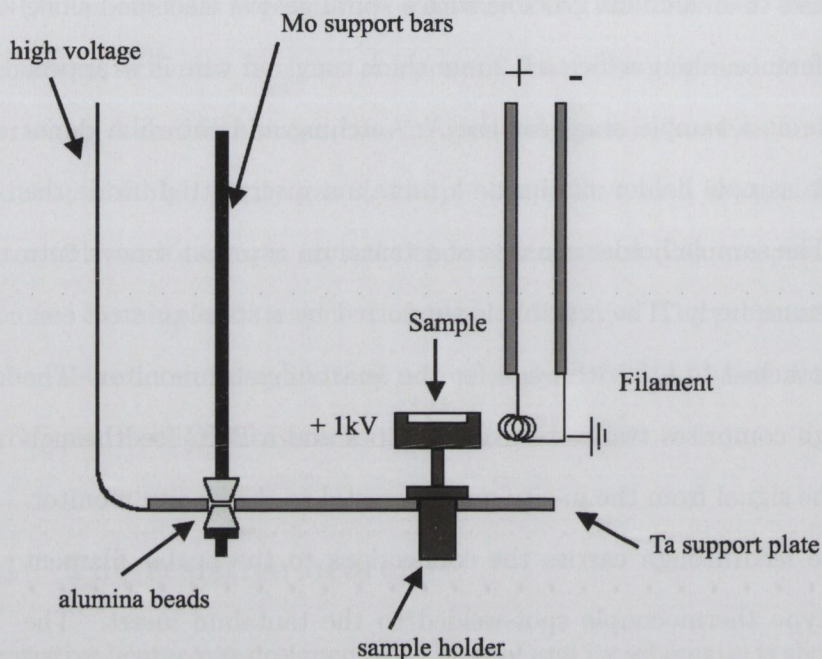


Fig. 2.8: Schematic illustration of the e^- -beam heater. Reproduced from (14)

filament. The temperature of the surface is measured with an infra-red pyrometer (Altimex UX-20/600 (24)) through a viewport.

2.7.3 The Ar^+ ion gun

For the in-situ cleaning of the samples' surface and STM tips, the system is equipped with an inert sputter ion source (25) for Ar^+ etching. This is fitted with two tungsten filaments through which a current of 2.6 A is driven during routine operation. The Ar gas is introduced, by means of a leak valve, directly into the gas cell of the ion gun and ionised by electron bombardment. Upon discharge, the Ar^+ ions are accelerated by a negative voltage of value between -0.2 and 2.0 kV, applied to the sample or tip to be sputtered. Discharge currents are typically 30-40 mA. The diameter of the target is taken as 11 mm, i.e. the diameter of

the circular tantalum insert in the resistive heater that accommodates the sample or tip. This is electrically isolated by the ceramic crucible. The target current I passing through the sample or tip is measured via the thermocouple spot-welded to the tantalum insert. This results in ion current values between $7.0 \leq I \leq \mu\text{A}$ when the beam energy is between 0.5 to 2.0 keV and Ar pressure is 5×10^{-6} Torr.

2.8 Auger Electron Spectroscopy Set-Up

The Auger analyser is a cylindrical mirror analyser (CMA, model 10-155A Physical Electronics (26)). A schematic of the Auger analyser is seen in Fig. 2.9.

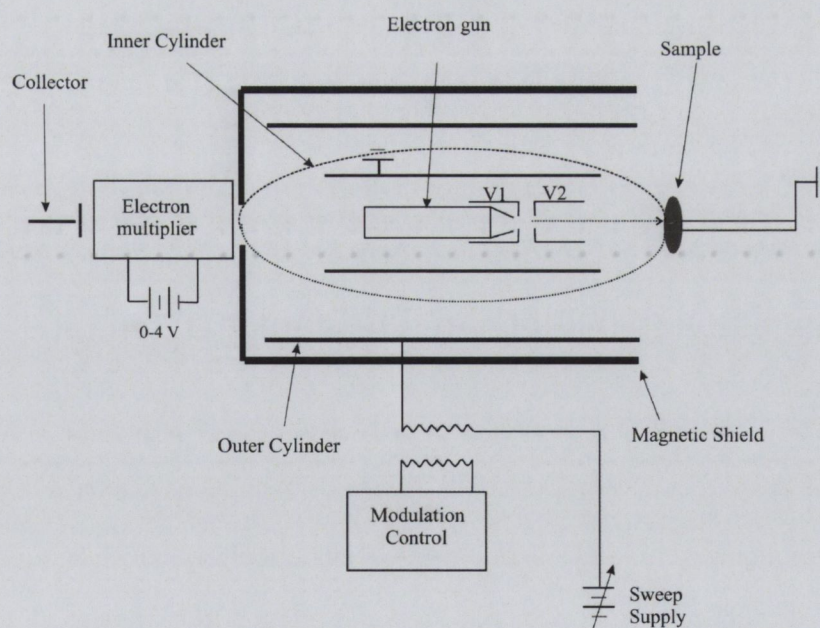


Fig. 2.9: Schematic of the cylindrical mirror Auger analyser

The primary electron beam is generated from a hot filament source,

and accelerated through a potential V_2 . The beam current can be varied by changing the extraction potential V_1 . The electron gun is within two concentric cylinders. The inner cylinder is grounded, while a deflecting potential is applied to the outer cylinder. The deflecting potential is chosen such that only electrons of a particular energy will pass through the exit aperture. The analyser current is given by the number of electrons that pass through this aperture. Between the exit aperture and the collector, an electron multiplier is used to amplify the analyser current. A full description of the operation of the Auger analyser can be found in (27). A beam of energy of 3 keV was used for all measurements. The filament and emission currents were 3.2 A and 0.4 mA respectively, giving a target current of $\sim 8 \mu\text{A}$. A SR 850 DSP lock-in amplifier from Stanford Research Systems (28) was used to output a $0.5 V_{rms}$ sinusoidal signal of frequency 12 kHz to modulate the deflecting voltage applied to the outer cylinder. A lock-in sensitivity of $100 \mu\text{V}$ was then used to detect the Auger signal. The scan was always set to 1 eV/s.

2.9 Low Energy Electron Diffraction

The SPECTALEED four-grid reverse view optics used in the experiments described here were manufactured by Omicron NanoTechnology GmbH. The optics were mounted on an O.D. 200 mm CF custom elbow which is tilted at an angle of 30° to the horizontal. The sample sits in the transfer fork of a magnetic drive, which is grounded by a stainless steel braid to an OFHC copper block at the bottom of the LEED annex. The sample is rotated in this drive so that its surface faces the electron gun. Scattered electrons are collected by the grids and screen located behind the gun.

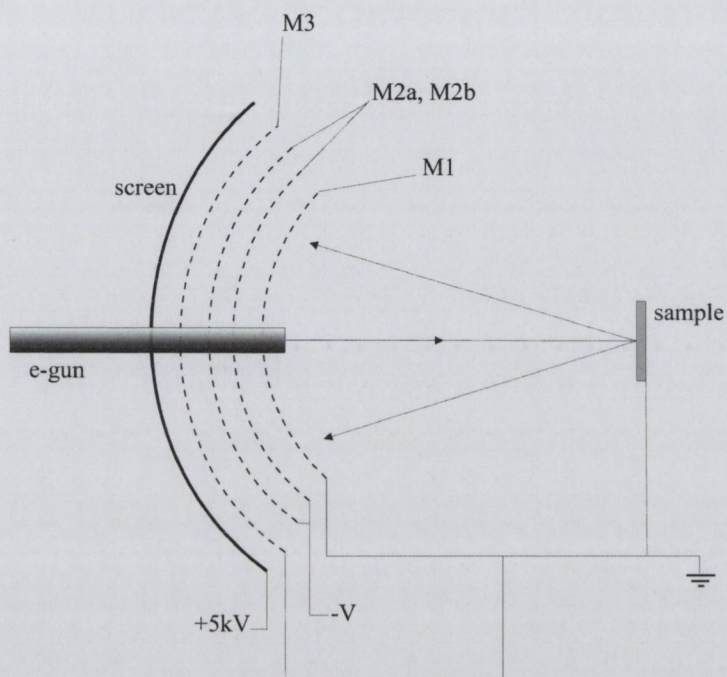


Fig. 2.10: Schematic of the four-grid optics operating in LEED mode (3).

A schematic illustration of a four-grid LEED apparatus is shown in Fig. 2.10. It consists of an electron gun, providing a collimated beam of electrons, and a hemi-spherical fluorescent screen of which the diffracted electrons are observed. The grid nearest the sample, M1, is earthed, so that electrons scattered by the sample initially travel in field-free space. A negative potential is applied to the two centre grids, M2a and M2b, to suppress inelastically scattered electrons, while elastically scattered electrons are accelerated towards the phosphorescent screen by its +5 keV potential. The fourth mesh M3 is also grounded to reduce the field penetration of the suppressing grids by the screen.

2.10 The Room Temperature STM

The room temperature STM head is constructed of titanium and comprises a piezo tube scanner and a fine approach piezowalker, see Fig. 2.11. It is based upon the system developed by Dr. S. H. Pan at the University of Basel, Switzerland (29).

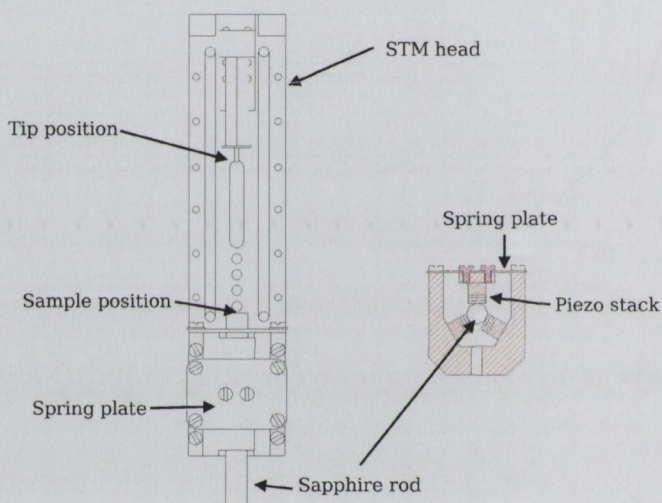


Fig. 2.11: Schematic of a STM head similar to the RT-STM. A front view and a cross-section of the fine approach walker are shown.

In this design, the sample is mounted on top of a cylindrical polished sapphire rod. The rod is clamped between a set of six piezo stacks, mounted in a triangular fashion. One pair of piezo stacks is spring-loaded against the sapphire rod. The motion of the sapphire rod occurs in two steps. First, the stacks rapidly shear simultaneously so that the rod remains fixed as the stacks slip along the rod. All six piezo stacks are then allowed to relax simultaneously, such that the rod is dragged in the direction opposite to the original shear direction.

The piezoelectric tube scanner has four electrodes of equal area, parallel to the axis of the tube. The inner electrode is grounded, so that

when a voltage is applied to one of the outer electrodes, the tube scanner bends away from that electrode. The scanner has a dynamic range of $\pm 13000 \text{ \AA}$ in the z-direction and 20600 \AA in the x- and y- directions. The STM head is isolated from vibrations by a two-stage spring system (13), which works in conjunction with the pneumatic dampers on the system frame.

The STM controller used for these experiments is a SCALA system by Omicron (21). This controller allows the user to compensate for the thermal drift using a topographic feature of the STM image as a reference point. The accompanying software provides functions for data analysis. Data were also analysed using commercial software from Nanotech electra S. L. (30).

2.10.1 Modifications to STM

During the course of this research, I have made several improvements to the STM. Central to the STM is the current voltage (I-V) converter. Since the tunnel current in STM is in the range of 10 pA to 50 nA , the first stage of signal processing is to convert the current into a measurable voltage. Fig. 2.12 shows the schematic for the in situ I-V converter.

One of the main factors that limits the performance of the STM I-V circuit is the stray input capacitance. A large feedback resistor is used to provide a large gain in order to provide a measurable voltage. In our case, we use a $10^8 \Omega$ resistor for a conversion factor of 10^8 . The greater the resistor, the greater the gain. However, there will always be some stray capacitance in parallel with the resistor. The two act as a low-pass RC filter, thus limiting the bandwidth of the circuit. An estimate of the circuit bandwidth is the frequency at which the signal has dropped

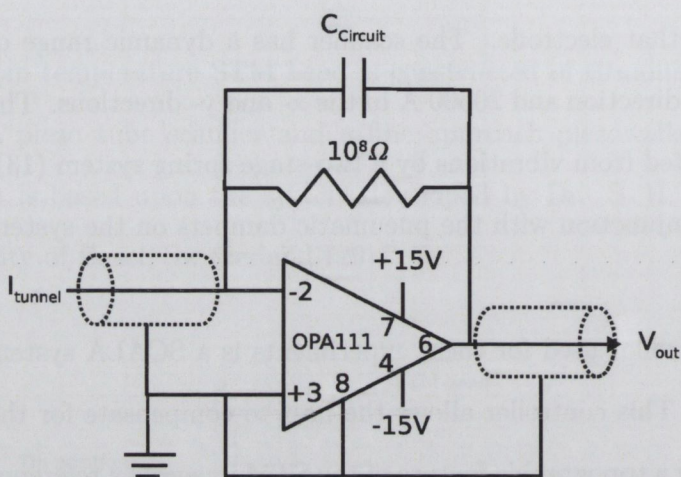


Fig. 2.12: Schematic of the STM I-V converter.

by -3 dB, and is calculated by $f_{-3dB} = (2\pi RC)^{-1}$. Upon inspection of the STM, I realized that the I-V converter was connected to the STM tip with a 100 pF coaxial cable, giving a -3d B point of only 16hz. To improve the situation, I relocated the I-V converter directly over the scanner and connected it with a 3 cm length of fine wire shielded with a 5mm diameter braided cable. In this case the input capacitance is less than 0.5 pF, giving a -3 dB point of at least 3.2 kHz. This change was immediately noticeable and resulted in scanning rates 10 X faster than previously possible.

In addition to this, the STM controller has the option to control a 1/10 voltage divider and an external amplifier to increase the signal gain by 10-fold. To make use of these features, I made a small box containing a digitally switchable voltage divider and 1-10 X amplifier to be placed inline with the bias voltage and tunneling signal lines. A schematic of the circuits inside this box is given in Appendix 10.2.

2.10.2 STM Tips

To achieve an STM image resolution at the atomic scale, atomically sharp and stable tips are vital. Tungsten is an ideal material for this and is the most widely used material for tip preparation. Tungsten is relatively hard, making it a stable probe material, and it can be electrochemically etched, allowing the preparation of atomically sharp tips (6).

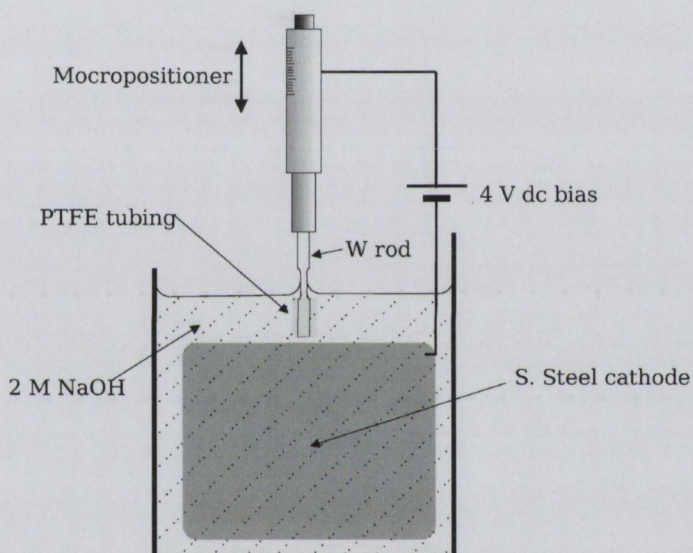


Fig. 2.13: Electrochemical etching set-up used to prepare the W STM tips.

STM images in this thesis were obtained with W tips, which were prepared using a chemical etching procedure described in detail elsewhere (31).

W tips are prepared from 0.5 mm thick wire. The wire is cut into small rods and a small insulating PTFE tube is placed on the end of the rod. The rod is then clamped into a modified micrometer screw, which allows precise positioning of the rod in a beaker of 2.0 M NaOH solution. The W wire acts as the anode while a submerged metal foil acts as the cathode. Under an applied 4 V DC bias, chemical etching occurs at the

air/electrolyte interface. The W oxidises to form soluble WO_4^{2-} , which flows away from the active etching region. This leads to a thinning of the wire at the interface region and eventually the submerged section of the wire falls off under its own weight.

During the etching process, the PTFE acts to physically restrict the active region (32) and also protects the tip that falls into the beaker. This tip etching set-up is shown in Fig. 2.13. The tips are then rinsed with propan-2-ol, placed in tip holders and inserted into UHV. The tips are then etched with Ar^+ ions to remove the WO_4^{2-} present from the chemical etching process. This process produces stable, atomically sharp tips.

Bibliography

- [1] D. Briggs and M. Seah, *Auger and X-ray Photoelectron Spectroscopy*, volume 1 of *Practical Surface Analysis*, Wiley, New York, second edition, 1990.
- [2] L. Davis, N. MacDonald, P. Palmberg, G. Riach, and R. Weber, *Handbook of Auger Electron Spectroscopy*, Physical Electronics Industries, Minnesota, second edition, 1976.
- [3] M. A. V. Hove, V. H. Wienberg, and C. M. Chan, *Low-Energy Electron Diffraction*, volume 6, Springer Verlag, Berlin, Springer Series in Surface Science, 1986.
- [4] G. Binning, H. Rohrer, C. Gerber, and E. Wiebel, *Phys. Rev. Lett.* **49**, 57 (1982).
- [5] C. J. Chen, *Introduction to Scanning Tunneling Microscopy*, Oxford University Press, New York, 1993, 1983.
- [6] R. Wiesendanger, *Scanning Probe Microscopy and Spectroscopy*, Cambridge University Press, Cambridge, 1994.
- [7] Simmons, *J. Appl. Phys.* **34**, 1793 (1963).
- [8] J. Bardeen, *Phys. Rev. Lett.* **6**, 57 (1961).
- [9] A. Chambers, B. Halliday, and J. Matthew, Short course in vacuum technology, Course booklet, Dublin City University, Dublin, 1998.
- [10] G. Kaye and T. Laby, *Physical and Chemical constants*, Wiley, London, 16 edition, 1995.
- [11] D. Hoffman, B. Singh, and J. T. III, *Handbook of vacuum science and technology*, Academic Press, London, 1998.
- [12] A. Quinn, *Development of an ultra-high vacuum scanning tunneling microscope*, Phd thesis, Physics Department, Trinity College Dublin, 1996.
- [13] A. Quinn, *Development of an Ultra-High Vacuum Scanning Tunneling Microscope*, PhD thesis, Trinity College Dublin, Ireland, 1996.
- [14] J. Osing, *Studies towards spin sensitive scanning tunneling microscopy*, Phd thesis, Physics Department, Trinity College Dublin, 1998.
- [15] S. Murphy, *Surface Studies of the Fe/Mo(110) and Fe/W(100) Epitaxial Systems.*, PhD thesis, Trinity College Dublin, Ireland, 2000.

- [16] VAT Vacuum Products Ltd., 235 Regents Park Road, Finchley, London, N3 3LG U.K.
- [17] Physical Electronics Inc. (formerly Perkin-Elmer), 6509 Flying Cloud Drive, Eden Prairie, Minnesota, 55344 U.S.A.
- [18] VG Microtech, The Birches Industrial Estate, Imberhorne Lane, East Grinstead, West Sussex RH19 1UB U.K.
- [19] Pfeiffer Vacuum GmbH, Emmeliusstrasse, D-35614 Asslar.
- [20] SAES Getters G.B. Ltd., 5 Suthern Court, South Street, Reading, Berkshire RG1 4QS U.K.
- [21] Omicron, Limberger Str. 75 D-65232 Taunusstein Germany.
- [22] Leybold Inficon Inc., Two Technology Place, East Syracuse, NY 13057-9714 U.S.A.
- [23] C. Seoighe, *Surface studies of magnetite (100)*, Phd thesis, Physics Department, Trinity College Dublin, 1999.
- [24] IRCON Inc., 7301 North Caldwell Avenue, Nilis, Illinois 60648 U.S.A.
- [25] P. V. Technology, Macclesfield SK11 OLR, UK.
- [26] P. E. I. (formerly Perkin-Elmer, 6509 Flying Cloud Drive, Eden.
- [27] D. Woodruff and T. Delchar, *Modern Techniques of Surface Science*, Cambridge Solid State Series, Cambridge University Press, second edition, 1994.
- [28] S. R. Systems, 1290-D REamwood Av., Sunnyvale, Caifornia 94089, USA.
- [29] S. H. Pan, Piezo Electric Motor. International Patent Publication No WO93/19194. International Bureau, World Intellectual Property Organisation.
- [30] I. Horcas et al., Rev. Sci. Instrum. **78**, 013705 (2007).
- [31] S. F. Ceballos, G. Mariotto, S. Murphy, and I. V. Shvets, Surf. Sci. **523**, 131 (2003).
- [32] H. Bourque and R. M. Leblanc, Rev. Sci. Instrum. **66**, 2695 (1995).

Chapter 3

Density Functional Theory

In this thesis we employ Density Functional Theory (DFT) calculations to aid interpretation of experimental results. Since this is a new technique for our research group, I have provided this chapter to review some of the main concepts of DFT. This chapter will outline the theoretical background of density functional and pseudopotential theory, as well as describe details specific to VASP (Vienna Ab-initio Simulation Package)(1). VASP is an ab-initio quantum-mechanical molecular dynamics (MD) software package that uses pseudopotentials and a plane wave basis set to calculate an electronic ground state. The DFT results in this thesis employed both VASP and CASTEP and although the description in this chapter is based on VASP, the concepts are in general universal to all DFT codes (2; 1).

First, we will introduce two key ideas that are used in the majority of electronic structure codes which use periodic boundary conditions, the Born-Oppenheimer approximation and Bloch's theorem. Then we will provide a description of the basics of density functional theory leading to the Kohn-Sham (KS) equations. Next, we will discuss the approximations for the exchange-correlation energy that must be made in order

to solve the KS equations. Furthermore, pseudopotential theory is used as a way to minimise the number of plane-wave basis functions necessary to describe all the features of a valence electron moving through the solid. In the final section, we introduce the molecular dynamics procedure based on the calculation of the Hellman-Feynman forces. The derived equations of motion determine the relaxation of the ions in the supercell towards the minimum energy configuration.

3.1 Born-Oppenheimer Approximation and Bloch's Theorem

In order to study our system of interacting electrons and nuclei, it is necessary to know the particle density. This requires us to construct a suitable many-body wavefunction for the system. In principle, this wavefunction is a function of time and all nuclear and electronic coordinates. However, by making one approximation, the system is simplified.

Because the nuclei are typically 2000 times more massive than the electrons, we can decouple the electronic and nuclear motion by saying that the electrons respond instantaneously to any change in nuclear coordinates. This approximation allows us to rewrite the full many-body wavefunction as the product of a nuclear and an electronic wavefunction. Since the electronic wavefunction only depends on the instantaneous nuclear configuration, and not on time, we can describe its behaviour with the time-independent Schrodinger equation. Since the nuclei are massive enough to be treated as classical particles, they respond to the electronic forces according to Newton's laws. This semi-classical approximation, coupled with adiabatic separation of variables, is called the Born-

Oppenheimer approximation.

If we confine our studies to periodic systems, we can further simplify the system with Bloch's theorem. This theorem says that any wavefunction, $\psi_{i,\mathbf{k}}$, of a periodic system must be the product of a cell-periodic part $u_j(\mathbf{r})$ and a phase factor, in order to preserve the translational symmetry of the density. The phase factor takes the form of a plane wave, $e^{i\mathbf{k}\cdot\mathbf{r}}$, whose wavevector is a linear combination of reciprocal lattice vectors, and $u_j(\mathbf{r})$ is written as:

$$u_j(\mathbf{r}) = \sum_{\mathbf{G}} c_{j,\mathbf{G}} e^{i\mathbf{G}\cdot\mathbf{r}} \quad (3.1)$$

where $\mathbf{G} \cdot \mathbf{r} = 2\pi m$, where m is an integer, \mathbf{r} are the crystal lattice vectors, $c_{j,\mathbf{G}}$ are the plane-wave coefficients, the subscript j indicates the band index and \mathbf{k} is a continuous wavevector that is confined to the first Brillouin zone of the reciprocal lattice. Since $u_j(\mathbf{r})$ has the same periodicity as the direct lattice, the electron wavefunctions can be expanded in terms of a linear combination of plane-waves,

$$\psi_{j,\mathbf{k}}(\mathbf{r}) = \sum_{\mathbf{G}} c_{j,\mathbf{k}+\mathbf{G}} e^{i(\mathbf{k}+\mathbf{G})\cdot\mathbf{r}} \quad (3.2)$$

Plane-wave expansions are a simple way of representing electron wavefunctions. They offer a complete basis set that is independent of the type of crystal and treats all areas of space equally. This has the additional advantage that the basis functions are orthogonal, and that operations on them are computationally efficient. In particular it is straightforward to Fourier transform our wavefunction from real to reciprocal space or vice versa.

Many of the systems we wish to study, such as a surface, are not pe-

riodic, and so we construct what is known as a supercell. This is essentially just a large unit cell, repeated periodically in space, but containing a "spacer" region to separate the region of interest from its periodic images. Typically the "spacer" is a vacuum. By using supercells to represent our system, we can take advantage of Bloch's theorem even for non-periodic systems. Clearly, we must ensure that our supercell is a good approximation of the original, aperiodic system, and this is done by checking that our results are invariant with respect to small changes in the supercell size.

3.2 Hohenberg-Kohn Theorem

The Hohenberg-Kohn theorems are the foundations of DFT. The Hohenberg-Kohn theorems relate to any system consisting of electrons moving under the influence of an external potential $v_{ext}(\vec{r})$. This functional has its minimum value for the correct ground-state electron density. The ground-state energy functional is written as:

$$E[n] = \int v_{ext}(\vec{r})n(\vec{r})d\vec{r} + F[n] \quad (3.3)$$

where v_{ext} is the external potential, i.e. the potential related to the positions of the nuclei. The central idea of the theorem is that there is a one-to-one correspondence between the electron density $n(\vec{r})$ and the external potential. The functional $F[n]$ includes all kinetic energy and electron-electron interaction terms. It is convenient to separately identify the energy due to the Coulomb-interaction, also called the Hartree-energy from $F[n]$:

$$F[n] = \frac{e^2}{8\pi\epsilon_0} \int \int \frac{n(\vec{r})n(\vec{r}')}{|\vec{r} - \vec{r}'|} d\vec{r}d\vec{r}' + G[n] \quad (3.4)$$

where e is the charge of the electron and ϵ_0 is the electric permittivity of vacuum. Since the exact form of $G[n]$ is unknown, the ground state of the system can be obtained by minimizing $E[n]$ with respect to varying the density while conserving N :

$$\int n(\vec{r})d\vec{r} = N \quad (3.5)$$

This leads to the variational equation:

$$\delta\{E[n] - \mu \int n(\vec{r})d\vec{r}\} = 0 \quad (3.6)$$

A Lagrange multiplier, μ , is introduced due to the constraints of equation 3.5. By applying Eq. 3.3, Eq. 3.4 and Eq. 3.6 the ground state can be determined by:

$$v_{ext}(\vec{r}) + \frac{e^2}{4\pi\epsilon_0} \int \frac{n(r')}{|r - r'|} dr' + \frac{\delta G[n]}{\delta n(\vec{r})} = \mu \quad (3.7)$$

where $\frac{\delta G[n]}{\delta n(\vec{r})}$ is the functional derivative of $G[n]$ with respect to $n(\vec{r})$. Now we need to assume a form for $G[n]$ in order to determine E .

3.3 Kohn-Sham (KS) Equations

Kohn and Sham developed a method resulting in one-particle equations, called the Kohn-Sham (KS) equations, which may be solved (3). Their idea was to consider a system of N non-interacting electrons in some external potential $v_{ext,s}(\vec{r})$. The ground-state density of this system is $n(\vec{r})$. The functional $F[n]$ in Eq. 3.4 reduces to $T_s[n]$, which is the

kinetic energy functional of non-interacting electrons. Now the equation determining $n(\vec{r})$ is given by:

$$v_{ext,s}(\vec{r}) + \frac{\delta T_s[n]}{\delta n(\vec{r})} = \mu_s \quad (3.8)$$

In this case, the general form of $T_s[n]$ is again unknown. However, in this case, there is a way to solve for $n(\vec{r})$. For the case of non-interacting electrons, the many particle ground state wavefunction is simply a product of single electron wavefunctions $\phi_i(\vec{r})$ that obey the time-independent Schrodinger equation:

$$\left\{ \frac{-\hbar^2}{2m} \nabla^2 + v_{ext,s}(\vec{r}) \right\} \phi_i(\vec{r}) = \epsilon_i \phi_i(\vec{r}), i = 1 \dots N, \quad (3.9)$$

where m denotes the electron mass. The density for this system of electrons is then given by:

$$n(\vec{r}) = \sum_{i=1}^N |\phi_i(\vec{r})|^2 \quad (3.10)$$

The ground state is found by selecting the N states, $\phi_i(\vec{r})$, that have the lowest energy ϵ_i . So for this particular system of non-interacting electrons, there is indeed a way of finding the solution to Eq. 3.8. This method is also valid for the case of interacting electrons (3). The functional $G[n]$ may be split into two terms:

$$G[n] = T_s[n] + E_{xc}[n] \quad (3.11)$$

The first term is still the kinetic energy of a system of non-interacting electrons with a density $n(\vec{r})$, and $E_{xc}[n]$ is called the exchange-correlation energy, which contains the information of the interacting system with

density $n(\vec{r})$. Equation 3.7 now becomes:

$$v_{ext}(\vec{r}) + \frac{e^2}{4\pi\epsilon_0} \int \frac{n(r')}{|r - r'|} dr' + \frac{\delta E_{xc}[n]}{\delta n(\vec{r})} + \frac{\delta T_s[n]}{\delta n(\vec{r})} = \mu \quad (3.12)$$

This equation has the form of 3.8 except $v_{ext,s}(\vec{r})$ is replaced by an effective potential $v_{eff}[n]$:

$$v_{eff}[n] = v_{ext}(\vec{r}) + e^2 4\pi\epsilon_0 \int \frac{n(r')}{|r - r'|} dr' + \frac{\delta E_{xc}[n]}{\delta n(\vec{r})} \quad (3.13)$$

As with the non-interacting case, the correct ground-state density of the interacting system is found by the self-consistent solution ($v_{eff}[n]$ dependent on $n(\vec{r})$) of the single-particle KS equations:

$$\left\{ \frac{-\hbar^2}{2m} \nabla^2 + v_{eff}(\vec{r}) \right\} \psi_i(\vec{r}) = \epsilon_i \psi_i(\vec{r}), i = 1 \dots N \quad (3.14)$$

$$n(\vec{r}) = \sum_{i=1}^N |\psi_i(\vec{r})|^2 \quad (3.15)$$

Therefore, the total ground-state energy of the electron system is:

$$E[n] = T_s[n] + \int v_{ext}(\vec{r}) n(\vec{r}) d\vec{r} + \frac{e^2}{8\pi\epsilon_0} \int \int \frac{n(\vec{r}) n(\vec{r}')}{|\vec{r} - \vec{r}'|} + E_{xc}[n] \quad (3.16)$$

where:

$$T_s[n] = - \sum_{i=1}^N \int \psi_i^*(\vec{r}) \left(\frac{\hbar^2}{2m} \nabla^2 \right) \psi_i(\vec{r}) d(\vec{r}) \quad (3.17)$$

Now we must adopt some explicit form for $E_{xc}[n]$ in order to find the self-consistent solution to Eq. 3.15 and to calculate $E[n]$.

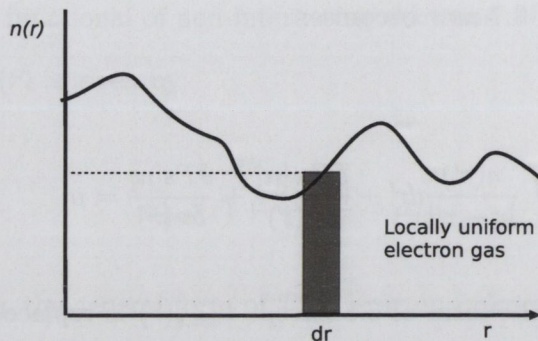


Fig. 3.1: Schematic diagram showing the principle of the local density approximation. For a given radial slab, dr , the local charge density is considered to be, $n(\vec{r})$, the density of an equivalent uniform homogeneous electron gas.

3.3.1 Local Density Approximation

The Local Density Approximation (LDA) is the simplest approximation of the exchange-correlation energy functional which was first used by Kohn and Sham (3). With the LDA, regions of space where the charge density is slowly varying the exchange-correlation energy can be considered as a locally uniform electron gas of the same charge density. The LDA functional assumes that the per-electron exchange-correlation energy at every point in space is that of the per-electron exchange-correlation energy of a homogeneous electron gas. This is written as:

$$E_{xc} = \int d^3\vec{r} n(\vec{r}) \left(\frac{-3e^2}{4\pi} \right) (3\pi^2 n(\vec{r}))^{\frac{1}{3}} \quad (3.18)$$

and represented by Fig. 3.1

Although this approximation is simple, it works very well. It even works reasonably well in systems where the charge density is rapidly varying. However it tends to under-predict atomic ground state energies and ionisation energies, while over-predicting binding energies. It is also known to greatly favour high spin state structures. For these reasons

there have been attempts to move beyond the LDA, notably through the addition of gradient corrections to incorporate longer range gradient effects (4). However in practice, although these improvements appear to result in better total energies, the resultant structure is often worse, and at a greatly increased computational cost. In general, the LDA is worse for small molecules and improves with system size.

3.3.2 Exchange-Correlation

The only remaining problem is to find an approximate solution for the homogeneous electron gas exchange-correlation term, $\varepsilon_{xc}(n)$. There are several parametrised methods for this and the one we used in VASP is based on the work by Ceperley and Alder (5).

The correlation energy for a homogeneous electron gas comes from a set of quantum Monte Carlo calculations performed by Ceperley and Alder (5). These were later parametrised by Perdew and Zunger (6).

The results of Ceperley and Alder apply to low density electron gases, and can be combined with results from perturbation theory for high density gases to cover a wide density range. Defining the correlation energy per electron, ε_c , polarisation ξ and Wigner-Seitz radius of each electron, r_s as:

$$E_c = \Omega n \varepsilon_c(n, \xi), \xi = \frac{(n_\uparrow - n_\downarrow)}{n}, r_s = \left(\frac{4\pi n}{3} \right)^{\frac{1}{3}}, \quad (3.19)$$

where n is the electron density, for the non-polarised ($\xi = 0$) and fully-polarised ($\xi = 1$) cases, ε_c is given by (6):

$$\varepsilon_c = \begin{cases} \gamma 1 + \beta_1 \sqrt{r_s} + \beta_2 r_s^{-1} & r_s \geq 1 \\ B + (A + Cr_s) \ln(r_s) + Dr_s & r_s < 1 \end{cases} \quad (3.20)$$

3.4 Pseudopotential Theory

In condensed matter systems most of the space in the cell can be described by smoothly varying electron wave functions. However, in the vicinity of atomic nuclei the electron orbitals tend to oscillate very rapidly. This requires us to set a very large cut-off energy, so that we include plane waves with very short wavelengths. Since most of the space doesn't require such a high cut-off, there is an unnecessarily high computational expense. In order to eliminate this we can use a pseudopotential where the core electrons, and the potential due to the nuclear charge, are replaced by a fictitious potential. This potential is defined such that the behaviour of the valence electrons is not affected outside of some cut-off radius from the nucleus. As long as this radius does not overlaps regions of space involved in chemical bonding, the pseudopotential approximation should not significantly alter the inter-atomic interactions characteristic of the condensed matter system. Furthermore, by removing the core electrons from the calculation, the number of Kohn-Sham orbitals is reduced. This reduces the memory required to store the orbitals, the time required to evaluate orbital-dependant quantities.

3.4.1 Projector Augmented-Wave Method

The electron wavefunctions of real materials have very different signatures in different regions of space. In the bonding region, the wavefunction is fairly smooth, whereas close to the nucleus, due to the large

attractive potential of the nucleus, it oscillates rapidly. It is difficult for electronic structure methods to accurately describe the bonding region while accounting for the large variations in the atom center. The augmented-wave methods divide the wavefunction into parts, namely, a partial-wave expansion within the atom centered sphere and an envelope function outside the sphere. The envelope function can be expanded into plane waves. The envelope function and partial-wave expansions are then matched with value and derivative at the sphere radius. The projector augmented-wave (PAW) method which is used by VASP was developed by Blöchl (7). The PAW uses a transformation that maps the valence wavefunctions onto pseudo wavefunctions that are to be identified as the envelope functions. This linear transformation gives pseudo wavefunctions that are computationally easy.

There are several benefits of the PAW method over pseudopotential methods. Firstly, all errors can be systematically controlled so that there are no transferability errors. This means that a traditional pseudopotential constructed from an isolated atom is not guaranteed to be accurate for a molecule. However, the converged results of the PAW method do not depend on a reference system such as an isolated atom, because it uses the full density and potential. The PAW method provides access to the full charge and spin density, which is relevant for hyperfine parameters. Hyperfine parameters are sensitive probes of the electron density near the nucleus. In many situations, they are the only information available that allows us to deduce atomic structure and chemical environment of an atom.

3.5 Relaxation of the Ionic System

Thus far, the determination of the electronic ground state has been considered in a system with fixed ionic positions. The positions of the ions and the size and shape of the unit cell can be included as dynamic variables in a Lagrangian, usually referred to as Car-Parrinello Lagrangian. This, along with the Euler equations of motion give the necessary equations for the relaxation of the system. In the Car-Parinello scheme, the Kohn-Sham energy functional $E[c_{n\mathbf{k}}]$ is a function of the set of coefficients of the plane-wave basis set $n\mathbf{k}$. Each coefficient $n\mathbf{k}$ is essentially the coordinate of a classical particle. To minimize the KS energy functional, these particles are given an initial kinetic energy and the system is gradually cooled until the set of coordinates reaches the values $n\mathbf{k}_0$ that minimize the functional. The Car-Parrinello Lagrangian has the form(8):

$$L = \frac{1}{2} \sum_i \mu \langle \dot{\psi} | \dot{\psi} \rangle + \sum_j \frac{1}{2} M_j \dot{R}_j^2 + \sum_v \frac{1}{2} \beta \dot{\alpha}_v^2 - E[\{\psi_i\}, \{R_j\}, \{\alpha_v\}] \quad (3.21)$$

where μ and β are artificial masses associated with the electronic wavefunctions (ψ_i) and coordinates defining the unit cell (α_v), E is the KS energy functional, and R_j is the position of ion j with mass M_j . The kinetic term is due to the fictitious dynamics of the electronic degrees of freedom, and the dynamics of the ions bound by the cell size and shape. The KS energy functional replaces the potential energy in a conventional Lagrangian formulation.

The equations of motion for the positions of the ions and the coordinates of the unit cell are given by:

$$M_j \ddot{\mathbf{R}}_j = -\frac{\delta E}{\delta \mathbf{R}_j} \quad (3.22)$$

$$\beta \ddot{\alpha}_v = -\frac{\delta E}{\delta \alpha_v} \quad (3.23)$$

The equations of motion for the degrees of freedom associated with the dynamics of the ions and of the unit cell can be integrated at the same time as the equations of motion for the electronic states and, as will be shown below, provide a method for performing ab-initio dynamical simulations of the ionic system. A relaxation of the ionic system can be performed using these equations simply by removing kinetic energy from the electronic system, the ionic system, and the motion of the unit cell. In this case, the system will evolve until the total energy of the system is minimized with respect to all of these degrees of freedom and the ionic configuration will have reached a local energy minimum. However, integration of the equations of motion for the ions and for the unit cell is not as straightforward as it first appears. This is because physical ground-state forces on the ions and integrated stresses on the unit cell cannot be calculated for arbitrary electronic configurations, as shown in the following section.

3.5.1 The Hellmann-Feynman Theorem

When an ion moves, the wavefunctions must change to the self-consistent KS eigenstates corresponding to the new position, in order for the KS energy functional to remain physically meaningful. These changes contribute to the force on the ion:

$$f_j = -\frac{dE}{d\mathbf{R}_j} = \frac{\delta E}{\delta \mathbf{R}_j} - \sum_i \frac{\delta E}{\delta \psi_i} \frac{d\psi_i}{d\mathbf{R}_j} - \sum_i \frac{\delta E}{\delta \psi_i^*} \frac{d\psi_i^*}{d\mathbf{R}_j} \quad (3.24)$$

from Eq. 3.22 we see that the force in the Lagrangian equation of motion is the partial derivative of the KS energy functional with respect to the ion position. This is not the physical force on the ion, but the force on the ion from the particular electronic configuration. However, according to the Hellmann-Feynman theorem, when each electronic wavefunction is an eigenstate of the Hamiltonian, the two final terms in Eq. 3.24 sum up to zero. Then the partial derivative of the KS energy with respect to the ion position gives the physical force on the ion (9; 10). Therefore, once the electrons are brought close to the ground state we can calculate forces and stresses on an ionic configuration. These calculated forces can then be used to calculate a new ion trajectory to update the ionic positions. This process is repeated until the required accuracy for the ground state is met.

Bibliography

- [1] G. Kresse and J. Furthmüller, Phys. Rev. B **54**, 11169 (1996).
- [2] S. Clark et al., Z.Kristallogr **220**, 567 (2005).
- [3] W. Kohn and L. J. Sham, Phys. Rev. **140**, A1133 (1965).
- [4] F. W. Kutzler and G. S. Painter, Phys. Rev. B **45**, 3236 (1992).
- [5] D. M. Ceperley and B. J. Alder, Phys. Rev. Lett. **45**, 566 (1980).
- [6] J. P. Perdew and A. Zunger, Phys. Rev. B **23**, 5048 (1981).
- [7] P. Blöchl, Phys. Rev. B **50**, 17953 (1994).
- [8] R. Car and M. Parrinello, Phys. Rev. Lett. **55**, 2471 (1985).
- [9] R. P. Feynman, Phys. Rev. **56**, 340 (1939).
- [10] H. Hellmann, *Einführung in die Quantenchemie*, Deuticke, Leipzig, 1937.

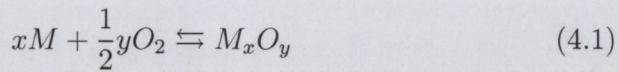
Chapter 4

Oxidation Theory

The study of the oxidation of metals has been a subject of considerable research effort for many years. In general, the explanation of the oxidation mechanisms for metals is split in two regimes based on the oxide thickness. For thick oxide films ($> 1\mu\text{m}$), oxidation is generally described by Wagner's theory. For thin oxide films ($< 50\text{nm}$), Cabrera and Mott theory is applied. These theories are all based on the kinematics of the reaction process, including the mechanisms involved in determining the oxidation rate.

In this chapter, I will give a basic overview of the oxidation processes that are relevant to the experiments detailed in the following chapters. Since the oxide films detailed in this thesis fall in the range of Cabrera and Mott theory, Wagner theory will not be discussed here. For a more detailed review of the principles governing the oxidation of metals, see the article by Lawless (1).

The general equation for the oxidation reaction of a metal is very simple. The driving force for this reaction, like all chemical reactions, is the free energy change associated with the formation of oxide from the reactants. This is written as



Since this is a thermodynamic relation, it cannot be used to determine the oxidation rate. Oxidation rates are based on kinetics, and therefore so is this discussion.

4.1 The Oxidation Process

The oxidation process involves a number of steps. First, the O_2 molecules reach the clean metal surface. These molecules are physisorbed at the surface via the Van-der-Waals-interaction between the oxygen and the metal atoms. The oxygen is then chemisorbed at the surface. This involves the dissociation of the O_2 molecules into atomic oxygen ($O_2 \rightarrow O + O$). Because of the large electronegativity of oxygen compared to metals, the dissociation is accompanied by a charge transfer from the metal to the oxide (this will be illustrated in chapter 6). As the oxygen concentration increases at the metal surface, it reaches a critical point and oxide clusters and islands start to nucleate. These oxide islands then coalesce laterally to a closed oxide layer. At this point the oxidation reaction now occurs at the oxide surface and may or may not continue.

4.1.1 Oxygen Adsorption

Before oxidation occurs, there is a process of physical and chemical adsorption of oxygen to the metal surface. This process proceeds at a rate that is related to the rate of collision of molecules with a unit area of surface. This is a product of the gas pressure p , the mass of the gas molecule m , Boltzmann constant k and T the absolute temperature.

$$p/(2\pi mkT)^{\frac{1}{2}} \quad (4.2)$$

From this, assuming that 100 % of the oxygen arriving to the surface sticks (sticking coefficient is 1.0), a monolayer of adsorbed gas will form on the surface in approximately one second at room temperature for a gas pressure of 10^{-6} Torr. Physical adsorption will occur on any surface at low temperatures. However, chemisorption takes place at temperatures well above the boiling point of the gas, and therefore is important to the oxidation process under most conditions of temperature and pressure.

The dissociation of molecular oxygen is also a necessary step in the chemisorption and oxidation process. Dissociation is linked to the energetic position of the O_2 orbitals with respect to the Fermi-level of the metal. Oxygen molecules possess one bonding π and one antibonding π^* orbital. In the ground state, the bonding orbital is occupied and the antibonding is empty. Therefore, the ability of a metal to dissociate molecular oxygen depends on the work function of the metal. Of all the metals, only noble metals like Pd or Au cannot dissociate the O_2 molecules into atomic oxygen, and oxidation is prevented.

This scenario gives three possibilities, either the antibonding orbital is situated above the Fermi-level of the metal; in which case, there is no charge transfer from the metal to the O_2 molecule, and only physisorption of the molecule via Van-der-Waals forces. The second possibility is that the antibonding orbital is situated partially below the Fermi-level, and a charge transfer partially fills the antibonding orbital with electrons. In this case, the oxygen still remains in the molecular state leaving charged chemisorbed O_2 molecules on the surface. However in most cases, it is the third possibility that occurs, in which the antibonding orbital is situated

below the Fermi-level and the O_2 molecules will dissociate and chemisorb on the metal.

A more detailed analysis of the oxygen adsorption process for transition metals, including the specific properties of the d-band electrons can be found in the literature (2; 3; 4).

4.1.2 Oxygen Incorporation

In order to further discuss the oxidation process we assume that the oxygen is dissociated and chemisorbed at the metal surface. The next step is for the oxygen to be incorporated into the metal, which can happen in one of two ways. Either, the chemisorbed oxygen layer will be located at a potential minima on the surface of the metal (a bonding site), causing a minimum amount of displacement of the metal atoms; or there can be a surface reconstruction in which both metal ions and oxygen ions will constitute the surface plane.

In most cases, at low oxygen exposures, somewhat disordered structures are observed prior to the formation of the first ordered structure. With this, the occurrence of two or more different surface structures or surface phases is not unusual. This ordering can usually be enhanced with a slight heating of a surface. If the surface is stable to reconstruction, the oxygen will eventually be incorporated into the metal by "place exchange". As oxygen is highly electronegative, giving it an electron affinity which is greater than the work function of a metal surface, electrons may be transferred to the adsorbate. Whether the electron transfer is complete or partial, a dipole is produced at the surface with the negative side outwards. As these dipoles accumulate on the surface, the electrostatic energy will build, eventually reaching a point that it will

overcome the activation energy required to flip the dipole. As this dipole is essentially made of a negative oxygen and a positive metal atom, when it flips, the oxygen will be incorporated into the metal surface layer.

4.1.3 Oxide Nucleation and Growth

As more oxygen is incorporated into the surface, the oxide will begin to nucleate. The nucleation of oxide at defect sites on the metal surface, such as at the terrace edges, is expected to occur at low oxygen pressures and temperatures. However, at elevated temperatures, it is expected to be homogeneous (1). Nucleation leads to the formation of both sub-oxide and true oxide on the metal surface, and is possible below the surface. During this process, the metal layers close to the surface are usually slightly expanded *i.e.* relaxed by the oxygen (1). Thus, it becomes easier to break open the metal bonds for the onset of the oxidation reaction.

The nucleation process is controlled by an activation energy which according to Cabrera should decrease as the oxygen pressure increases (5). Apart from the nucleation process, the movement of atoms also requires some activation energy. Reaching this energy level is obtained by increasing the temperature, and depending on the temperature and oxygen concentration on the surface, it is often possible to observe precursor states of the oxygen that result in the formation of surface reconstructions. In this case, the oxygen builds ordered superstructures until the critical concentration for oxide nucleation is reached. After the formation of oxide islands or clusters, oxidation usually continues laterally until the first oxide monolayer is closed (1).

4.2 Oxide Film Growth

Once there is a continuous oxide film formed on the metal surface, the oxidation process is now influenced by the oxide barrier between the reactants. The reaction can continue only if under the following conditions: either the cations, anions, or both need to be able to diffuse through the oxide layer to provide reactants. The electrons must be able to transfer from the metal to the oxide surface, and the surface must be able to dissociate the O_2 molecules in order to provide reactive oxygen. Otherwise, oxidation stops after the formation of a closed oxide layer and the oxide acts as a passivating layer.

If these criteria are met and the oxidation continues, the nature of the oxide barrier between the reactants will determine the rate limiting process of the oxide growth. These processes are related to the diffusion rates of both the ions and electrons necessary for the reaction to proceed. The theory for the oxidation of thin films was first developed by Cabrera and Mott and continued by Cook and Fromhold (5; 6). It describes the oxide growth perpendicular to the surface after the formation of a closed oxide layer, and up to oxide layer thicknesses of about one micrometer. The central issue of this theory is the development of a quantitative expression for the rate of increase in the oxide film thickness L with oxidation time t .

Since the oxide growth rate is closely connected to the transport and diffusion of electrons, holes, and ions through the oxide film, Mott focused on the individual oxide growth characteristics determined by one of the three following processes. 1). the electron or electron hole tunneling from the metal/oxide interface to the surface. 2). the thermoemission of electrons from the metal/oxide interface into the oxide conduction band

and subsequent diffusion to the surface. 3). and the ion diffusion of either positive metal ions or negative oxygen ions through the oxide layer.

When the oxide is ultra-thin and/or metallic the electron transfer is considered to take place relatively quickly and therefore the diffusion of cations or anions across the oxide film is usually much slower, limiting the oxide process. However, when the film is thicker, it becomes more likely that the electron transfer across the film can affect the reaction rate. The kinetics of the reaction mechanism are also a function of temperature and oxygen pressure as well as the crystal structure and physical properties of the oxide on the metal (5; 6).

Further effects such as grain boundary diffusion and the microstructure on material transport by short-circuit diffusion paths, pores due to condensation of vacancies, and cracks due to stresses within the oxide film may play a critical role (1). Furthermore, surface effects such as boundary concentrations and interfacial reactions that are related to the temperature and pressure as well as the specific chemical reactions must be considered (7). Since the reaction rate may be influenced by so many different factors, there are a multitude of rate laws reported in the literature (1). While the rate equations alone cannot be used to determine the oxidation mechanism, they can be useful to describe the possible mechanisms which must be considered.

While all three processes can occur at the same time, usually only one of them is predominantly limiting the oxide formation and thus determines the growth characteristics. Which of the three factors is the limiting one depends strongly on the oxidation conditions as well as the material properties. Some important parameters are the height of the band gap in the oxide layer (barrier height), the present thickness of the

oxide layer (barrier width), and the oxidation temperature (activation energy).

The electron current through the oxide can be due to two main effects, tunneling or thermoemission. For low temperatures, the oxidation process is typically electron tunneling limited, whereas in the case of high temperatures it is dominated by thermoemission of electrons (1). At low temperatures, a lack of thermal energy means electrons are unable to overcome the activation barrier required to reach the conduction band. Going to higher temperatures, thermoemission of electrons from the metal/oxide interface into the oxide conduction band is possible, such that the oxidation process usually becomes thermoemission limited (1).

The thickness of the oxide can also affect the growth characteristics (1). Thin oxide layers represent a reasonably narrow tunnel barrier width such that electron tunneling is the most probable process at the onset of perpendicular oxide growth. In contrast, for thick oxide films, one usually obtains thermoemission limited oxide growth due to the electron tunneling probability dropping exponentially with increased tunnel barrier width. In this case, the transport of electrons through the conduction band only weakly depends on the oxide thickness. In the following section, we will provide a more detailed discussion about these rate limiting processes.

4.3 Rate Limiting Models for Oxidation Processes

In this section, the basic models for the rate limiting processes are described. This description follows the review article "The oxidation of

metals” by Lawless (1)

4.3.1 Ion and Electron Current Density

In this section, we will describe the two expressions for the electron current density J_e , one for electron tunneling and one for thermoemission as well as the expression for the ion current density J_i . For the following considerations, one assumes that the metal is the diffusing ion species in the system. Up to an oxide thickness of 500 Å, locally charged areas can be neglected and we can assume charge neutrality. Thus, the ion current density J_i and the electron current density J_e in the oxide film globally cancel each other:

$$J_i + J_e = 0 \quad (4.3)$$

The oxide growth rate dL/dt is proportional to the current density of either the ions or electrons, depending on which process is the growth limiting one:

$$dL/dt = RJ_iJ_e \quad (4.4)$$

The parameter R is the oxide volume that one of the diffusing ions creates in the oxidation process. Integrating Eqn. 4.4 results in an expression for the oxide thickness L depending on the oxidation time t . The main theoretical issue is to find suitable functions that realistically describe the electron and ion current density through the oxide layer. This will be done in the following sections.

4.3.2 The Electronic Tunnel Current

In order to derive an expression for the electronic tunnel current density, we will use a simplified band structure of the metal-oxide-oxygen system, where there are no deformations or mirror charges considered at the interface (Fig. 4.1). A metal with a Fermi level E_F has a work function f_0 with respect to the vacuum level. It is covered with an oxide layer of thickness L with a band gap E_g . Oxygen molecules from the gas phase can dissociate and chemisorb on the oxide surface by populating a level lying f_{ox} below the vacuum. The lower edge of the oxide conduction band is situated χ_0 above the Fermi level of the metal and χ_{ox} above the chemisorption level of the oxygen. The oxygen level at the surface and the Fermi level of the metal compensate each other by a charge transfer from the metal (M^+) to the oxygen (O^-). As a consequence the so-called Mott-potential V_M

$$V_M = e^1(\chi_0 - \chi_{ox}) = e^1(f_0 - f_{ox}) \quad (4.5)$$

develops between the oxide surface and the metal/oxide interface. This potential is the driving force for ion diffusion and thus for the oxidation process as a whole. The charge transfer observed between the interface and the surface can be compared with the charge transfer occurring between two metals with different work functions. In this case the Mott-potential corresponds to the contact potential between the two metals.

At low temperatures and for thin oxide layers, the electron current due to thermoemission into the oxide conduction band can be neglected. In this case, the only transport mechanism is quantum mechanical tunneling of the electrons through the barrier represented by the oxide layer. The

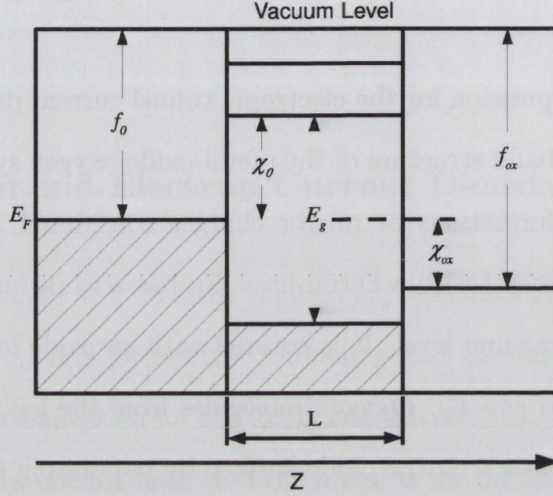


Fig. 4.1: Diagram of the band structure of a metal-oxide-oxygen system.

height of the tunnel barrier is determined by χ_0 and χ_{ox} , while its width is given by the oxide layer thickness L . We have to take into account, that the effective mass m of the tunneling electrons can deviate from m_e . Assuming a trapezoidally shaped potential within the oxide layer, we obtain the following expression for the electronic tunnel current density (8; 9; 6):

$$J_e = \frac{1}{8\pi^2 \hbar L(t)^2} \left[(2\chi_0 + eE_{ox}L(t)) \exp\left(-\frac{2\sqrt{m^*}}{\hbar} \sqrt{2\chi_0 + eE_{ox}L(t)}\right) - (2\chi_{ad} + eE_{ox}L(t)) \exp\left(-\frac{a\sqrt{m^*}}{\hbar} 2\chi_{ad} + eE_{ox}L(t)\right) \right]$$

Here E_{ox} is the electric field in the oxide layer due to the Mott-potential. However, in order to calculate the growth function $L(t)$, an expression for the ion current is also needed and will be derived in section 4.3.4.

From experimental observation of oxidation with an electron tunneling current-limited growth mode, one typically observes a quadratic

increase in the oxide thickness at the onset of growth. This is due to the small tunneling barrier associated with the very first layers of oxide, resulting in an ion current density limiting type growth. As the oxide continues to grow, electron tunneling becomes the limiting process and the rapid growth slows exponentially to a logarithmic oxide growth, $L(T) \approx \log(t)$. Finally, the growth rate approaches zero and the oxide acts as a protective layer against further oxidation.

4.3.3 The Thermal Electron Current

At high temperatures, a significant number of electrons can have the energy required to pass over the energy barrier χ_0 from the metal into the oxide conduction band. This results in insignificant electron tunneling, and the growth process becomes dominated by thermoemission. However, if χ_0 is too large, the oxidation process stops at the point where electron tunneling becomes improbable. Here, we will consider only the electron current that is created by thermoemission. Due to the presence of an electric field, the emission process is called Schottky-Emission and is described via the modified Richardson-Dushman Relation (8; 10):

$$J_e = AT^2 \exp(\chi_0/k_B T) \exp\left(-\sqrt{\frac{e^3 E_{ox}/4\pi\epsilon_0 K}{k_B T}}\right) \quad (4.6)$$

where A is the Richardson-Dushman constant, K the dielectric constant of the oxide and k_B and T are the Boltzmann constant and the absolute temperature, respectively. Comparing this expression with the electron tunneling current (Eqn. 4.6), there is a key difference. While the electron tunneling current depends on the the oxide layer thickness (tunnel barrier width), the thermal electron current current does not. This is due to

the electrons being thermally activated into the oxide conduction band. Once in the conduction band, the electrons can move quasi free through the oxide independently of the oxide thickness. This assumes that their diffusion time (obtained from the diffusion length and velocity) is short compared to their recombination time. As a consequence, we obtain a linear growth of the oxide thickness $L(t)$ with oxidation time. Substituting Eqn. 4.6 and 4.11 into Eqn. 4.3 and Eqn. 4.4 results in the following transcendental equation for $L(t)$:

$$\gamma t = L \left(1 - \frac{\alpha}{\sqrt{L}} \right) \exp \left(-\frac{\alpha}{\sqrt{L}} \right) + \alpha^2 I_1 \left(\frac{\alpha}{\sqrt{L}} \right) \quad (4.7)$$

The parameters γ and α are defined as

$$\alpha = \frac{1}{k_B T} \sqrt{\frac{e^3 V_0}{4\pi \epsilon_0 K}} \quad (4.8)$$

$$\gamma = \frac{AR}{Z_i} T^2 \exp \left(-\frac{\chi_0}{k_B T} \right) \quad (4.9)$$

I_1 is the integral given by

$$I_1(\eta) = \int_{\eta}^{\infty} \frac{e^{-\xi}}{\xi} d\xi \quad (4.10)$$

A more detailed description and derivation can be found in (10).

With this type of growth, one observes the oxide thickness increasing quickly due to the high electric field E_{ox} present in thin oxide films at the onset of oxidation. This field reduces the work function at the metal/oxide interface significantly (Schottky Effect) and thus induces an increase in the electron current density. With growing oxide thickness, E_{ox} drops ($E_{ox} = V_0/L$) and the electron current through the oxide layer reaches a value that is independent of the thickness L resulting in a lin-

ear growth behaviour. The slope of the linear part increases rapidly with rising oxidation temperature.

For example, at room temperature, Al_2O_3 is an insulator with a band gap of 8 eV. Therefore, at low temperatures, one obtains a logarithmic rate associated with electron tunneling current limited growth, as mentioned above. However, for temperatures higher than 1000 K, thermoemission of electrons begins to dominate the growth behaviour and typical thermoemission limited growth behaviour with a linear rate is seen (10).

In semiconducting oxide layers with a small band gap or metallic oxides, the electron current J_e is commonly much higher than the ion current J_i . Thus, such systems are often limited by the ion transport through the oxide layer (ion current limited oxide growth). In contrast, oxides with a well ordered structure and a large band gap with no defect levels usually exhibit an electron current limited oxide growth (1).

4.3.4 The Current For Ion Diffusion

Now we will discuss the effects of ion diffusion on the oxidation rate. In this discussion, we assume that the O_2 molecules are dissociated and charged at the oxide surface with the oxide layer itself in between the O_2 and M^+ ions. Therefore, either oxygen or metal ions must diffuse through the oxide layer in order to keep the oxidation process running. The driving force for this diffusion is the Mott-potential created between the negatively charged surface and the positively charged interface (5). The strength of this potential depends on the difference in electronegativity between the electropositive metal and the electronegative oxygen. If the Mott-potential is strong enough, it will push one of the two ion species

through the oxide layer and the oxidation process will continue.

Depending on the diffusing species, the oxidation front is located either at the surface (M^+ ions are diffusing) or at the metal/oxide interface (O^- ions are diffusing). In some cases, it is also possible that both species diffuse simultaneously through the oxide. Then the oxidation process can occur, in principle, anywhere within the oxide layer. According to Cook and Fromhold, the current density of the ion diffusion J_i is related to the oxide defect density $C(z)$ perpendicular to the surface. It is described by the following function (11; 9):

$$J_i = 2a\nu_i \exp\left(\frac{-W_i}{k_B T}\right) \sinh\left(\frac{Z_i e E_{ox} a}{2k_B T}\right) \frac{C_i(L) - C_i(0) \exp(Z_i e E_{ox} L(t)/k_B T)}{1 - \exp(Z_i e E_{ox} L(t)/k_B T)} \quad (4.11)$$

Here a is the ionic jump distance in the oxide layer, which is equal to the spacing between two interstitial sites where an ion can be situated, ν_i is the ionic attempt frequency for a jump from one lattice site to a neighboring one and W_i is the activation energy for the ion diffusion. The parameters $C_i(L)$ and $C_i(0)$ are the bulk defect concentration (interstitials or vacancies) at the surface ($z = L$) and at the metal/oxide interface ($z = 0$), respectively. E_{ox} is the electric field in the oxide which is assumed to be homogeneous over the complete layer thickness. Z_{ie} describes the effective charge per particle of the species diffusing through the oxide layer and k_B and T are the Boltzmann constant and the absolute temperature, respectively. J_i is determined by solving the differential diffusion equation

$$J_i = -D_{eff} \frac{dC(z)}{dz} + \mu E_{ox} C(z) \quad (4.12)$$

for $C(z)$ under the condition $\frac{Z_i E_{ox} a}{2k_B T} \ll 1$. Here $D_{eff} = a^2 \nu \exp(\frac{-W_i}{k_B T})$ is the diffusion coefficient and $\mu = \frac{D Z_i e}{k_B T}$ (Einstein relation) is the zero-field mobility. A more detailed derivation of J_i can be found in the book "Theory of Metal Oxidation" by Fromhold (7).

The electric field E_{ox} due to the Mott-potential is the driving force for ion diffusion. Since we are assuming a homogeneous charge through the oxide, the corresponding electric field E_{ox} is constant and thus independent of the oxide layer thickness L . With the approximation ($E_{ox} = const$), we can obtain an expression for $L(t)$ by substituting Eqn. 4.11 into Eqn. 4.4. With the assumed constant electric field in the oxide, the integration of Eqn. 4.4 can be carried out, and we obtain a transcendent equation for $L(t)$ (7):

$$1 + \beta t = \exp(\alpha L) \alpha L \quad (4.13)$$

where α and β are defined as

$$\alpha = \frac{Z_i e}{k_B T} E_{ox} \quad (4.14)$$

$$\beta = \left(\frac{Z_i e E_{ox}}{k_B T} \right)^2 RDC_{max} \quad (4.15)$$

this equation can be solved numerically with the Newton method, and for $\alpha L > 1$ we obtain $\exp(\alpha L) \gg \alpha L$ and αL on the right side of Eqn. 4.13 can be neglected. Thus, an approximated but explicit solution can be given for $L(t)$:

$$L(t) = \frac{1}{\alpha} \ln(1 + \beta t) \quad (4.16)$$

Therefore, the ion current through the oxide film leads to a logarithm-

mic growth of the oxide. At the early stages of oxidation, the oxide thickness increases very rapidly independent of the temperature. This growth rate quickly changes into a logarithmic mode and finally approaches a constant value. This growth mode is qualitatively similar to that of the tunnel current limited growth type. However, there is a key distinguishing difference between the two. Since ion limited growth is induced by a thermal activation of the ion current, the oxide layer reaches a constant thickness that depends on the oxidation temperature, whereas for tunnel current limited growth the final thickness of the oxide layer is independent of the oxidation temperature. For a typical example of this type of growth, see the oxidation of Cr(110) to Cr_2O_3 (12).

4.4 Linear Rate Laws

There are also several other types of rate laws described in the literature. In this section, we will describe linear rate laws that will be useful in the following chapters. Linear rate laws for oxide growth in the thin film region have been occasionally observed. These laws are generally explained on the basis of a rate limiting phase boundary reaction. This boundary may be located at either the oxide-metal interface or the oxide-gas interface

4.4.1 Deal and Grove Rate Law

The oxidation of Si is one classic example of this type of oxidation. The initial growth process is thought to be logarithmic at room temperature and for very thin oxide films. However, it changes to a linear then parabolic growth at elevated temperatures (13; 14). Deal and Grove ex-

plained the linear-parabolic growth on the basis of a model which involved the following, the incorporation of oxygen molecules at the oxide-oxygen interface with the oxygen flux across the interface being given by:

$$F_1 = h(C^* - C_0), \quad (4.17)$$

where h is the gas phase transport coefficient, C^* is the equilibrium concentration of oxygen molecules and C_0 is the actual molecular concentration in the solid at the interface. The transport of the oxygen molecule through the oxide with the flux being given by Fick's law:

$$F_2 = D_{eff}dC/dx, \quad (4.18)$$

and direct reaction of the molecule with Si, expressed as:

$$F_3 = kC_i, \quad (4.19)$$

where C_i is the molecular oxygen concentration at the Si-SiO₂ interface. Making the steady state assumption, the rate equation was derived as

$$\frac{dx}{dt} = \frac{kC^*N_1}{1 + k/h + k/D_{eff}} \quad (4.20)$$

where x is the thickness of the oxide, C^* is related to the oxygen pressure by Henry's law, N_1 is the number of oxidant molecules incorporated into unit volume of oxide, k is the rate constant for the oxygen-silicon interface reaction, and D_{eff} , is the effective diffusion coefficient for oxygen molecules in the oxide (15). Integration of this equation gives a rate law of the form

$$x^2 + Ax = B(t + \tau) \quad (4.21)$$

where A , B and τ are constants. It was concluded that if the oxide thickness was less than $1/2A$, where

$$A = \frac{2D_{eff}}{1/k + 1/h} \quad (4.22)$$

then the oxidation was linear and if greater than $1/2A$, it approached the parabolic law. In this model, the pressure dependence is linear for both the linear and parabolic stages of the oxidation.

4.4.2 Surface-Controlled Linear Growth

Furthermore, linear rate laws may also result if the oxide contains macroscopic pores or cracks such that the diffusion of metal ions to the surface can be rapid and independent of film thickness. In this case, the reaction rate will be limited by the surface reactions of oxygen adsorption, decomposition, and the oxidation reaction. These processes are dependent on temperature and pressure alone leading to a time independent growth rate:

$$L(t) = k't \quad (4.23)$$

where the rate constant k' can depend on the temperature and pressure of the system. Therefore, a linear rate may continue to any thickness as long as the oxide remains porous (7; 16).

The rate may also be linear for a non-porous film if the rate of diffusion through the oxide is faster than the phase boundary reaction, but since the diffusion rate decreases with increasing oxide thickness, a linear law

would hold only until the diffusion rate becomes comparable with the rate of the phase boundary reaction (17).

4.5 Oxidation Studies of Molybdenum

There have only been a few studies of the oxidation of Mo(110) as well as Mo(100) and Mo(112). The initial studies of the oxygen adsorption on the Mo(110) surface were performed by Bauer and Poppa using LEED and AES (18). By exposing the Mo surface to 1×10^{-9} Torr oxygen at room temperature they determined the sticking coefficient to be rather low (0.5) with a maximum oxygen coverage $\theta \approx 1/2$, leading to a rather complex LEED pattern. At elevated temperatures of 1200K they were able to reach saturation, $\theta \approx 1$, again with a complex LEED pattern which without real space imaging, they were unable to characterise.

Another attempt to characterise the oxidation of Mo(110) was made by Gotoh and Yanokura (19; 20). In their first paper on the subject, they annealed the Mo(110) surface at 1150 K at 1×10^{-6} Torr oxygen and observed 3-dimensional MoO₂ crystalites that formed on the surface. After annealing up to 1400 K, these crystalites evaporated and reformed a 2-dimensional ordered phase on the surface. With only RHEED data to work with they were unable to completely determine the oxide growth epitaxy. A later paper by the same group and again using RHEED, described the 2-dimensional ordered structures mentioned in the previous paper as ordered domains that run along the Mo[1-1 3] and [1-1-3] directions. Again, due to a lack of real space imaging, the authors had difficulty in describing these surface oxide phases.

In the following chapters we fully describe these oxide phases, in ad-

dition to demonstrating them as a mechanism to produce regular arrays of nanostructures on the Mo(110) surface. This is done through the use of LEED, STM and DFT calculations.

Bibliography

- [1] K. R. Lawless, Rep. Prog. Phys. **37**, 231 (1974).
- [2] A. Gross, M. Scheffler, M. J. Mehl, and D. A. Papaconstantopoulos, Phys. Rev. Lett. **82**, 1209 (1999).
- [3] A. Zangwill, (1988).
- [4] C. Stampfl, H. J. Kreuzer, S. H. Payne, H. Pfnür, and M. Scheffler, Phys. Rev. Lett. **83**, 2993 (1999).
- [5] N. Cabrera and N. F. Mott, Rep. Prog. Phys. **12**, 163 (1949).
- [6] A. T. Fromhold and E. L. Cook, Phys. Rev. **158**, 600 (1967).
- [7] A. T. J. Fromhold, *Theory of metal oxidation*,, volume Vol. I, North-Holland, Amsterdam, The Netherlands,, 1976.
- [8] A. T. Fromhold and E. L. Cook, Phys. Rev. **163**, 650 (1967).
- [9] A. T. Fromhold and E. L. Cook, Phys. Rev. **175**, 877 (1968).
- [10] A. T. Fromhold and E. L. Cook, Phys. Rev. Lett. **17**, 1212 (1966).
- [11] A. K. Vijh, *Theory of Metal Oxidation, Vol 1—Fundamentals*, volume 14, AVS, 1977.
- [12] A. Stierle et al., Science **303**, 1652 (2004).
- [13] G. Oertel and E.-H. Weber, Physica Status Solidi (a) **43**, 141 (1977).
- [14] B. E. Deal and A. S. Grove, J. Appl. Phys. **36**, 3770 (1965).
- [15] U. R. Evans and C. V. King, J. Electrochem. Soc. **108**, 94C (1961).
- [16] T. B. Grimley and B. M. W. Trapnell, Proc. R. Soc. London, Ser. A **234**, 405 (1956).
- [17] K. Hauffe, *Oxidation of Metals*, Plenum, , New York, 1965.
- [18] E. Bauer and H. Poppa, Surf. Sci. **127**, 243 (1983).
- [19] M. Kamei, T. Obayashi, H. Tsunematsu, Y. Tanaka, and Y. Gotoh, Surf. Sci. **356**, 137 (1996).
- [20] Y. Gotoh and E. Yanokura, Surf. Sci. **287-288**, 979 (1993).

Bibliography

- 1. K. H. ...
- 2. A. G. ...
- 3. A. ...
- 4. ...
- 5. ...
- 6. ...
- 7. ...
- 8. ...
- 9. ...
- 10. ...
- 11. ...
- 12. ...
- 13. ...
- 14. ...
- 15. ...
- 16. ...
- 17. ...
- 18. ...
- 19. ...
- 20. ...

Part II

Experimental Results

Chapter 5

Background

In this chapter, a background of the materials studied in this thesis is given. In the first section, a brief overview of molybdenum and the Mo(110) surface is discussed. For a more detailed discussion of the Mo(110) surface see (1). In the second section, a more detailed description of MoO₂ will be given, including the crystallographic structure, and the electronic and optical properties. This will include experimental values of these properties as reported in the literature in addition to the values we have calculated with DFT. Furthermore a comparison will be made between the two in order to validate the reliability of our DFT calculations for this oxide.

5.1 Molybdenum

Molybdenum, from the Greek meaning "lead-like", is a chemical element with the symbol Mo and atomic number 42. The electronic configuration of Mo is [Kr] 4d⁵ 5s¹. It was discovered in 1778 by Carl Wilhelm Scheele and first isolated in 1781 by Peter Jacob Hjelm. With a density of 10.280 g/cm³ and a melting point at 2896K, giving it the sixth highest melting

point of any element, it is often used in high-strength steel alloys.

Molybdenum has a bcc (body-centred cubic) crystal structure, space group $Im\bar{3}m$ (Space group number: 229) with cell parameters $a = b = c = 3.147 \text{ \AA}$ and cell angle $\alpha = \beta = \gamma = 90.00^\circ$.

Because of a well established cleaning procedure compared to other metals, Mo has been widely used as a substrate for surface science studies (2; 3).

5.1.1 The Mo(110) Surface

The densely packed Mo(110) surface is known to be the lowest energy surface of Molybdenum (4). The bcc (110) surface presents a distorted hexagonal primitive unit cell but it is often convenient to describe this surface using the centered rectangular unit cell highlighted in Fig 5.1.1.

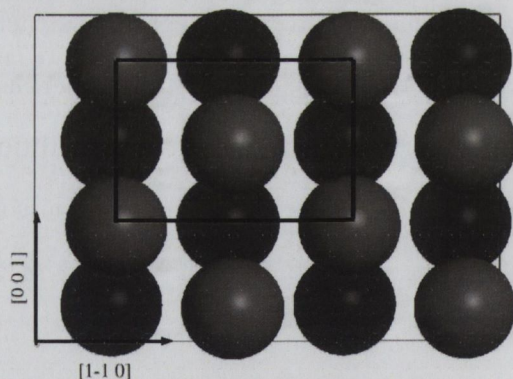


Fig. 5.1: A diagram of the Mo(110) surface. The centered rectangular unit cell is highlighted by the black box. The grey and black spheres represent the surface and second atomic layer atoms, respectively.

The Mo(110) single crystals used in these studies were obtained from Surface Preparation Laboratory and were grown by the floating-zone method. The sample was prepared from a 5N purity single Mo crystal by Rene Koper of the Surface Preparation Laboratory, The Netherlands (5).

As-grown 5N purity crystals of refractory metals such as Mo, typically contain bulk impurities (C, K, S, *etc.*) in concentrations of a few parts per million. The surface was oriented to within 0.1° of the (110) crystal plane and finished by mechanical polishing to a surface roughness of $0.03 \mu\text{m}$. The sample was fixed in a sample-holder with a Ta cap and inserted into the UHV system described previously (Chapter 2 section 2.6).

The typical procedure for cleaning refractory metal surfaces involves annealing the crystal in an O_2 atmosphere of partial pressure $1 \times 10^{-7} \leq P_{\text{O}_2} \leq 1 \times 10^{-6}$ Torr at elevated temperatures $\sim 1200\text{-}1300 \text{ K}$. At these temperatures, the bulk impurities diffuse to the surface where they form chemically stable oxides. These oxides, along with the surface oxide, are then removed by flash-annealing the surface to very high temperatures, in the range $2200\text{K} \leq T_{\text{flash}} \leq 2600\text{K}$ for short periods (5-30 seconds) under UHV conditions. These flashes are accompanied by sharp pressure bursts in the vacuum, with some time between flashes to allow the sample to cool and the vacuum to recover.

Initially, the surface was oxidised by annealing at $1300 \text{ K} \leq T \leq 1550 \text{ K}$, in an oxygen atmosphere of partial pressure 1×10^{-6} Torr, for 30 to 60 minutes. The sample was then flash-annealed to temperatures reaching $2400 \pm 200 \text{ K}$ for 15 to 20 seconds to remove the oxide layer. It was then left to cool for 5 to 10 minutes before the next flash, which allowed the chamber pressure to recover to the low 10^{-10} Torr. This cycle was repeated several times, with flash times gradually shortened to a few seconds, before the next oxidising cycle was begun. LEED and AES analysis were used to assess the cleanliness and structural order of the surface. After considerable repetition (\sim seventy oxidising cycles) of

this procedure, it was found that a carbon peak did not appear above the detection limit of the auger system, indicating a concentration below 1 %.

It should be noted that the main *LMM* Auger transition for sulphur at 152 eV is obscured by a molybdenum peak at 148 eV. While this means that the presence of sulphur contamination cannot be completely excluded, the cleaning procedure was assumed to produce concentrations of the same order as the carbon level. Oxygen peaks were found to persist in Auger spectra taken on the surface at this point. As a result, the oxidising treatment was abandoned and further cleaning of the surface was carried out by flash-annealing alone. The LEED and Auger spectra of the clean Mo(110) surface can be seen in Figs. 5.2 and 5.3.



Fig. 5.2: LEED image of the clean Mo(110) surface taken at 147eV. The Mo[001] direction is marked by the arrow.

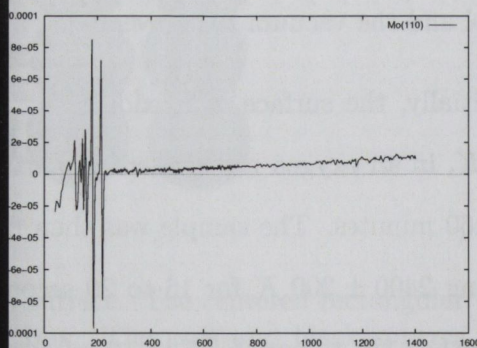


Fig. 5.3: AES spectra of a clean Mo(110) surface. The main Mo peaks are at 180 and 220eV

5.2 MoO₂

Molybdenum IV oxide (MoO₂) is a very interesting material which displays both high electrical conductivity and high transmittance in the visible region(6). These properties, which are uncommon for an oxide, make MoO₂ an important material for both scientific studies as well as industrial applications(6; 7; 8). First, we will give a discussion of the crystallographic structure of MoO₂. Next, the electronic and optical properties of MoO₂ will be described. This discussion will contain both experimental and theoretical results from the literature in addition to our own DFT calculations. A comparison is made between the two as an attempt to validate the accuracy of our DFT calculations. These calculations will be used in later chapters along with our experimental results.

5.2.1 Crystal Structure

MoO₂ crystallizes in a simple monoclinic lattice with space group P21/c (C5 2h) (Fig. 5.4) (9). The lattice constants and monoclinic angle are $a = 5.6109 \text{ \AA}$, $b = 4.8562 \text{ \AA}$, $c = 5.6285 \text{ \AA}$, and $\beta = 120.95^\circ$, respectively (9). This structure is a slight deviation from the rutile structure. This deviation is a result of a pairing of the metal atoms parallel to the monoclinic a axis in a lateral, zigzag, displacement. This pairing can be seen in the diagram of the MoO₂ crystal structure displayed in Fig. 5.4.

The unit cell, which is highlighted by thick solid black lines, comprises four formula units (Fig. 5.4). The Mo atoms along with the two nonequivalent oxygen atoms occupy the general Wyckoff positions (4e): $\pm(x, y, z)$, $\pm(x, 1/2 - y, 1/2 + z)$ with the parameters listed in Table 5.1.

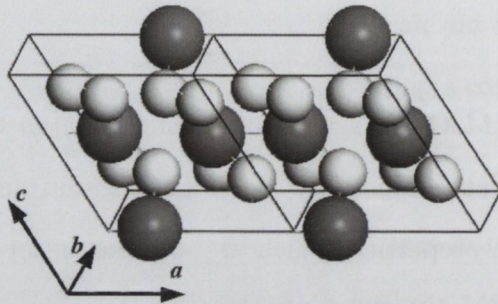


Fig. 5.4: The crystal structure of MoO_2 . Note the pairing of the metal atoms parallel to the monoclinic a axis.

Atom	Wyckoff Positions	x	y	z
Mo	(4e)	0.2316	-0.084	0.0164
O ₁	(4e)	0.1123	0.2171	0.2335
O ₂	(4e)	0.3908	-0.3031	0.2987

Table 5.1: Wyckoff positions of the atoms in the MoO_2 unit cell.

Using standard notation, the primitive translations are:

$$a_{M1} = \begin{pmatrix} 0 \\ 0 \\ -a_M \end{pmatrix} \quad a_{M2} = \begin{pmatrix} -b_M \\ 0 \\ 0 \end{pmatrix} \quad a_{M3} = \begin{pmatrix} 0 \\ c_M \sin \beta \\ -c_M \cos \beta \end{pmatrix} \quad (5.1)$$

giving a unit cell with dimensions and atomic positions listed in tables 5.2 and 5.3.

Unit Vectors (\AA)			
	x	y	z
a	5.61	0	0
b	0	4.86	0
c	-2.89	0	4.83

Table 5.2: Dimensions of the bulk MoO_2 unit cell.

Atomic Positions (Å)			
O ₁	1.33	3.38	1.44
O ₂	-0.05	1.05	1.13
O ₃	2.84	0.96	0.97
O ₄	4.21	3.48	1.29
O ₅	1.39	1.47	3.39
O ₆	2.76	3.8	3.7
O ₇	-0.12	3.9	3.86
O ₈	-1.49	1.37	3.54
Mo ₁	1.25	4.82	0.08
Mo ₂	2.91	2.39	2.33
Mo ₃	1.46	0.04	4.75
Mo ₄	-0.2	2.47	2.49

Table 5.3: Atomic positions of the Mo and O atoms in the bulk MoO₂ crystal.

DFT Calculated Structure

We performed a structural relaxation of the MoO₂ unit cell with VASP and compared the resulting structure with reference data (9). For these calculations, we used PAW pseudopotentials and the LDA. Convergence tests showed a (6x6x6) k-point grid was adequate. The cell consisted of one MoO₂ unit containing 12 atoms. The cell was allowed to relax by minimizing the total forces on each ion to less than 0.01eV/Å. The relaxed structure had dimensions of $a = 5.574$ Å, $b = 4.902$ Å, $c = 5.648$ Å, and $\beta = 120.741^\circ$ degrees, in excellent agreement with the bulk values. The dimensions of the unit vectors and atomic positions, along with the percent change from the experimental values, is listed in Tables 5.4 and 5.5.

5.2.2 Electronic Structure

Most of the experimental studies published on MoO₂ have focused on its atomic and electronic structure, with a motivation to understand the

Unit Vectors (Å)			
	x	y	z
<i>a</i>	5.57 (0.33%)	0 (0.00%)	0 (0.00%)
<i>b</i>	0 (0.00%)	4.9 (-0.47%)	0 (0.00%)
<i>b</i>	-2.89 (0.13%)	0 (0.00%)	4.85 (-0.28%)

Table 5.4: Dimensions of the MoO₂ unit cell after DFT relaxation.

Atomic Positions (Å)			
O ₁	1.32 (0.45%)	3.4 (-0.21%)	1.42 (0.63%)
O ₂	-0.04 (1.50%)	1.05 (0.08%)	1.16 (-1.26%)
O ₃	2.81 (0.37%)	0.95 (0.45%)	0.99 (-0.95%)
O ₄	4.18 (0.41%)	3.5 (-0.30%)	1.26 (1.11%)
O ₅	1.37 (0.62%)	1.5 (-1.06%)	3.42 (-0.48%)
O ₆	2.73 (0.55%)	3.85 (-0.62%)	3.69 (0.20%)
O ₇	-0.13 (-3.33%)	3.95 (-0.70%)	3.85 (0.06%)
O ₈	-1.49 (0.17%)	1.4 (-0.89%)	3.58 (-0.60%)
Mo ₁	1.24 (0.56%)	4.86 (-0.46%)	0.08 (1.44%)
Mo ₂	2.89 (0.32%)	2.41 (-0.45%)	2.34 (-0.06%)
Mo ₃	1.45 (0.51%)	0.04 (-1.96%)	4.76 (-0.17%)
Mo ₄	-0.21 (-2.55%)	2.49 (-0.50%)	2.5 (-0.23%)

Table 5.5: Atomic positions of the Mo and O atoms after DFT relaxation of the MoO₂ crystal.

nature of its atypical metallic and optical properties. Through the use of UPS, XPS, optical reflectivity measurements, and DFT calculations the electronic structure of MoO₂ is now well understood (6; 10; 9; 7). The origin of the unusual properties derive from the existence of cation-cation interactions via a direct interaction of the Mo d-electron wave functions. Using molecular orbital theory, a model for the energy band diagram resulting from this interaction was first proposed by Goodenough (11). This model was later confirmed and refined with ultraviolet and x-ray photoemission spectroscopy to the form presented in Fig. 5.5 (12; 10).

Fig. 5.5 shows a schematic of the energy level diagram restricted to the interactions between the atomic Mo 4d and the O 2p orbitals.

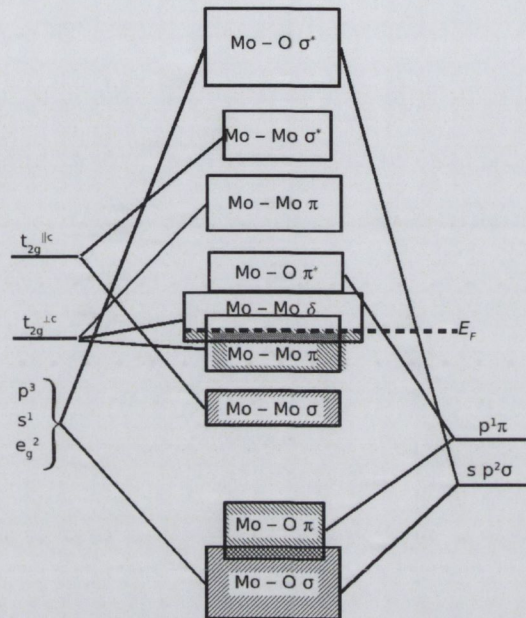


Fig. 5.5: A schematic of the energy level diagram of MoO_2 restricted to the interactions between the atomic Mo 4d and the O 2p orbitals.

The lowest energy bands result from Mo-O σ and Mo-O π bonds. The band resulting from the Mo-Mo σ bond of the $t_{2g||}$ bond is located along the MoO_2 a axis. Since the Mo in this oxide has a formal ionic configuration of $4d^2$, there are 4 electrons available per pair of Mo atoms. Two of these electrons occupy the lower-lying Mo-Mo σ band, leaving the remaining two electrons to enter the overlapping bands at E_F , making the compound a metallic conductor. The specific resistivity at room temperature has been reported to be $2 \times 10^{-6} \Omega \cdot \text{m}$ (13).

5.2.3 Calculated Electronic Density of States and Band Structure of MoO_2

For a deeper insight into the electronic properties of MoO_2 , we have calculated the electronic density of states (DOS) and the electronic band structure with VASP. For these calculations we used the relaxed struc-

ture as determined above. Since DFT calculations of the DOS can have many fine features, we used a smearing of 0.2eV. Furthermore, the band structure was calculated along the high symmetry lines within the first Brillouin zone of the simple monoclinic lattice (Fig. 5.6).

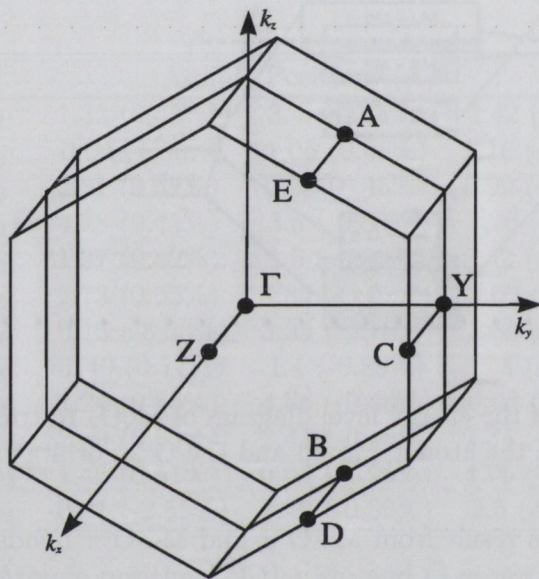


Fig. 5.6: Diagram of the first Brillouin zone of the simple monoclinic lattice with high symmetry lines shown.

A detailed description of the calculated electronic structure of MoO₂ is given by Eyert et al (7). The calculated total and partial DOS is presented in Fig. 5.7, along with the published data of Eyert for comparison (Fig. 5.8). From these figures, it can be seen that there is good agreement between the two. Furthermore, by using information on the electronic structure from the literature, we can identify some of the peaks and bands seen in the DOS plot.

UPS and XPS experiments revealed a group of bands approximately 9 eV in width. Within this group, there is a 6eV wide band associated with the O 2p states at higher energies, and a 3eV wide band for the Mo 4d states at E_F (12). This Mo 4d band is split into two peaks at 1.5eV

and 0.5 eV below the Fermi level (E_f) (12). From the plots in Figs. 5.7 and 5.8, we can see that there is in fact a 9eV wide set of bands below E_f . The partial density of states(PDOS) shows that the two peaks at 1.5 eV and 0.5 eV are dominated by Mo 4d electrons and the 6eV wide band below them is mostly filled by O 2p electrons, in agreement with the experimental data. This is also in agreement with the model proposed by Goodenough, in that this Mo 4d split at 1.5 eV and 0.5 eV can be explained by the Mo-Mo σ and π bonds respectively, and the wide band below is related to the O 2p bonds. Furthermore, the PDOS show that the Mo band is occupied at E_f , making MoO_2 a metallic conductor.

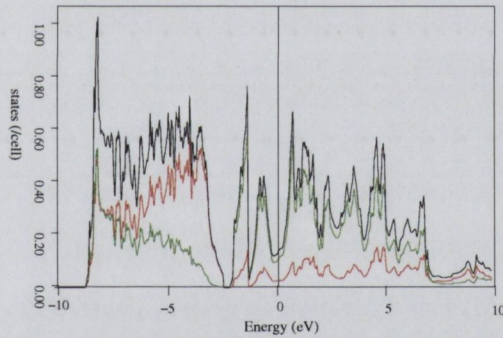


Fig. 5.7: The calculated total and partial DOS of MoO_2 . The black, red, and green lines represent the total, oxygen 2p and Mo 4d densities, respectively.

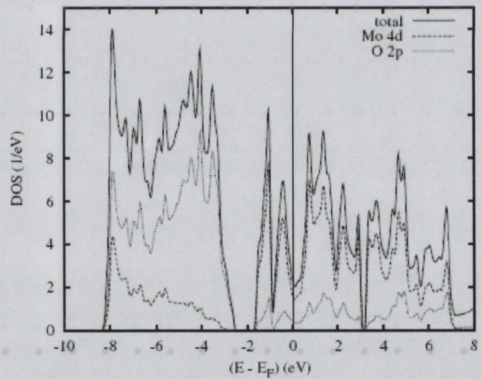


Fig. 5.8: The calculated total and partial DOS of MoO_2 from Eyert *et al* (7)

For completeness, the DFT calculated band structure is shown in Fig. 5.9 and with the band structure calculated by Eyert *et al* for comparison (Fig. 5.10). As seen, there is good agreement between the two except for a discrepancy along the C point. This may be due to the fact that we used a DFT relaxed structure for our calculations whereas they used the measured bulk values.

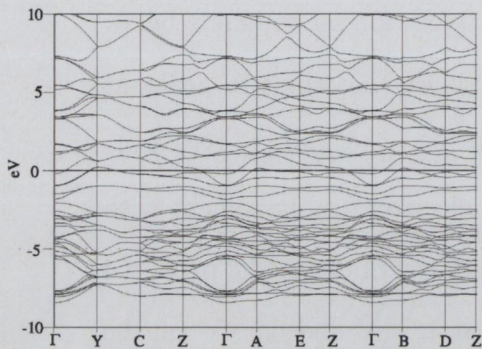


Fig. 5.9: The calculated band structure of MoO₂.

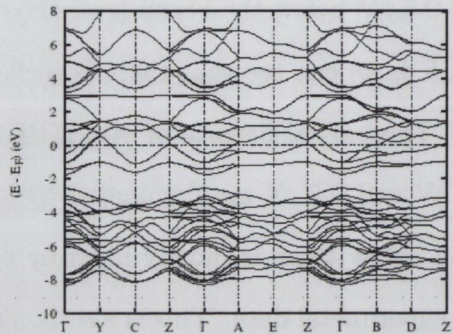


Fig. 5.10: The calculated band structure of MoO₂ from Eyert *et al* (14)

5.3 The Optical Properties of MoO₂

The optical measurements that give the most information on the electronic system are measurements of the reflectivity of light at normal incidence on single crystals. The reflectivity coefficient, $r(\omega)$, is a complex function defined at the crystal surface as the ratio of reflected electric field $E(refl)$ to the incident electric field $E(inc)$. Through the use of the Kramers-Kronig relations, these reflectivity measurements can then lead to the dielectric function, ϵ , of the material.

The reflectivity of MoO₂ was measured on single crystals some time ago by L. L. Chase (10). It is now possible to calculate optical spectra through the use of DFT with the PAW approach (15; 16). Therefore, we have calculated the optical spectra of MoO₂ and compared them to the published experimental results.

5.3.1 DFT Calculated Optical Spectra of MoO₂

After the electronic ground state has been determined, we can calculate the frequency dependent dielectric matrix using VASP. The imaginary

part is determined by a summation over empty states using the equation:

$$\varepsilon_{\alpha\beta}^1(\omega) = \frac{4(\pi e)^2}{\Omega} \lim_{q \rightarrow 0} \frac{1}{q^2} \sum_{c,v,\mathbf{k}} 2\omega \mathbf{k} \delta(\epsilon_{c\mathbf{k}} - \epsilon_{v\mathbf{k}} - \omega) x \langle u_{c\mathbf{k}+e_{\alpha q}} | u_{v\mathbf{k}} \rangle \langle c_{v\mathbf{k}+e_{\beta q}} | u_{v\mathbf{k}} \rangle^*, \quad (5.2)$$

where the indices c and v refer to conduction and valence band states, respectively; and $u_{c\mathbf{k}}$ is the cell periodic part of the wavefunctions at the \mathbf{k} -point, \mathbf{k} . The real part of the dielectric tensor ε^1 is obtained by the usual Kramers-Kronig transformation,

$$\varepsilon_{\alpha\beta}^1(\omega) = 1 + \frac{2}{\pi} P \int_0^\infty \frac{\varepsilon_{\alpha\beta}^2(\omega') \omega'}{\omega'^2 - \omega^2 + i\eta} d\omega', \quad (5.3)$$

where P denotes the principle value. The Kramers-Kronig transformation uses a small complex shift η , where we selected a value of 0.1 as suggested in the VASP manual. The method is explained in detail in Ref (16).

Using these calculated values, we now directly compare the DFT calculations of MoO₂ with experimental results published in the literature, as illustrated in Figs. 5.11 and 5.12, respectively.

Even though we have introduced a smearing of 0.1 eV, there are many extra peaks in the curves produced by DFT, that were not detected by the experimental measurements. Overall, the curves are very similar to each other, indicating that the DFT calculations of MoO₂ produce reliable results that can be interpreted as an accurate description of the experimental data.

Once the real and imaginary parts of the dielectric function are calculated, the following equation can be used to determine the frequency dependent reflectivity constants $R(\omega)$:

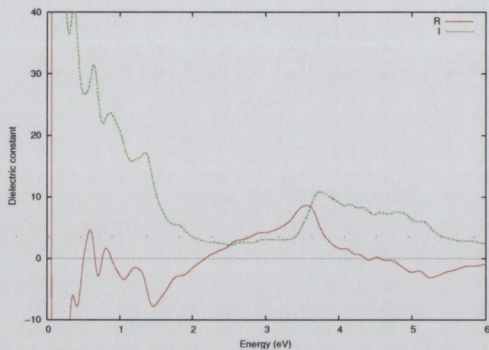


Fig. 5.11: The frequency dependent dielectric matrix of MoO₂ calculated using VASP.

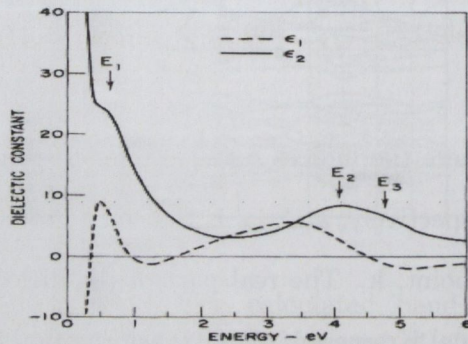


Fig. 5.12: The frequency dependent dielectric matrix of MoO₂ measured by optical reflectivity (10)

$$R(\omega) = \left| \frac{\sqrt{\varepsilon(\omega)} - 1}{\sqrt{\varepsilon(\omega)} + 1} \right|^2 \quad (5.4)$$

Figs. 5.13 and 5.14 show a comparison between the calculated and experimental frequency dependent reflectivity constant. These further illustrate the excellent agreement between the experimental data and our calculations.

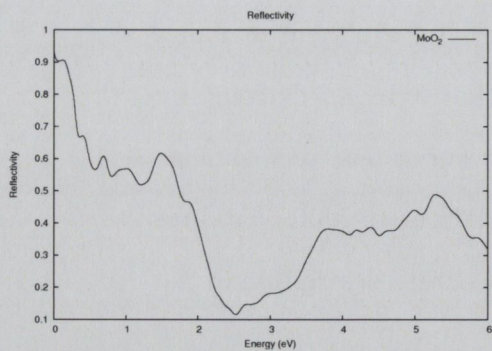


Fig. 5.13: Frequency dependent reflectivity constant calculated by DFT.

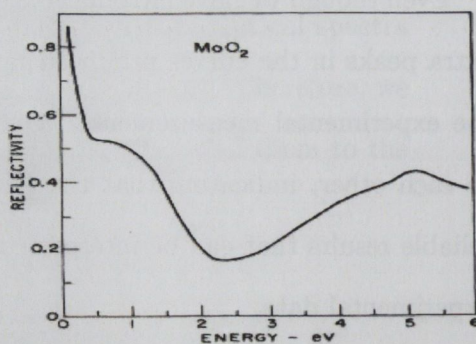


Fig. 5.14: Frequency dependent reflectivity constant on MoO₂ by optical measurements.

Bibliography

- [1] S. Murphy, *Surface Studies of the Fe/Mo(110) and Fe/W(100) Epitaxial Systems.*, PhD thesis, Trinity College Dublin, Ireland, 2000.
- [2] T. W. Haas and A. G. Jackson, *J. Chem. Phys.* **44**, 2921 (1966).
- [3] E. Bauer and H. Poppa, *Surf. Sci.* **127**, 243 (1983).
- [4] J. G. Che, C. T. Chan, W.-E. Jian, and T. C. Leung, *Phys. Rev. B* **57**, 1875 (1998).
- [5] Surface Preparation Laboratory, Penniweg 69 F, 1507 DE Zaandam, The Netherlands.
- [6] V. Bhosle, A. Tiwari, and J. Narayan, *J. Appl. Phys.* **97**, 083539 (2005).
- [7] V. Eyert, R. Horny, K.-H. Höck, and S. Horn, *J. Phys.: Condens. Matter* **12**, 4923 (2000).
- [8] A. Katrib, P. Leflaive, L. Hilaire, and G. Maire, *Catal. Lett.* **38**, 95 (1996).
- [9] B. Brandt and A. Stapski, *Acta. Chim. Slov.* **21**, 661 (1967).
- [10] M. A. K. L. Dissanayake and L. L. Chase, *Phys. Rev. B* **18**, 6872 (1978).
- [11] J. B. Goodenough, *Phys. Rev.* **117**, 1442 (1960).
- [12] F. Werfel and E. Minni, *J. Phys. C: Solid State Phys.* **16**, 6091 (1983).
- [13] D. Adler, *Solid State Physics*, volume 21, Academic Press, New York and London, 1968.
- [14] E. V., H. R., H. K-H., and H. S., *J. Phys.: Condens. Matter* **12** (2000).
- [15] B. Adolph, J. Furthmüller, and F. Bechstedt, *Phys. Rev. B* **63**, 125108 (2001).
- [16] M. Gajdoš, K. Hummer, G. Kresse, J. Furthmüller, and F. Bechstedt, *Phys. Rev. B* **73**, 045112 (2006).

Chapter 6

Surface Oxide Growth on Mo(110)

Thus far in the literature, the recent studies of the surface oxidation of the 4d series span from Ag to Rh. Within this span, there is a developing trend from a thermodynamically stable (O-M-O) surface oxide trilayer for Ag; to a slightly less stable trilayer for Pd; to a transient, kinetically stable trilayer for Rh. The recent theoretical and experimental studies on the initial oxidation stages of transition metals, Pd(111), Pd(100), Rh(111), Rh(110) and Rh(100) show that the structures of the surface oxides differ from those of the bulk oxides(1; 2; 3; 4; 5). The surface oxides on these metals exhibit different thermodynamic stabilities. A common feature is that their formation involves sub-surface penetration of oxygen, thus the metal atoms of the surface oxide are sandwiched between two atomic layers of oxygen, forming Oxygen-Metal-Oxygen (O-M-O) tri-layer surface oxides. However, it was recently suggested that since many of the TM oxides wet their own metal surfaces, the adhesion energy should provide extra stabilisation allowing a bulk-like surface ox-

oxide to form when the O_2 partial pressure is many orders of magnitude lower than required to maintain the bulk oxide (6).

In response to this we targeted the lighter metals of the 4d series to establish if a bulk-like surface oxide exists on the Molybdenum surface, and if so then what is the epitaxial relationship between the film and substrate. The details of these experiments will be outlined in this chapter.

6.1 Experimental Procedure

We used single crystal Mo(110) with the surface deviation from the (110) plane of less than 0.1° and cleaned with the procedure outlined in chapter 5. Once a clean surface was obtained the samples were annealed to 1000°C in an oxygen environment of 1×10^{-6} Torr for up to 1 minute. The surfaces were then characterized using LEED and STM. All STM images were recorded at room temperature in the constant current mode using currents of approximately 0.05 to 0.1 nA and bias voltages of 0.1 to 0.05 V with electrochemically etched W tips.

6.2 Experimental Results

6.2.1 LEED Analysis

Fig. 6.1 shows the LEED pattern of the molybdenum oxide overlayer on the Mo(110) surface after annealing at 1000°C and 1×10^{-6} Torr for 30 seconds, and then cooled in an O_2 environment at a rate of $\sim 200^\circ\text{C}/\text{min}$. The LEED pattern shows two rows of satellite spots that form an X shape centered about the molybdenum $p(1 \times 1)$ spots. The rows are separated

by an angle of 50° that is bisected by the Mo[1-1 0] direction. Using the Mo(110) p(1x1) LEED pattern of the substrate as our reference, we determined that the rows are running along the Mo[3-3 2] and Mo[3-3-2] direction. The pairing of these rows along two equivalent directions is an indication of the overlapping of patterns of two equivalent overlayer domains.

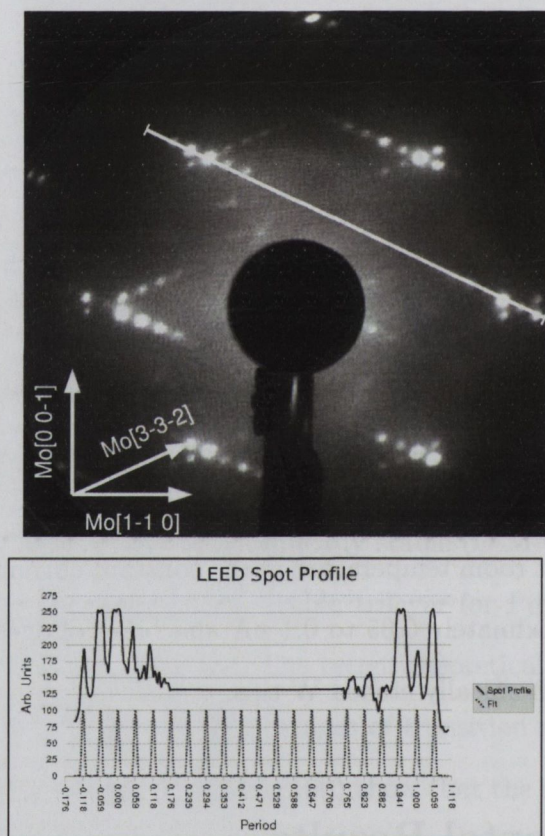


Fig. 6.1: The LEED pattern of the oxide overlayer on Mo(110) taken at 103eV. The sample was annealed for 30s at 1000°C and 1×10^{-6} Torr oxygen pressure. Below is a graph of a spot profile taken along the row of satellite spots indicated by the white line on the LEED image. The graph shows two curves. The curve above shows the LEED spot profile with the amplitude corresponding to the intensity of the LEED pattern. The curve below is a fit of the above profile showing the satellites have 1/17th the periodicity as the p(1x1) spots.

A spot profile along one of these rows is shown by the graph below

the LEED image in Fig. 6.1. This profile shows the satellite spots have a periodicity of $1/17$ of the spacing between two primary Mo(110) LEED spots. From the direction and period of the rows, it was determined that the satellite spots correspond to an overlayer with dimensions in the real space of 5.2 \AA along the $[1-1-3]$ direction (orthogonal to $[3-3-2]$). This 5.2 \AA separation is equal to one spacing of Mo lattice in that direction. Furthermore, we can say that this 1:1 coincidence occurs once for every 17 units in the Mo $[0\ 0-1]$ direction. This corresponds to a separation of $\sim 23 \text{ \AA}$ between two rows of coincidence. The same applies to the equivalent $[1-1\ 3]$ direction of Mo lattice. We can therefore conclude that there is 1:1 coincidence between the overlayer and the Mo substrate in these two directions. For that reason we will assign the domains to be lying along the $[1-1-3]$ and $[1-1\ 3]$ directions, and for simplicity the description will be kept to the Mo $[1-1-3]$ domain. The matrix describing the coincidence unit cell is then:

$$\begin{bmatrix} 17 & -17 \\ 2 & 1 \end{bmatrix}$$

As an aid, the real and reciprocal space diagrams of this system are illustrated in Fig. 6.2. In this figure, the real and reciprocal space Mo(110) unit vectors are labeled a_1 and a_2 , and a_1^* and a_2^* , respectively. The real and reciprocal space unit vectors of the overlayer are labeled b_1 and b_2 , and b_1^* and b_2^* respectively.

6.2.2 STM Analysis

Fig. 6.3 presents an STM image of the surface of Mo(110) after annealing under the same conditions discussed above. This image shows a periodic row structure aligned along the Mo $[1-1-3]$ direction. This row structure,

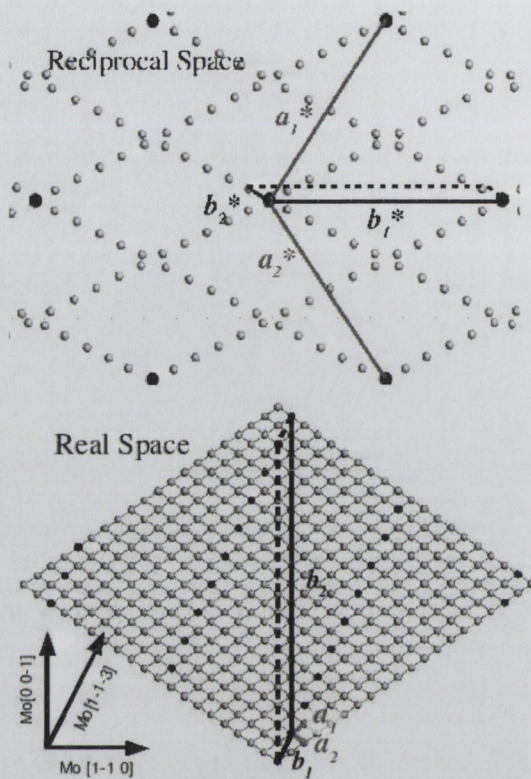


Fig. 6.2: Unit vectors along Mo[1-1-1] and Mo[1-1 1] in the real and reciprocal space are labelled a_1 and a_2 , and a_1^* and a_2^* , respectively. The overlayer real and reciprocal space unit vectors are labelled b_1 and b_2 , and b_1^* and b_2^* , respectively. The black dotted line along the b_1 direction represents the 1:1 coincidence of the overlayer and substrate in the Mo[1-1-3] direction.

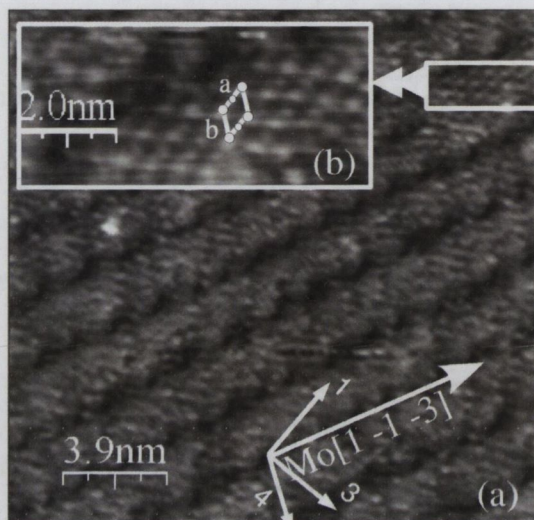
has a period of $23 \pm 1 \text{ \AA}$ and corrugation of $0.2 \pm 0.1 \text{ \AA}$. These rows are highly regular and seemingly cover the entire substrate surface. The periodicity and direction of these rows is consistent with the spacing of the satellite spots in the LEED pattern shown in Fig. 6.1. The image (b) in Fig. 6.3 was taken at a bias of 0.05 V and is a zoom of the area in the top right of Fig. 6.3(a). It shows that the atomic surface structure has a quasi-hexagonal surface mesh with a lattice constant of $5.7 \pm 0.2 \text{ \AA}$ and an angle of $\sim 124^\circ$. This mesh is highlighted by the white diamond, and the atomic structure which is highlighted by the white dots on this

diamond. These dots have a periodicity of $2.9 \pm 0.1 \text{ \AA}$ along the side marked a, forming rows in a direction that is near to Mo [0 0-1]. There is a modulation in the intensity, or height, of the atoms along the rows as shown in the line profile below the image in Fig. 6.3. Furthermore, these rows are separated by $5.7 \pm 0.2 \text{ \AA}$ in a direction near to Mo[1-1 1], marked side b of the diamond. It should be noted that this surface structure is the same over the the entire surface however most areas needed to be enhanced with FFT filtering before it becomes obvious.

Given that the periodicity and direction of these rows is the same as the coincident lattice structure seen with LEED, we consider that the rows represent the coincidence molybdenum oxide structure. It has been shown in previous studies of coincident lattice structures using electron-scattering quantum-chemistry (ESQC) that the atomic contrast of an STM image of an ultrathin oxide layer on a metal substrate is dependent on the site location of the oxygen atom on the substrate (7). This was explained by an interplay of several electronic effects causing a difference in the tunneling probability at that location. This theory has been used to explain the Moire patterns that are often seen by STM with coincidence lattice structures (8; 9; 7; 10; 11; 12), and can explain the striped pattern shown in Fig. 6.2. With this in mind and from what we know from the LEED and STM data a model for this system was developed.

6.2.3 MoO₂ Surface Oxide Model

Based on previous Raman, XPS and RHEED studies of the oxidation of molybdenum it was determined that MoO₂ is the sole oxide that grows epitaxially on the Mo(110) surface at low pressures (13; 14; 15; 16; 17; 18; 19; 20). The MoO₂ bulk structure has a monoclinic-distorted ru-



Directions indicated by arrows:

1) Mo[0 0-1] 3) Mo[1-1 0] 4) Mo[1-1 1]

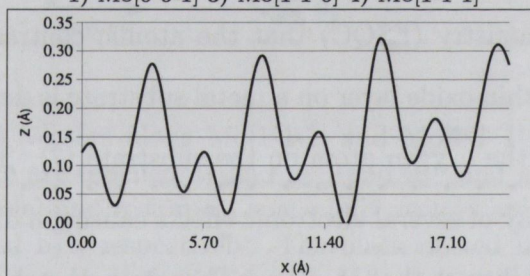


Fig. 6.3: (a) STM image taken at a bias of 0.10 V and current of 0.1nA of the MoO₂/Mo(110) surface after annealing for 30 s at 1000° C and 1x10⁻⁶ Torr oxygen pressure. The image shows a periodic row structure aligned along the Mo[1-1-3] direction with a period of 23 ± 1 Å. (b) Is a zoom of the area indicated by the box in the top right of the figure, taken at bias of 0.05V and current of 0.1nA. A white diamond with white dots highlights the atomic surface structure. These dots have a periodicity of 2.9±0.1 Å along the side marked a, forming atomic rows in the ~ Mo[0 0 -1] direction. There is a modulation in the intensity, or height, of the atoms along the rows. This modulation is shown by a line profile taken along a row, and is illustrated in the graph below the image. Furthermore, these rows are separated by 5.7 ± 0.2 Å in a direction near to Mo[1-1 1] marked side b of the diamond.

tile structure (space group P21/C) with lattice parameters $a=5.661$ Å, $b=4.846$ Å, $c=5.628$ Å, and $\beta = 120.95^\circ$ (21). This gives the a and c axes and the angle β dimensions similar to the overlayer imaged by STM. Also, the axes are nearly twice that of the Mo bulk lattice constant with β close to the angle of the quasi-hexagonal Mo(110) surface. Because of this, there are multiple epitaxial relationships that are suitable matches for the LEED data. However, considering the size and shape of the surface mesh imaged by STM, the only compelling overlayer structure is MoO₂(010)/Mo(110). The MoO₂(010) surface is a quasi-hexagonal surface with a lattice spacing on the order of 5.7 Å and an angle of 120.95°, and very similar to the surface imaged STM. Furthermore, the MoO₂(010) surface (Fig. 6.3) is built from alternating ionic planes of oxygen anions, and Mo-Mo bonded dimers (Fig. 6.4). A layered oxygen-metal-oxygen (O-M-O) surface like this is a likely choice for two reasons. First, metal/polar-oxide interfaces such as this, where the oxide has only oxygen ions within the terminating plane are generally considered most stable, with adhesive energies an order of magnitude higher than non-polar interfaces (1; 2; 6; 22; 23; 24; 25; 26; 27; 28; 4; 9; 29; 30). This stability is believed to arise from several factors including the macroscopic Coulomb interaction between the ions in the oxide and the 'image charges' in the metal (29; 30). On the atomic scale this interaction is better described by a charge redistribution across the interface (31; 32). In addition to this, several studies of the surface oxides of TMs have shown through a combination of LEED and DFT that an O-M-O trilayer can be the most energetically favoured (1; 2; 3; 4; 5).

Using the literature as our inspiration we started with a MoO₂ O-M-O trilayer, and considered the interface as being built from the Mo(110)

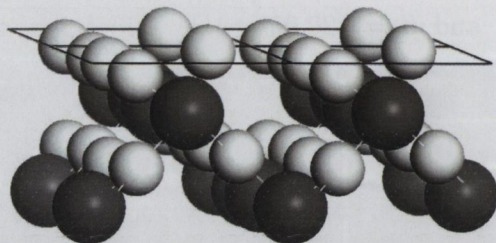


Fig. 6.4: The MoO_2 (010) surface is built from alternating layers of oxygen anions (white) and Mo-Mo bonded cations (grey). In the oxygen layers, the oxygen is arranged in quasi-hexagonal pattern with an atomic spacing of $\sim 3\text{\AA}$. In the Mo layers, the metal forms dimers that are aligned along the MoO_2 [100] direction, and are arranged in quasi-hexagonal pattern with dimensions of the MoO_2 unit cell.

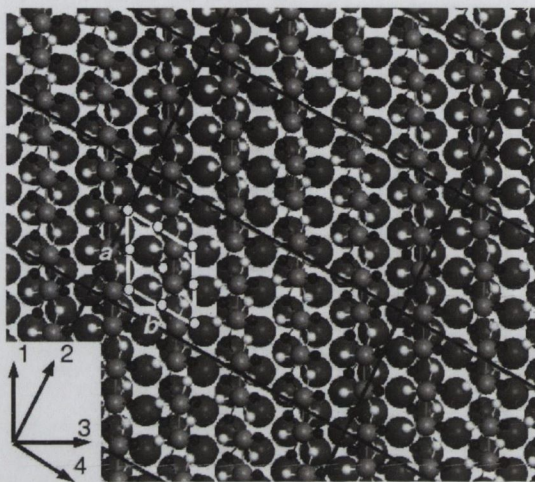
surface plane followed by the $\text{MoO}_2(010)$ oxygen plane. We started by orientating the $\text{MoO}_2(010)$ oxygen plane to find a suitable match with the $\text{Mo}(110)$ surface mesh that formed 1:1 coincidence about the $\text{Mo}[1-1-3]$ direction. Since the $\text{Mo}(110)$ surface mesh and the $\text{MoO}_2(010)$ oxygen mesh are both quasi-hexagonal with similar lattice parameters, there are three suitable orientations that form such coincidence; MoO_2 either [201] or [-101] or [102] are parallel to $\text{Mo}[1-1-3]$. The next step was to compare these three models to the LEED and STM in order to narrow the selection. Upon fitting the three possible orientations into a unit cell constrained by the dimensions determined by LEED the possible orientations were narrowed to one, the $\text{MoO}_2[201] \parallel \text{Mo}[1-1-3]$ orientation. This selection was done by considering two things. First we only chose those orientations with a minimal amount of stress induced on the film to fit the unit cell, and more importantly this was the only orientation with an equivalent domain along $\text{Mo}[1-1-3]$ direction. With this orientation the MoO_2 c axis is orientated 4.9° off the $\text{Mo}[0-0-1]$ direction, and the a

axis near to the Mo[1-1 1]. There is an equivalent domain of MoO₂(0-1 0) [2 0 1] || Mo[1-1 3] with the *c* axis orientated the same degree off Mo[0 0-1] but in the opposite direction, and the *a* axis near the equivalent Mo[1-1-1] direction.

The next step was to optimize this model to completely agree with the LEED and STM data. In order to induce the required 1:1 coincidence Mo [1-1-3] that reoccurs once every 17 units along Mo[0 0-1] the overlayer was skewed by 2.7°. After the skewing the MoO₂ [100] is now 2° off the Mo[0 0-1], and the overlayer can be described by a unit cell of MoO₂ [201] parallel to Mo[1-1-3] and MoO₂ [0 0 4] parallel to half a unit of Mo[9-9 7]. The dimensions of such a unit cell are 10.4 Å x 22.9 Å with an angle of 86.4°. Furthermore, the matrix describing the overlayer unit cell can be reduced to cell dimensions of the smallest length scale describing the overlayer as:

$$\begin{bmatrix} 1 & 8 \\ -4 & 2 \end{bmatrix}$$

The illustration in Fig. 6.5 shows the MoO₂(010)/Mo(110) surface model as described above. The black mesh shows the overlayer unit cell in agreement with the LEED data. There is a 1:1 coincidence between the interfacial oxygen and molybdenum atoms that runs along the Mo[1-1-3] direction (along the black mesh lines in that direction). The white diamond highlights the surface oxygen unit cell, and the surface oxygen are highlighted in that cell by the white dots. The surface oxygen unit cell is in perfect agreement with the STM data except there is an added row of oxygen running along the *a* axis (side marked *a* in Fig. 6.3) .



Directions indicated by arrows:

- 1) Mo[0 0-1] 2) Mo[1-1-3] 3) Mo[1-1 0] 4) Mo[1-1 1]

Fig. 6.5: Top view of the $\text{MoO}_2(010)$ overlayer unit cell as determined by STM, LEED and DFT calculations. The larger dark grey spheres represent the Mo(110) surface atoms, the white spheres represent the O^{2-} interface atoms, the grey spheres represent the Mo^{4+} atoms, and the black spheres represent the O^{2-} surface atoms. The black rectangular grid represents the overlayer unit cell. Note that this is the “on-top” configuration and that the interface oxygen atoms are located on top of the Mo interface atoms at the intersections of the grid lines and along the Mo [1-1-3] direction.

6.3 DFT Calculations

To further refine this model, DFT calculations were carried out. As a first approximation, the MoO_2 unit cell was given a slight distortion and rotation to align the a and c axes along Mo [1-1-1] and [0 0-1], respectively (Fig. 6.6). To fit the oxide to the substrate, the oxide unit cell was skewed by 4° to give an angle of 125° , the a axis was reduced by 3 %, and the c was stretched by 10 %. In doing this we were able to fit one primitive unit cell of the $\text{MoO}_2(010)$ surface to the Mo(110) surface, greatly reducing our computing cost. This modification also allows us to compare the 4 possible interfacial oxygen coordination sites at the interface in terms of

energy, work of adhesion, and interlayer separation. For the calculations, we used a periodic slab geometry with a four layer slab of Mo(110), an O-Mo-O trilayer of MoO₂(010), and a vacuum gap of 15 Å between the slabs to eliminate any spurious electric fields (25). In these calculations the bottom two layers of the Mo slab were constrained and the top two Mo layers along with MoO₂ were allowed to relax. These calculations were performed using CASTEP (33), and for comparison both the Generalized Gradient Approximation (GGA) and the Local Density Approximation (LDA) with a cutoff of 300 eV and a k point separation of 0.05 1/Å in the Brillouin zone were used. We calculated the work of adhesion as the difference of the sum of the individual energies of the relaxed Mo(110) and MoO₂(010) slabs and the energy of the two interfaced together, all divided by the area of the interface.

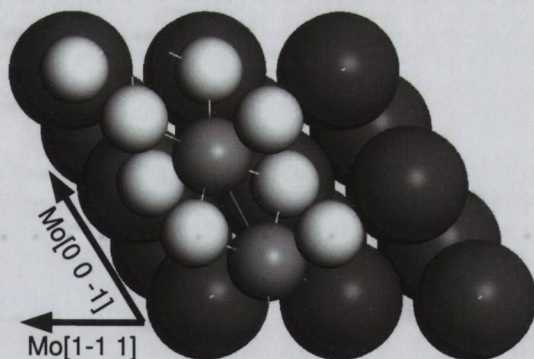


Fig. 6.6: Model unit cell used for DFT calculations with MoO₂(010) plane parallel to the Mo(110) surface and MoO₂(010) and the *a* and *c* axes aligned along the Mo[1-1-1] and [0 0-1], respectively.

6.3.1 DFT Geometry Optimization

DFT geometry optimizations were performed for the slabs of dimensions shown in Fig. 6.6 for each of the four possible configurations of the

interfacial oxygen. These configurations are (a) on the 2-fold bridge site above the underlying Mo atom, (b) atop the surface Mo, (c) on the 3-fold hollow site, and (d) 2-fold bridge site with no underlying Mo atom (Fig. 6.7).

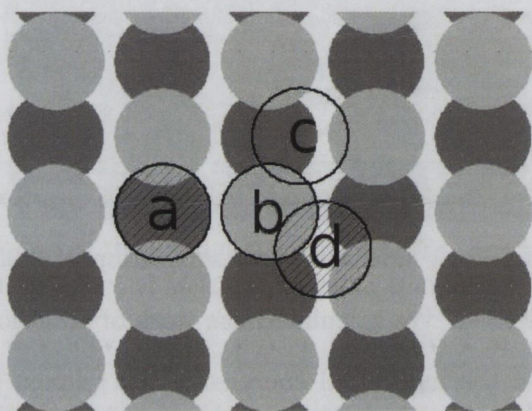


Fig. 6.7: DFT geometry optimizations were performed for each of the four possible configurations of the interfacial oxygen atoms that form the coincident sites seen in the LEED data. These configurations are (a) on the 2-fold bridge site above the underlying Mo atom, (b) atop the surface Mo, (c) on the 3-fold hollow site, and (d) 2-fold bridge site no underlying Mo atom (Fig. 6.7).

It was found that both of the bridge configurations, (a) and (d), relaxed onto the 3-fold site, leaving us with only two stable configurations. In both cases there was a strong adhesion between the film and substrate, as expected for a polar oxide/metal interface. The adhesion energy from this system has two main components, a contribution from the metal-oxygen bonding, and a contribution arising from the electron redistribution at the interface. The latter is the result of the metal substrate transferring electrons to the interfacial oxygen atoms, which can be explained by the Pauling's electronegativity of the two elements, $\chi_{Mo}(1.8) < \chi_O(3.5)$. This results in a polarization of the metal at the interface, and a stronger adhesion energy. This effect was found to increase the

adhesion energy by an order of magnitude for the polar Mo/MgO(111) interface compared to the nonpolar Mo/MgO(100) interface (34). A map of the electron density difference gives an illustration of the electron redistribution at the interface for the two configurations (Fig. 6.8). On this map the light areas above the interface oxygen indicate an enhanced electron population, whereas the dark areas and bands above the Mo atoms and along the interface indicate a reduced electron population, thus mimicking the macroscopic ‘image charge’. Furthermore, with these two configurations, it was found that the case with the interface oxygen located on the 3-fold site had the lowest energy by 0.20 and 0.23 eV per atom at the interface as calculated by GGA and LDA, respectively. This configuration also had the shortest interlayer separation and highest work of adhesion, indicating a stronger interface bonding; the results of these calculations are shown in table 6.1.

Configuration	ΔE		W		Interlayer separation (\AA) GGA
	GGA	LDA	GGA	LDA	
Top site	0.2	0.23	5.75	6.48	1.72
3-fold			7.13	8.10	1.18

Table 6.1: DFT Geometry Calculations

ΔE is the difference in total energy for the system in eV/Atom
W is the work of adhesion in J/m^2

From these results, full overlayer unit cell slabs for both the on top and 3-fold configurations were constructed. These slabs consisted of two layers of Mo(110) and the MoO₂(010) tri-layer giving 148 atoms in total. The interlayer distance at the interface was fixed across the slab to the value calculated for the respective configurations; i.e. interlayer warping was not considered for the different configurations across the interface(28). The unit cell slab used for the on-top configuration is

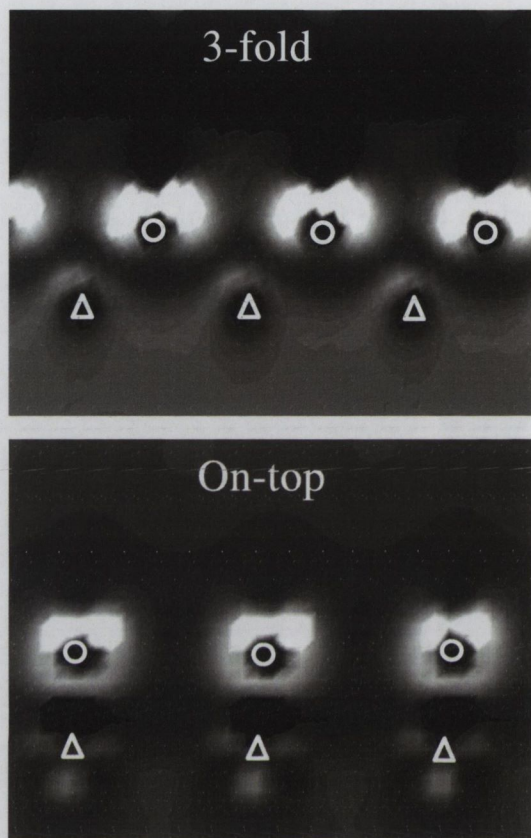


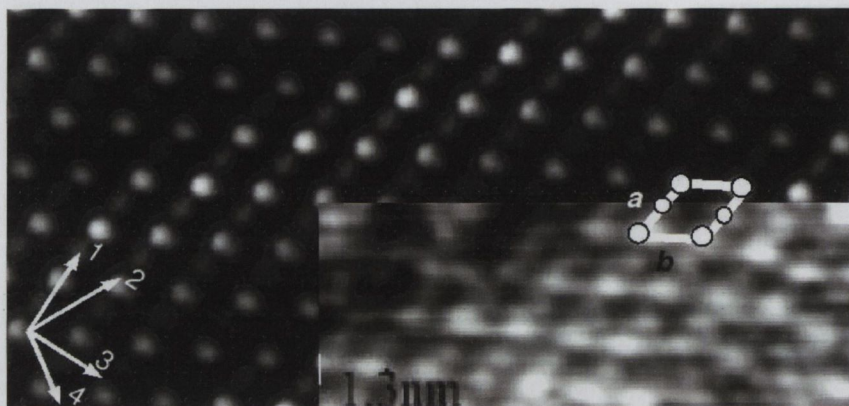
Fig. 6.8: A slice taken along the Mo(1-1 0) surface showing a map of the electron density difference for the 3-fold and on-top configuration. The circles mark the interfacial oxygen and the triangles mark the substrate Mo locations. Light areas represent positive and dark areas represent negative areas corresponding to enhanced and reduced electronic populations respectively. This map was generated using the results of the GGA calculations.

shown in Fig. 6.5. DFT calculations using the LDA and an energy cut off of 300 eV were performed for the two cases. It was found that the 3-fold case converged with an energy of 0.1eV/atom lower than the on-top case, suggesting that this is the most stable surface.

6.3.2 DFT STM Simulations

STM simulations of the two DFT calculations using a tip to sample bias of 0.05 V were also performed. The case of the 3-fold site configuration showed an obvious row of structures formed by the STM contrast, in agreement with the rows seen in the STM data. However, the on-top site configuration showed very little change in contrast. An STM simulation for the 3-fold case is compared with an atomically resolved STM image of the $\text{MoO}_2(010)/\text{Mo}(110)$ surface. The comparison shows that this model is now in excellent agreement with the STM data in Fig. 6.9. Again, to highlight the surface oxygen unit cell a white diamond is drawn, with the surface oxygen in the cell represented by white dots. The oxygen lattice in this simulation features a missing row of oxygen along the $\text{MoO}_2[1\ 0\ 0]$, as in the STM data. Furthermore, there is also an alternation of the bright and dim spots that represent the oxygen atoms along the rows in agreement with the experimental data.

Further investigation of the STM simulation of the 3-fold case reveals the origin of both the bright and dim STM spots of the surface oxygen atoms along the MoO_2 a axis, along with the origin of the missing oxygen row seen in the STM data. Fig. 6.10 shows the map of STM simulation from Fig. 6.9 overlaid on the model of the $\text{MoO}_2(010)$ surface. This figure shows that the dim spots on the STM images are a probe of the empty states near the Fermi level in the molecular orbital of the O^{2+} surface atoms that bridge the two Mo atoms forming Mo-Mo dimers, marked (a). Whereas the bright spots, (b), are representative of the states in the molecular orbital of the O^{2+} surface atoms that bridge between two Mo atoms of separate Mo dimers. This indicates that the density of states accessible by the STM tip is more localized around



Directions indicated by arrows: 1) Mo[0 0-1] 2) Mo[1-1-3] 3) Mo[1-1 0] 4) Mo[1-1 1]

Fig. 6.9: The high resolution STM image taken at 0.05 V and 0.1 nA in constant current mode (lower right) compared with a DFT STM simulation at 0.05 V. The $\text{MoO}_2(010)$ atomic surface structure has a quasi-hexagonal surface mesh with a lattice constant of $5.7 \pm 0.2 \text{ \AA}$ and an angle of $\sim 124^\circ$. This mesh is highlighted by the white diamond, and the atomic structure is highlighted by the white dots on this diamond. These dots have a periodicity of $2.9 \pm 0.1 \text{ \AA}$ along the side marked *a* (*a* axis), forming rows in a direction that is near to Mo [0 0-1]. There is a modulation in the intensity, or height, of the atoms along the rows. Furthermore, these rows are separated by $5.7 \pm 0.2 \text{ \AA}$ in a direction near to Mo[1-1 1], marked side *b* of the diamond (*c* axis). The brightest spots are located above areas where the oxygen atoms at the interface are located on the 3-fold hollow sites.

these areas marked (b), and can be related to bulk MoO_2 where the atomic sphere radii for the oxygen located in this position was calculated to be $\sim 10\%$ larger versus the oxygen bonded to the Mo dimers (35). Furthermore, the oxygen atoms of type marked (c) in the figure have a single bond to the Mo and are not imaged by STM.

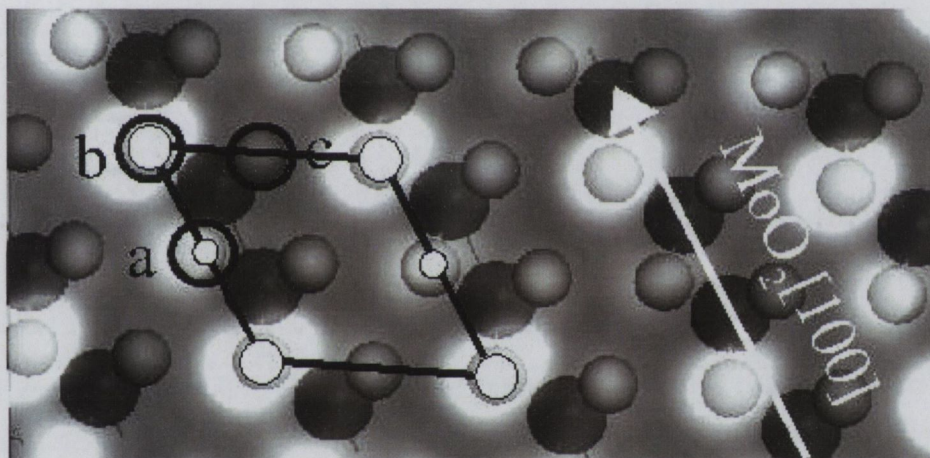


Fig. 6.10: Overlay of an STM simulation at 0.05V for the 3-fold case. The MoO₂ unit cell is drawn by the black diamond, and the surface oxygen are white, and first layer of Molybdenum atoms are grey. The circle marked (a) shows the dim oxygen atoms seen in STM, circle (b) shows the bright oxygen atoms, and circle (c) shows the missing oxygen atoms.

Bibliography

- [1] J. Gustafson et al., *Phys. Rev. Lett.* **92**, 126102 (2004).
- [2] J. Gustafson et al., *Phys. Rev. B* **71**, 115442 (2005).
- [3] E. Lundgren et al., *Phys. Rev. Lett.* **88**, 246103 (2002).
- [4] K. Reuter and M. Scheffler, *Appl. Phys. A* **78**, 793 (2004).
- [5] C. Dri et al., *J. Chem. Phys.* **125**, 094701 (2006).
- [6] C. T. Campbell, *Phys. Rev. Lett.* **96**, 066106 (2006).
- [7] Y. J. Kim et al., *Phys. Rev. B* **55**, R13448 (1997).
- [8] C. I. Carlisle, D. A. King, M.-L. Bocquet, J. Cerdá, and P. Sautet, *Phys. Rev. Lett.* **84**, 3899 (2000).
- [9] H. C. Galloway, P. Sautet, and M. Salmeron, *Phys. Rev. B* **54**, R11145 (1996).
- [10] T. Maroutian, S. Degen, C. Becker, K. Wandelt, and R. Berndt, *Phys. Rev. B* **68**, 155414 (2003).
- [11] M. Ritter, W. Ranke, and W. Weiss, *Phys. Rev. B* **57**, 7240 (1998).
- [12] S. Degen et al., *Surf. Sci.* **576**, L57 (2005).
- [13] T. Jirsak, M. Kuhn, and J. A. Rodriguez, *Surf. Sci.* **457**, 254 (2000).
- [14] G. H. S. Jr. and P. C. Stair, *Surf. Sci.* **317**, 65 (1994).
- [15] E. Bauer and H. Poppa, *Surf. Sci.* **127**, 243 (1983).
- [16] T. W. Haas and A. G. Jackson, *J. Chem. Phys.* **44**, 2921 (1966).
- [17] M. Kamei, T. Obayashi, H. Tsunematsu, Y. Tanaka, and Y. Gotoh, *Surf. Sci.* **356**, 137 (1996).
- [18] Y. Gotoh and E. Yanokura, *Surf. Sci.* **287-288**, 979 (1993).
- [19] A. K. Santra, B. Min, and D. W. K. Goodman, *Surf. Sci.* **513**, L441 (2002).
- [20] T. Schroeder, J. Zegenhagen, N. Magg, B. Immaraporn, and H. Freund, *Surf. Sci.* **552**, 85 (2004).
- [21] B. Brandt and A. Stapski, *Acta. Chim. Slov.* **21**, 661 (1967).
- [22] M. Todorova et al., *Phys. Rev. Lett.* **89**, 096103 (2002).
- [23] A. Stierle et al., *Science* **303**, 1652 (2004).

- [24] D. J. Siegel, L. G. Hector, and J. B. Adams, *Phys. Rev. B* **65**, 085415 (2002).
- [25] R. Benedek, M. Minkoff, and L. H. Yang, *Phys. Rev. B* **54**, 7697 (1996).
- [26] M. W. Finnis, *J. Phys.: Condens. Matter* **8**, 5811 (1996).
- [27] J. Purton, S. C. Parker, and D. W. Bullett, *J. Phys.: Condens. Matter* **9**, 5709 (1997).
- [28] R. Benedek et al., *Phys. Rev. Lett.* **84**, 3362 (2000).
- [29] M. W. Finnis, *Acta Metall. Mater.* **40**, S25 (1992).
- [30] D. M. Duffy, J. H. Harding, and A. M. Stoneham, *Acta Metall. Mater.* **40**, S11 (1992).
- [31] C. Noguera, F. Finocchi, and J. Goniakowski, *J. Phys.: Condens. Matter* **16**, S2509 (2004).
- [32] K. Reuter, *Nanocatalysis: Principles, Methods, Case Studies*, Springer, 2005.
- [33] M. D. Segall et al., *J. Phys.: Condens. Matter* **14**, 2717 (2002).
- [34] J. Goniakowski and C. Noguera, *Phys. Rev. B* **66**, 085417 (2002).
- [35] V. Eyert, R. Horny, K.-H. Höck, and S. Horn, *J. Phys.: Condens. Matter* **12**, 4923 (2000).

Chapter 7

Formation of MoO₂ Nanowires on Mo(110)

In this chapter, a method of growing single crystal MoO₂ nanowires on the Mo(110) surface is described. We show that an oxide film can undergo a periodic self-faceting regime during growth, producing regular arrays of oxide nanowires. In Chapter 6, we showed that in the first stage of oxide growth, a highly strained closed MoO₂ (010) oxide layer is formed on the Mo(110) surface. However, if in the bulk, this (010) oxide surface can be classified as a polar, Tasker type III surface, which needs a surface modification to be energetically favourable (1). In the case of the MoO₂ (010) surface oxide, as with any metal polar oxide interface, the film surface is close enough to the interface such that a charge redistribution at the interface can sufficiently modify the surface charge density and stabilize the film (2; 3; 4; 5; 6; 7; 8; 9; 10; 11; 12; 13; 14; 15). However, a key difference of this system is that the O-M-O oxide layer is not a transient surface oxide, phase like with the other studies, but it is that of the bulk oxide, MoO₂(0 1 0). Therefore, with further oxidation, the

oxide phase would continue to grow. For this chapter, we will use the $\text{MoO}_2(0\ 1\ 0)$ surface oxide as our starting point and show that with continued oxidation, the oxide film develops into regular arrays of MoO_2 nanowires.

The general mechanism for the growth mode is based on a mechanism for the formation of quantum dots on the surface of thin solid films recently proposed by A. A. Golovin et. al. (16). This method is a bottom-up approach in which the film goes through two stages of growth. In the initial growth stage, the film is coupled to the substrate via a strong wetting interaction. Furthermore, the substrate orientation causes the film to grow in a crystallographic orientation which, due to a large surface energy anisotropy, would be thermodynamically forbidden in the bulk and prone to faceting. However, due to the adhesion energy associated with the wetting interaction, faceting is suppressed. Stage two occurs upon further film growth with which the short ranged stabilizing effects of the wetting interaction can no longer stabilize the film surface. This, coupled with a surface energy anisotropy in the film, can result in periodic faceting of the film surface (16), leading to the formation of regular arrays of nanostructures.

7.1 Experimental Procedure

In this chapter we used the same sample and cleaning procedure as outlined in Chapter 6. Once a clean surface was obtained, the samples were annealed in oxygen by using the following procedure. First the UHV chamber was back-filled with oxygen to a pressure of 1×10^{-6} Torr. The sample temperature was then ramped from room temperature to $1200 \pm$

50 °C (beyond the decomposition temperature of molybdenum oxides,) at a rate of approximately 300 °C per min and then down to 900 ± 50 °C. The sample was held at 900 ± 50 °C for the desired annealing time and then cooled in an oxygen environment at a ramp rate of approximately 100 °C per minute. After the samples were cooled to room temperature, the surfaces were characterised using LEED, AES and STM. All STM images were recorded at room temperature in the constant current mode using currents of approximately 0.05 to 0.1 nA and bias voltages of 0.1 to 0.05 V with electrochemically etched W tips. The STM used in these studies was calibrated for atomic scale measurements. However, due to the relatively large size of these features, along with a lack of a nanometer scale calibration standard, we have introduced a larger degree of error in these measurements.

7.2 Experimental Results

In order to characterise the oxidation of Mo(110) under these conditions, the sample was annealed with a series of anneals from 5 min to 90 min. After each anneal, the sample was analyzed with LEED and STM and then flashed clean before starting another anneal.

The series of LEED and STM images in Fig. 7.1 show the evolution of molybdenum oxide over a range of annealing times from 5 minutes, Fig. 7.1A, to up to one hour, Fig. 7.1E. The resulting oxide has the form of nanowires. These wires grow in the Mo(110) [001] direction and have dimensions ranging from 5 nm wide by 0.5 nm tall up to a maximum size of 30 nm wide by 6 nm tall. These are shown by the line profiles in Fig. 7.1. Remarkably, the direction of the wire-like structures is different

from the direction of the stripes observed at an earlier stage (see Fig. 6.3 in Chapter 6). This indicates that the initial surface strain caused by coincidence structure of the surface oxide is no longer a source of surface arrangement. What is most interesting is that the dimensions of these wires are solely dependent on the annealing time, allowing the size of the wires to be easily manipulated. However, with further annealing beyond one hour, wires larger than 30 nm wide could not be achieved.

7.2.1 STM Analysis

Attempts were made to view the atomic structure of these wires with STM, however such resolution could not be achieved. There is however, further information about the structure of these wires in the STM measurements. Fig. 7.2 shows a high-resolution STM image of a side of one of the large nanowires. In this image, terraces can be seen. According to the line profile in this figure, one can see that the largest nanowires are comprised of terraces that have a width of 0.95 ± 0.09 nm and a step height of 0.53 ± 0.05 nm (Fig. 7.2). These dimensions give a slope of ~ 30 degrees to the substrate surface normal, resulting in a periodically faceted "hill and valley" MoO₂ surface.

7.2.2 Auger Data

The Auger spectra of the largest wires indicates that the oxide has the stoichiometry of MoO₂ (Fig. 7.3). The ratio of the Mo peak to the oxygen peak at 510 eV is 1:2. The percent concentration is listed in Table 7.1.

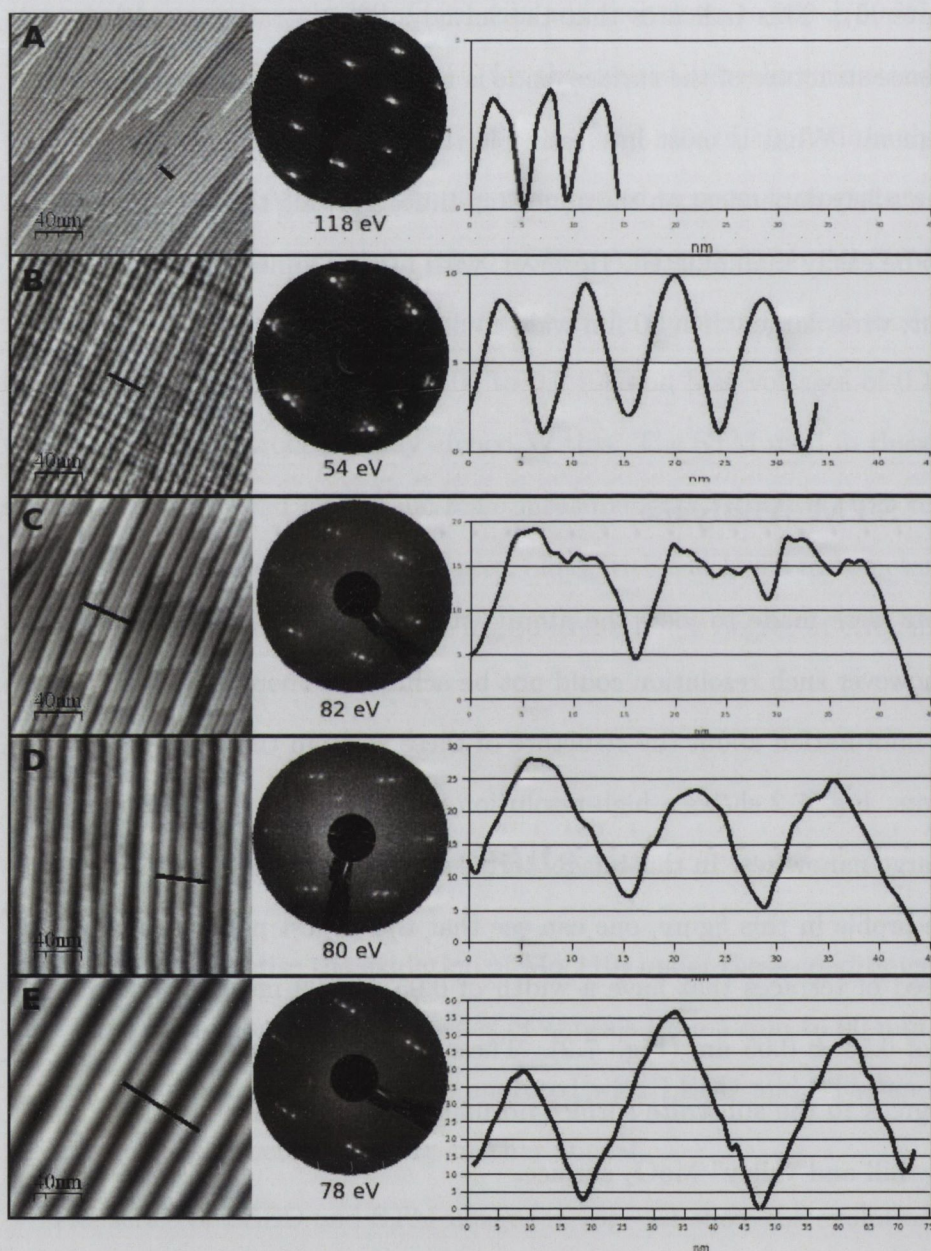


Fig. 7.1: The figure contains LEED, and STM as well as line profiles of the Mo(110) surface after annealing in an oxygen environment. The STM images show the development of MoO₂ nanowires over time. The width and height of the structures have the following dimensions, respectively: A. 5.20 nm x 0.33 nm, B. 8.46 nm x 1.00 nm, C. 14.42 nm x 1.4 nm, D. 15.32 nm x 2.5 nm, E. 27.50 nm x 5 nm.

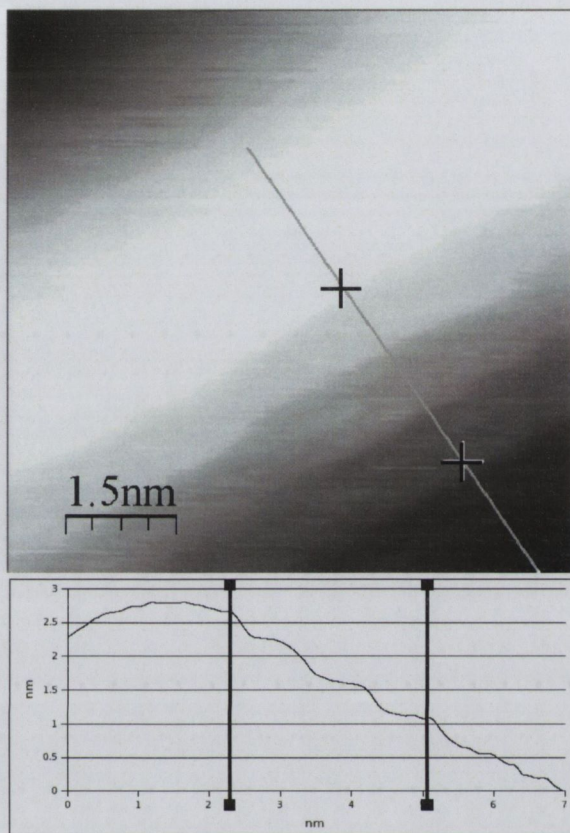


Fig. 7.2: STM image of the profile of a large oxide wire. The line profile shows terraces of $0.95\text{nm} \pm 0.09$ wide $0.53 \pm 0.05\text{nm}$ tall.

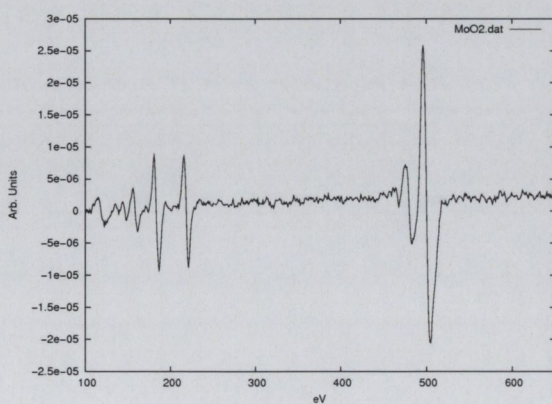


Fig. 7.3: Auger spectra of the MoO_2 oxide surface.

Species	Concentration
Mo	35%
O	65%

Table 7.1: The percent concentration on Mo and O from Auger of an MoO₂ oxide film.

7.2.3 LEED Analysis

The LEED pattern in Fig. 7.1A is that of Mo (110) with satellite spots along Mo [1 -1 -3] and [1 -1 3] direction, similar but more diffuse to that seen previously in chapter 6. In Fig. 7.1B, the satellite spots seen in 7.1A have become even more diffuse, and a new spot has developed along Mo [1-1 0]. In Figs. 7.1 C through E, the pattern, though still quasi-hexagonal, no longer has spots representative of Mo (110). Fig. 7.4 shows a close-up of the LEED pattern taken of the surface structure shown in Fig. 7.1C. This pattern gives a quasi-hexagonal structure with a lattice constant of $2.7 \pm 0.3 \text{ \AA}$ and an angle of $61 \pm 1^\circ$. These dimensions make this pattern an unsuitable match for Mo(110), which has dimensions 2.7 \AA but an angle of 70° , and therefore it must be that of the molybdenum oxide. However, with a unit cell of $a = 5.661 \text{ \AA}$, $c = 5.628 \text{ \AA}$, and $\beta = 120.95^\circ$, the LEED pattern is not what one would expect for the MoO₂ (010) unit cell (fig 7.1) (17). The fact that there is a glide plane along the MoO₂ c axis can explain missing odd order spots along that direction but cannot explain the missing spots along the a axis. Transmission high energy electron diffraction (THEED) images along the Mo₂(010) direction show weak odd order spots with bright even order spots (18). It is possible that the odd order spots are too weak to be detected with our LEED set-up. Another explanation may be that since the pattern is close in orientation and dimension to that of the MoO₂(010) oxygen

layer (see Fig. 6.4 in Chapter 6), that the pattern is the result of the oxygen unit cell at the surface, or perhaps a surface reconstruction. In the following discussion, we will assume no missing spots.

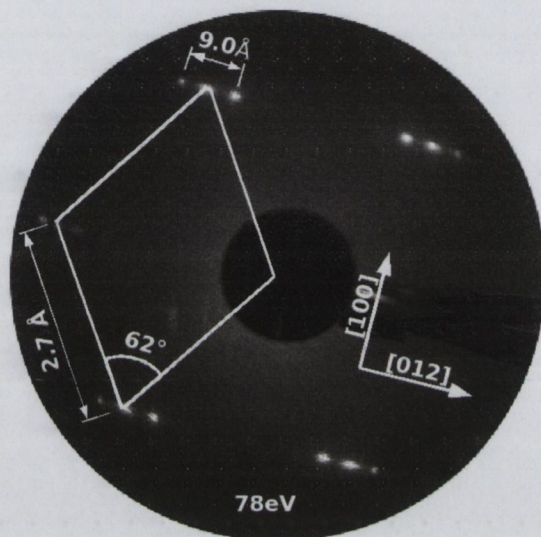


Fig. 7.4: LEED pattern taken at 78 eV of the surface structure shown in Fig. 7.1C. This pattern gives a quasi-hexagonal structure with a lattice constant of $2.7 \pm 0.3 \text{ \AA}$ and an angle of $61 \pm 1^\circ$.

7.2.4 LEED Spot Splitting

Another interesting feature of the LEED patterns from Fig. 7.1C to E is the presence of periodic splitting of the LEED spots over a range of beam energies. The splitting is well known and is an indication of regular step arrays on the surface (19; 20). This is explained by the superposition of the diffraction from atoms at the terraces and from atoms at the step edges. With one-dimensional step arrays, by changing energy, there is a periodic appearance of single and of split integer-order LEED spots. However, in this case, doublets of spots open and close to single spots. This is an indication of both ascending and descending staircases on the surface, as expected from the STM data. To further clarify this, a

diagram of the Ewald sphere for this system is drawn in Fig. 7.5.

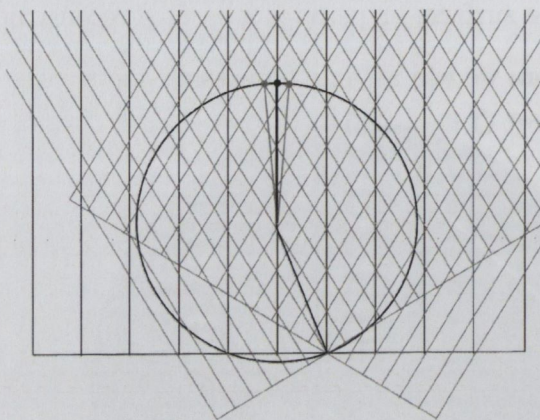


Fig. 7.5: Ewald sphere diagram for the MoO_2 "hill and valley" surface.

To illustrate the splitting, the graph of Fig. 7.6 shows a series of line profiles of the (0,1) and the (1,0) LEED spots over a range of beam energies from 58 eV to 173 eV. These profiles show that there are three distinct phases of spots over this energy range. Starting at 58 eV, there is one (0,1) and (1,0) LEED spot. With increasing energy, the spots split in two. As the energy increases beyond 68 eV, the spots continue to split apart. At 78 eV, the primary (0,1) and (1,0) spots become visible again. Furthermore, at this energy, the maximum separation between two symmetric multiplet spots occurs, as a result of spots from diffraction at ascending and descending steps coinciding. Therefore, the separation of the spots at this point is related to the average terrace width, allowing this value to be directly measured from LEED. We measured this value to be $9.0 \pm 0.9 \text{ \AA}$. As the energy continues to increase the primary spots disappear again and the two spots begin to coalesce until at an energy of 107 eV, only one primary spot is visible. A black line traces the path of the LEED spots in Fig. 7.6, and is representative of the lines of the Ewald sphere in Fig. 7.5.

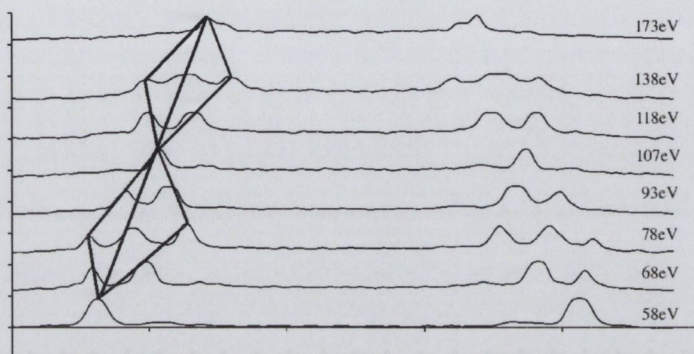


Fig. 7.6: Graph of the LEED spot profile at changing energy

The energy of the singular LEED spot which appears and disappears is related to the in-phase and out-of-phase scattering of electrons of adjacent terraces, respectively. Therefore, the “characteristic” beam energies at which they occur is a function of the step height and lattice parameter of the surface in the direction of the splitting. This was originally described by Henzler from which we obtain the equation (19):

$$E(s) = \frac{\hbar^2}{2m_0} \left(\frac{\pi}{r}\right)^2 \left[\left(s + \frac{g}{a}\right)^2 + \frac{r^2}{a^2} \right] \quad (7.1)$$

where \hbar and m_0 are Planck’s constant and the electron mass, respectively; r and a are the step height and lattice constant in the direction of splitting, respectively; and g is a fitting parameter to account for a horizontal offset at the lower step edge.

Using the measured value of the lattice constant from the LEED images, along with the voltages at which the primary spots, occur we can calculate the average step height with the following equation:

$$E(s+1)E(s) = \left(\frac{\hbar^2}{m_0}\right) \left(\frac{\pi}{r^2}\right) \left[s + \left(\frac{g}{a} + \frac{1}{2}\right) \right] \quad (7.2)$$

From this, we have an average step height of 4.6 Å. This value is in

agreement with the STM measurements, and close to the 4.86 Å value of the MoO₂ *b* axis.

From these experimental results, in addition to previous information about the oxidation of Mo(110), we can develop a structural model for the formation of these nanowires. This model will be described in the following section.

7.3 Nanowire Model

As the basis for a model of the molybdenum oxide nanowires, we will start with the surface oxide model described in the previous chapter. For reference, Fig. 7.7 shows the unit cell of MoO₂(010) oxide that forms a coincident lattice structure with the Mo(110) surface. The orientation of the MoO₂ overlayer is such that MoO₂[201] || Mo[1-1-3] and MoO₂[001] || Mo[3-3 2], as shown in Fig. 7.7. With this orientation, it can be seen that there are Mo-Mo dimer rows that form chains aligned with the MoO₂ *a* axis and close to the Mo(110) [00-1] direction, which is the same direction as the nanowires. Therefore, it is likely that the growth of the nanowires is related to these chains and that the chains are the building blocks that form the nanowires.

To describe the self-assembly of the oxide nanowires, a unit cell to be used as a “building block” needs to be constructed. For the basis of this unit cell, we used the orientation of the MoO₂ overlayer described above. Therefore, the cell of MoO₂ has a base in the (010) plane, with one side being the MoO₂ *a* axis, which defines the direction of the nanowires. The second side has one unit length in the [102] direction, perpendicular to the wires, and width of 9.66 Å, in agreement with the terrace width

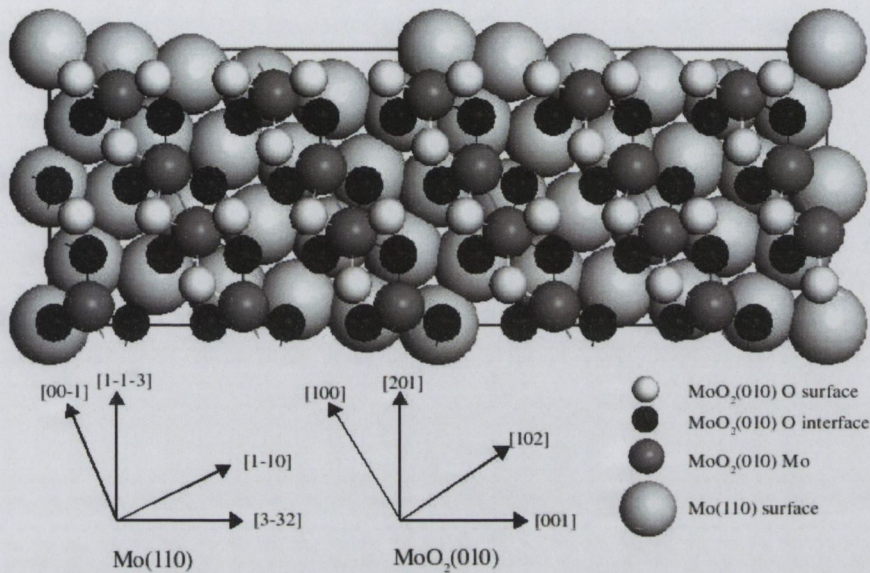


Fig. 7.7: Diagram showing the epitaxy of the MoO_2 (010) layer on $\text{Mo}(110)$.

measured in LEED and STM. Furthermore, if we make this cell one unit tall along the b axis, we have a MoO_2 “block” with a height of 4.86 \AA , within the error of the terrace height measured by LEED and STM (Fig. 7.8) and of the height of the smallest wires measured in Fig. 7.1.

Now that we have a building block for these wires, we can use it to better understand the growth of these wires. Starting with the smallest wires, which we measured to be $\sim 57 \text{ \AA}$ wide and $\sim 5 \text{ \AA}$ tall. The wire height of $\sim 5 \text{ \AA}$ can easily be associated with the height of one MoO_2 unit cell. However, to get the minimum width, we also need to know the dimensions of the $\text{Mo}(110)$ substrate. Comparing the dimensions of the $\text{Mo}[1-1\ 0]$ and the $\text{MoO}_2 [102]$ unit length, which in the diagram in fig 7.7 are $\sim 5^\circ$ apart, we see that there is a 13:6 relationship between them, giving a smallest common integer length of 58 \AA . Therefore, while the initial surface oxide layer grows highly strained with a coincidence

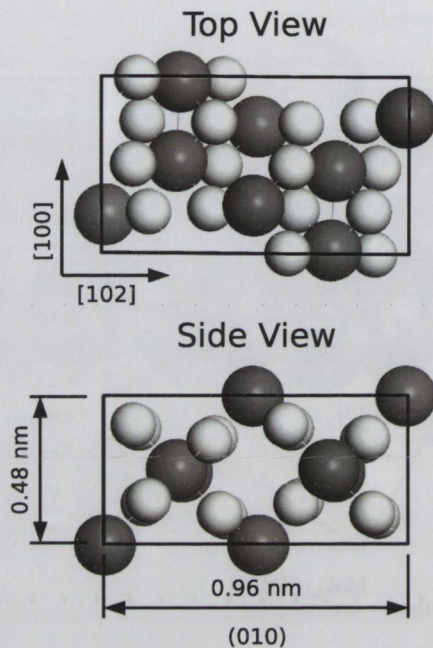


Fig. 7.8: Diagram of the MoO₂ building block.

along the Mo[1 -1 3] direction, it is likely that with the onset of three dimensional growth this coincidence changes running along the Mo[001] direction. This gives a larger, less strained MoO₂ overlayer unit cell which runs along the MoO₂ [100] direction, and is 6 units wide in the perpendicular [102] direction. This results in regular arrays of oxide nanowires.

As the oxide continues to grow, the oxide building blocks continue to assemble and according to the annealing time, we form various sizes of wires, as represented graphically in Fig. 7.9.

With regard to the largest wires, first we can determine the orientation of the two surface facets that make up the sides of the wires. From the above model, and in agreement with the slope of faces as measured by STM, we determined the surfaces to be MoO₂ (021) and (02-1) (Fig. 7.10). The (0 2 1) surface (Fig. 7.11) has previously been identified as a

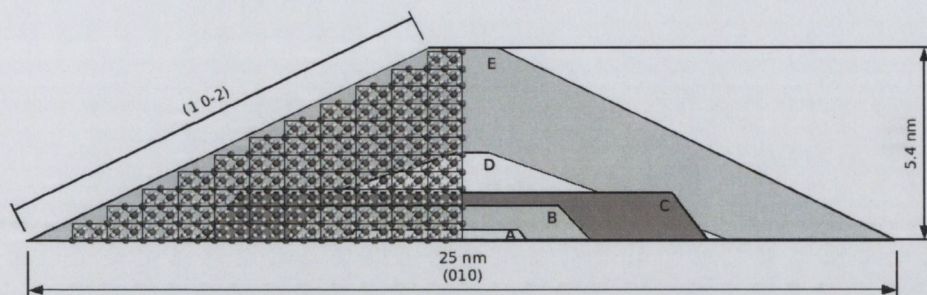


Fig. 7.9: Diagram of the various MoO_2 wire sizes measured with STM.

stable low energy surface for rutile and distorted rutile oxides (21; 22; 23). The stability of the distorted rutile (0 1 2), (0 2 1) and rutile (2 1 0) surface stems from it being made of charge balanced M_2O_4 layers (Tasker type II), thus eliminating the need for a charge redistribution to lower the surface energy of the initial MoO_2 (0 1 0) type III surface.

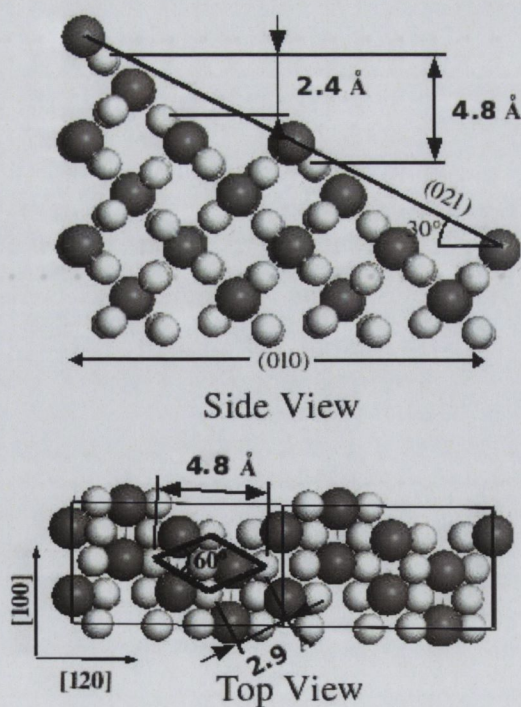


Fig. 7.10: An atomic model of the side and top views, respectively, of the oxide facet structure with the planes identified.

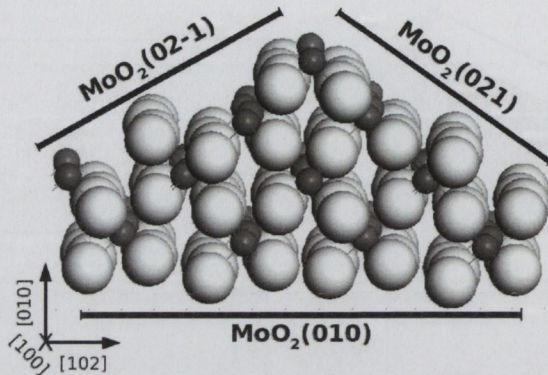


Fig. 7.11: A diagram of the oxide facet structure with the planes identified. The white spheres are Oxygen atoms and the grey spheres are Molybdenum atoms. It is a slice taken in the (2 0 -1) plane looking along the a axis (along the faceted rows).

7.3.1 Surface Energy Calculations

In order to quantify this, we employed DFT total energy calculations to determine the surface energy for the MoO_2 (0 1 0) and (0 2 1) surfaces. Furthermore, for comparison we also calculated the surface energy of the MoO_2 (0 1 1) surface, which is commonly considered the lowest energy rutile surface (21). For the calculations, we used the conventional approach in which the surface energy γ is determined by:

$$\gamma = (E_{slab} - NE_{bulk})/2A \quad (7.3)$$

where E_{slab} is the total energy of a slab of MoO_2 crystal cleaved to the desired orientation, N is the number of layers in the slab, A is the area of the surface, and E_{bulk} is the total energy of a bulk layer. For the calculations, we employed VASP with PAW LDA pseudopotentials with CA exchange functional (24; 25; 26; 27). For all geometries, five unit layer slabs were used, each containing 60 atoms except for the (010) which contained 59 in order to provide oxygen terminations at each surface. We

$\{hkl\}$	γ_{hkl} (J/m ²)	$\frac{\gamma_{hkl}}{\cos(\phi)}$
{010}	3.38	3.38
{021}	1.91	2.11
{011}	1.28	1.81

Table 7.2: DFT Calculated surface energy.

used Γ centered (8 x 8 x 1) k-point grids for the two low index surfaces and a (4 x 8 x 1) k-point grid for the (021) surface. The middle layer was constrained allowing all the other layers to relax by minimizing the Hellman-Feynman forces to less than 0.01 eV / Å. The calculated surface energies resulting from these calculations are listed in Table 7.2.

7.3.2 Theory of Periodic Faceting

We have now shown with DFT that the faceted MoO₂ (0 2 1) and (0 2 -1) surface would have a lower surface energy than the original (0 1 0) surface. However, to fully describe the surface energy of a periodically faceted “hill and valley” surface, we must employ the elastic theory of a periodically faceted surface, developed by Andreev and Marchenko (28; 29). This theory has been used to describe the periodic faceting of many surfaces including vicinal metals, Si (113) and Al₂O₃ (10-10) (30; 31; 32).

The basis of the theory is that the surface free energy of this type of surface is a competition between the surface energy $F(D)$ of the faces of length (D) and the energy of the convex and concave edges where two faces meet. This is illustrated in Fig. 7.12 and is described by the equation:

$$F(D) = \frac{\gamma(\phi)}{\cos(\phi)} + \frac{\eta(\phi)}{D} - \frac{C(\phi)\tau^2}{YD} \left| \frac{D}{a} \right| \quad (7.4)$$

where $\gamma(\phi)$ is the surface free energy, η is the average energy of the con-

cave and convex edges per unit length, C is a geometric factor accounting for the symmetry of the intrinsic surface stress tensor τ , Y is Young's modulus, and a is the lattice parameter. From this equation there exists an optimal periodicity D_{min} which defines the lowest energy surface.

$$D_{min} = a \exp\left(\frac{\eta(\phi)Y}{C(\phi)\tau^2} + 1\right) \quad (7.5)$$

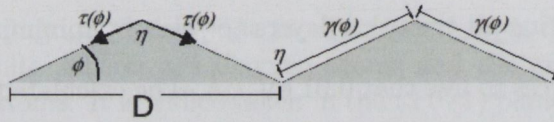


Fig. 7.12: Illustration of a faceted surface.

As there is little information available on the elastic properties of MoO_2 , making the determination of D_{min} for this system is not readily possible. However, these too can be calculated with DFT. In this case, we employed CASTEP due to its integrated algorithm for this purpose using LDA ultra-soft pseudopotentials with the CA-PZ exchange correlation functional (33; 34; 35) and a $(8 \times 8 \times 8)$ k-point grid centered at the γ point. By applying homogeneous strains of ± 0.005 and 0.010 , and calculating the resulting stresses, we were able to determine the 20 elastic constants for the monoclinic MoO_2 crystal, from which it is easy to determine Young's modulus along the three crystallographic axes. $Y_a = 339.60$ GPa, $Y_b = 184.34$ GPa, and $Y_c = 221.80$ GPa. It has been shown that this method can reliably determine the elastic constants of oxides (36).

By making some reasonable assumptions for the unknown values used in equation 7.5, along with the calculated values from above and the measured periodicity from STM as D_{min} , we arrive at an acceptable value

for τ . We used $\eta = 20 \text{ meV} / \text{\AA}$, $Y = 200 \text{ GPa}$ and $C = 1$ giving $\tau = 1.66 \text{ J} / \text{m}^2$. Considering that the surface stress τ is the strain derivative per unit area of the surface energy, it follows that the approximation $\tau = 1.66 \text{ J} / \text{m}^2$ is a reasonable value for a surface with an energy of $1.91 \text{ J} / \text{m}^2$ (37). Therefore, it is reasonable that the 30 nm periodicity of the facets is D_{min} , and the system is at equilibrium according to Marchenko's theory.

Now, if we take another look at Fig. 7.11, one can see the unidirectional anisotropy of this faceted surface, i.e. there are rows of oxygen atoms and Mo-Mo dimers that run along the MoO_2 $[1\ 0\ 0]$ direction (into the page), whereas Mo and O atoms alternate along the $[1\ -1\ 2]$ and $[1\ 1\ 2]$ directions (along the facets). This anisotropy is also reflected in the elastic properties of the crystal and therefore it is related to the direction of the faceting of the surface. From the previously calculated values for Young's modulus, we can see that in the direction along the facets, between the b and c axis, the value is $\sim 200 \text{ GPa}$. However, along the wires in the direction of the a axis, the value is $Y = 340 \text{ GPa}$. Since $D_{min} \propto \exp^{kY}$, it is easy to understand why the crystal facets in a direction perpendicular to the MoO_2 a axis.

The results of these calculations are reassuring. They show that by having a faceted surface with $(0\ 2\ 1)$ and $(0\ 2\ -1)$ facets, the film will have a lower surface energy than with the original $(0\ 1\ 0)$ orientation. Therefore, we have a case where the substrate initially causes a film to grow in an orientation that is normally forbidden, but an electron redistribution at the interface causes the film to wet the substrate's surface. However, the stability effect of the interface is localised and as the film continues to grow, the MoO_2 $(0\ 1\ 0)$ surface becomes unstable and this, coupled

to a surface energy anisotropy, leads to the spontaneous formation of a periodically faceted MoO_2 surface with lower energy (0 2 1) and (0 2 -1) faces. Furthermore, a faceting period of ~ 30 nm is likely an equilibrium state for this surface.

Bibliography

- [1] P. W. Tasker, *J. Phys. C: Solid State Phys.* **12**, 4977 (1979).
- [2] J. Gustafson, A. Mikkelsen, M. Borg, E. Lundgren, L. Kohler, G. Kresse, M. Schmid, P. Varga, J. Yuhara, X. Torrelles, et al., *Phys. Rev. Lett.* **92**, 126102 (2004).
- [3] J. Gustafson, A. Mikkelsen, M. Borg, J. N. Andersen, E. Lundgren, C. Klein, W. Hofer, M. Schmid, P. Varga, L. Kohler, et al., *Phys. Rev. B* **71**, 115442 (2005).
- [4] C. T. Campbell, *Phys. Rev. Lett.* **96**, 066106 (2006).
- [5] M. Todorova, W. X. Li, M. V. Ganduglia-Pirovano, C. Stampfl, K. Reuter, and M. Scheffler, *Phys. Rev. Lett.* **89**, 096103 (2002).
- [6] A. Stierle, F. Renner, R. Streitl, H. Dosch, W. Drube, and B. C. Cowie, *Science* **303**, 1652 (2004).
- [7] D. J. Siegel, L. G. Hector, and J. B. Adams, *Phys. Rev. B* **65**, 085415 (2002).
- [8] R. Benedek, M. Minkoff, and L. H. Yang, *Phys. Rev. B* **54**, 7697 (1996).
- [9] M. W. Finnis, *J. Phys.: Condens. Matter* **8**, 5811 (1996).
- [10] J. Purton, S. C. Parker, and D. W. Bullett, *J. Phys.: Condens. Matter* **9**, 5709 (1997).
- [11] R. Benedek, A. Alavi, D. N. Seidman, L. H. Yang, D. A. Muller, and C. Woodward, *Phys. Rev. Lett.* **84**, 3362 (2000).
- [12] K. Reuter and M. Scheffler, *Appl. Phys. A* **78**, 793 (2004).
- [13] H. C. Galloway, P. Sautet, and M. Salmeron, *Phys. Rev. B* **54**, R11145 (1996).
- [14] M. W. Finnis, *Acta Metall. Mater.* **40**, S25 (1992).
- [15] D. M. Duffy, J. H. Harding, and A. M. Stoneham, *Acta Metall. Mater.* **40**, S11 (1992).
- [16] A. A. Golovin, M. S. Levine, T. V. Savina, and S. H. Davis, *Phys. Rev. B* **70**, 235342 (2004).
- [17] B. Brandt and A. Stapski, *Acta. Chim. Slov.* **21**, 661 (1967).
- [18] V. Bhosle, A. Tiwari, and J. Narayan, *J. Appl. Phys.* **97**, 083539 (2005).

- [19] M. Henzler, *Applied Physics* **9**, 11 (1976).
- [20] M. Horn-von Hoegen, *Z. Krist.* **214**, 684 (1999).
- [21] P. M. Oliver, G. W. Watson, E. T. Kelsey, and S. C. Parker, *J. Mater. Chem.* **7**, 563 (1997).
- [22] A. Howard, C. Mitchell, D. Morris, R. Egdell, and S. Parker, *Surf. Sci.* **448**, 131 (10 March 2000).
- [23] F. Jones, R. Egdell, A. Brown, and F. Wondre, *Surf. Sci.* **374** (10 March 1997).
- [24] G. Kresse and J. Furthmüller, *Phys. Rev. B* **54**, 11169 (1996).
- [25] P. Blöchl, *Phys. Rev. B* **50**, 17953 (1994).
- [26] G. Kresse and J. Joubert, *Phys. Rev. B* **59**, 1758 (1999).
- [27] D. M. Ceperley and B. J. Alder, *Phys. Rev. Lett.* **45**, 566 (1980).
- [28] A. F. Andreev, *J. Exp. Theor. Phys.* **80**, 2042 (1981).
- [29] V. I. Marchenko, *J. Exp. Theor. Phys.* **81**, 1141 (1981).
- [30] S. Rousset, V. Repain, G. Baudot, Y. Garreau, and J. Lecoœur, *J. Phys.: Condens. Matter* **15**, S3363 (2003).
- [31] J. J. Metois, A. Saul, and P. Muller, *Nat. Mater.* **4**, 238 (2005).
- [32] M. Huth, K. Ritley, J. Oster, H. Dosch, and H. Adrian, *Adv. Funct. Mater* **12**, 333 (2002).
- [33] M. D. Segall, P. J. D. Lindan, M. J. Probert, C. J. Pickard, P. J. Hasnip, S. J. Clark, and M. C. Payne, *J. Phys.: Condens. Matter* **14**, 2717 (2002).
- [34] D. Vanderbilt, *Phys. Rev. B* **41**, 7892 (1990).
- [35] D. M. Ceperley and B. J. Alder, *Phys. Rev. Lett.* **45**, 566 (1980).
- [36] S. Shang, Y. Wang, and Z.-K. Liu, *Appl. Phys. Lett.* **90**, 1909 (2007).
- [37] R. Shuttleworth, *Proc. Phys. Soc. London, Sect. A* **63**, 444 (1950).

Chapter 8

The Oxidation Rate of MoO_2

The initial stages of oxidation of the Mo(110) surface up to a closed oxide layer happens rapidly at 900 °C and 10^6 Torr oxygen. Therefore, no precursor states have been observed, and there is no information about the onset of oxidation.

After the formation of a close-packed oxide film on the Mo substrate, further oxide growth requires that Mo substrate atoms, and/or chemisorbed oxygen surface atoms move into and through the developing oxide film towards the metaloxide and/or oxidegas interface, respectively. The migrating species is generally assumed to be ionic *e.g.*, for Al, Fe, Cu, and Ta substrates (1; 2; 3; 4; 5; 6). In order to maintain overall charge neutrality in the film, while also dissociating molecular oxygen at the oxide surface, electrons must also move through the oxide.

Since the MoO_2 film is considered to be metallic, we can assume that the electron transport through the oxide occurs at a faster rate than the chemical diffusion of Mo cations. The electric field induced by negatively charged oxygen anions at the oxide surface will retard further electron transport but enhance cation transport (2; 3; 4). Under the constraint that no net charge is transported through the oxide film, the magnitude

of the established electric field will be such that the ion current equals the charge current of the more mobile electrons. This gives the steady state equation:

$$J_i = J_e \quad (8.1)$$

where J is the current of the ion i and electron e , respectively. To obtain the growth rate dL/dt one integrates the following equation after inserting the appropriate equation for the rate limiting factor (4).

$$dL/dt = RJ_iJ_e \quad (8.2)$$

The parameter R is the oxide volume that one of the diffusing ions creates in the oxidation process. From Fromhold and Cook, integrating Eqn. 8.2 for the ion diffusion limiting case results in an expression for the oxide thickness L dependent on the oxidation time t (7):

$$L(t) = \frac{1}{\alpha} \ln(1 + \beta t) \quad (8.3)$$

Therefore, it is expected that from the Cabrera and Mott theory that ion current limited oxide growth leads to a logarithmic growth curve. At the early stages of oxidation, the oxide thickness increases very rapidly independent of the temperature. This growth rate quickly changes into a logarithmic mode and finally approaches a constant value.

By making the assumption that the base of these wires is at the substrate interface, we can consider the wire height as a measure of film thickness. Therefore, if we take the area under the line profiles, we can measure the volume of oxide formed per unit time. From this, we can plot the growth rate in Å/s of an equivalent flat MoO₂ film. Figure 8.1 shows the MoO₂ oxide wire height and equivalent flat oxide film thickness

over time. In this figure, we see that these wires follow a linear growth curve to a maximum height of ~ 5 nm and then stop.

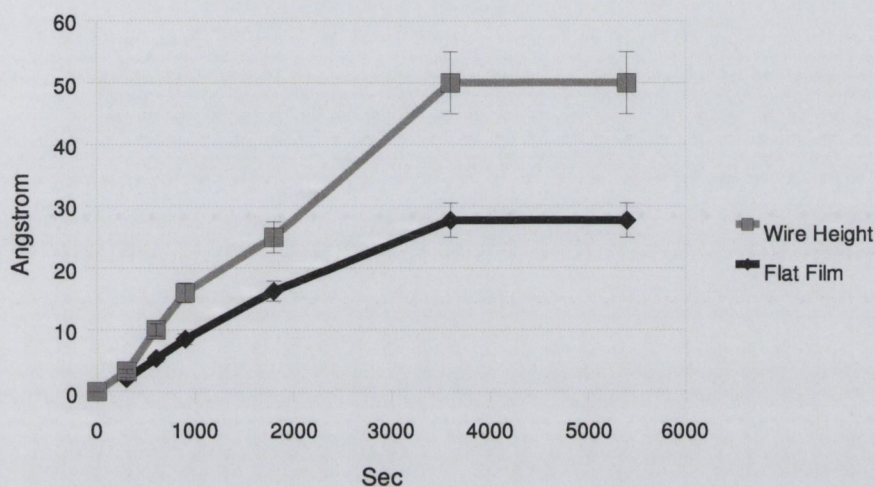


Fig. 8.1: Graph of the nanowire height and thickness of an equivalent flat MoO_2 film over time.

There are linear rate laws for two types of limiting processes, thermionic electron emission and a rate limiting phase boundary reaction (4). Since MoO_2 is known to be metallic, it is doubtful that the oxidation process would follow a law in which electrons are the less mobile species *i.e.* the thermionic emission law. Furthermore, if the base of the wires does in fact reach down to the substrate, then the regions between adjacent wires will remain at a constant thickness. Therefore, these areas would provide a path for ion transport that would remain constant over time and lead to a linear growth rate (4). With a network of these diffusion paths, the linear reaction process can follow one of two ways. The Mo ions may travel up through the areas, with electrons traveling through the oxide to dissociate the molecular oxygen. Here, the oxidation reaction occurs on the oxide surface phase boundary with the gas as illustrated in Fig 8.2.

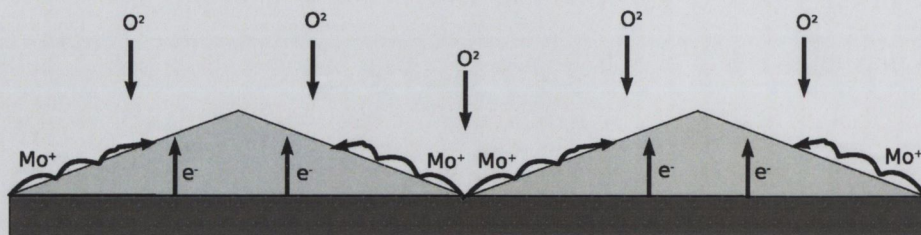


Fig. 8.2: Illustration of Mo ions traveling up through the boundaries between the wires, with electrons traveling through the oxide to dissociate the molecular oxygen. The oxidation reaction occurs on the oxide surface phase boundary with the gas.

In the second case, the oxidation reaction follows with the oxygen reaching the metal surface through the diffusion paths and the oxidation occurs at the Mo/MoO₂ phase boundary, as in the case of SiO₂/Si (Fig. 8.3) (8).

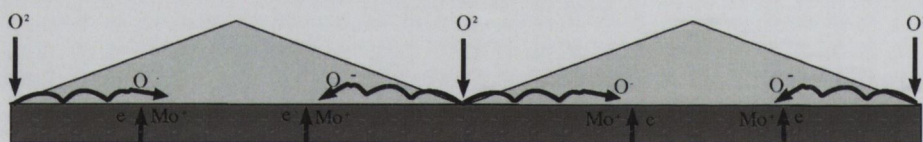


Fig. 8.3: Illustration of the oxidation reaction occurring with the oxygen reaching the metal surface through the diffusion paths and the oxidation reaction occurs at the Mo/MoO₂ phase boundary.

According to the STM data in figure 8.4, it appears that the oxidation occurs at the MoO₂ gas interface. In this image, there are several regions marked by arrows. In these regions, it can be seen that the wires grow on top of existing wires. This indicates that the oxide is forming at the interface with the gas, and therefore the Mo must be diffusing through the oxide layer in order for the oxidation to continue.

Considering the average growth rate is $\sim 4.7 \times 10^{-4}$ nm / s and that it takes ~ 28.5 oxygen atoms and ~ 14.3 Mo atoms to make one nm³ of MoO₂, that would mean a consumption rate of $\sim 1.3 \times 10^{-2}$ oxygen

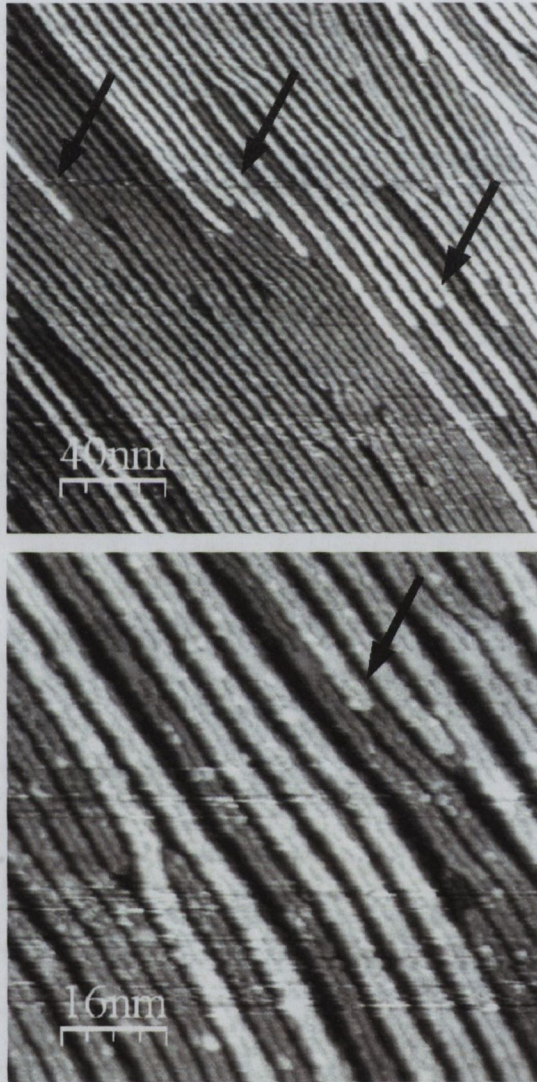


Fig. 8.4: In this STM, image there are several regions marked by arrows. In these regions, it can be seen that the wires grow on top of existing wires, indicating Mo is diffusing through the diffusion paths and the oxide is forming at the interface with the gas

atoms and 6.5×10^{-3} Mo atoms per nm^2 s. Therefore, there is a constant diffusion rate of Mo through the diffusion paths of 6.5×10^{-3} Mo per nm^2 s, or the oxidation is limited by oxygen. The rate of oxygen supply from the gas phase to the surface is controlled by the number of gas molecules R hitting a surface per unit time and area, at constant O_2 pressure and constant temperature T . According to the kinetic gas theory, this obeys the following equation:

$$R = \frac{p_{\text{O}_2}}{\sqrt{2\pi mkT}} \quad (8.4)$$

where m is the mass of the gas molecule and k is Boltzmann's constant. If oxygen supply from the gas phase to the oxide surface limits the oxide-film growth rate, a linear growth law would occur because R is constant with time. At 1×10^{-6} Torr oxygen in a room temperature chamber, the arrival rate of molecular oxygen to the surface is $3.6 \text{ O}_2 \text{ nm}^{-2} \text{ s}^{-1}$. This gives a sticking coefficient of 1.9×10^{-3} for a linear growth rate limited by oxygen adsorption. There is no available information about the sticking coefficient of MoO_2 , however one would expect it to be quite low for an oxide that is close to its decomposition temperature.

The normal growth procedure is to cool the wires in oxygen at a rate of $100 \text{ }^\circ\text{C}$ per minute. During this cooling, the Mo diffusion rate will decrease with a rate proportional to the diffusion coefficient, D_{eff} :

$$D_{eff} = a^2 \nu \exp\left(\frac{-w_i}{k_b T}\right) \quad (8.5)$$

However, the oxygen sticking coefficient will likely increase with a decrease in temperature, leading to stoichiometric MoO_2 in the AES data. If we stop the annealing process more abruptly in oxygen, after 30 min of

annealing the Auger data shows a 4:1 Mo:O ratio, Fig. 8.5 trace labeled Pre Anneal. The STM image of these wires in Fig. 8.6 shows poorly formed wires with a rough profile. This sample was then annealed in 10^{-6} Torr oxygen at 250 °C for one hour, the Mo:O ratio measured with Auger is 2.6:1 (Fig. 8.5 trace labeled Post Anneal), and the STM data shows smooth, well formed wires (Fig. 8.7). This indicates that the oxidation is limited by the rate of oxygen intake at the MoO_2 gas interface. However, in order to verify this, rate measurements need to be made with varying pressures to investigate if the growth rate follows the oxygen arrival rate. Currently, $\sim 10^{-6}$ Torr oxygen is the limit for our e-beam heater, but recently we have made a separate oxidation chamber more suitable for pressures of at least 10^{-4} Torr.

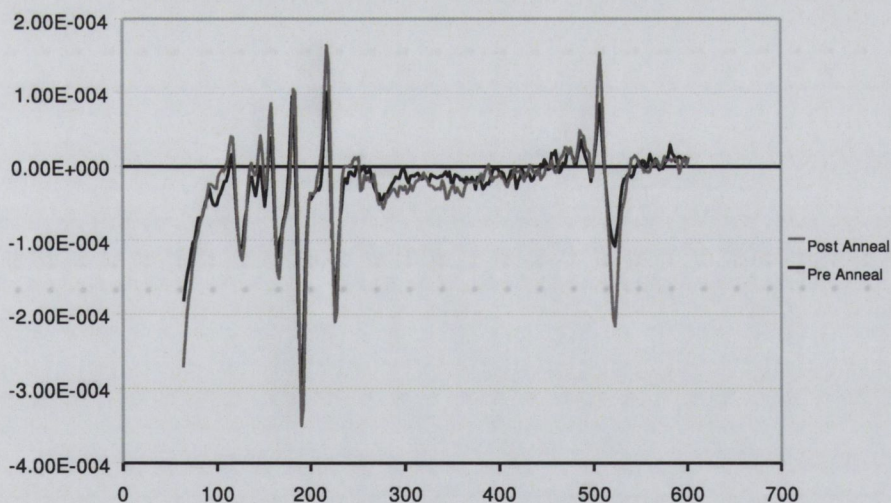


Fig. 8.5: Trace labeled pre-anneal shows the AES spectra of a sample cooled abruptly in oxygen after 30 min, showing a 4:1 Mo:O ratio. Trace labeled post-anneal shows the AES spectra of the sample after annealing in oxygen at 250 °C at 1×10^{-6} Torr for one hour, showing a Mo:O ratio of 2.6:1.

Once the surface reaches the lowest energy “hill and valley” period, we cannot measure the change in oxide thickness. Instinctively, one would

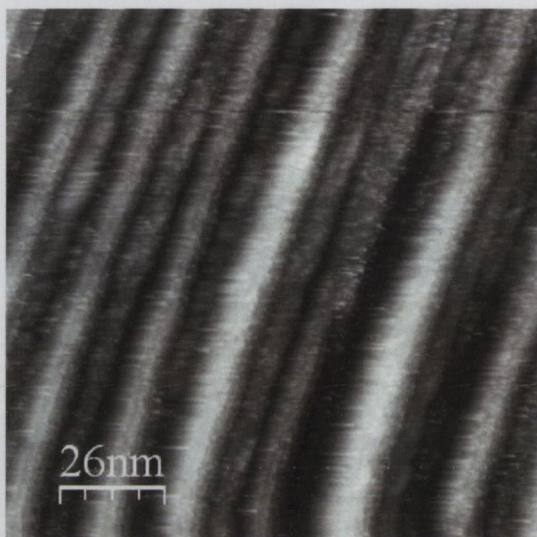


Fig. 8.6: STM after stopping the annealing process more abruptly, i.e. in oxygen after 30 min.



Fig. 8.7: STM after annealing the sample in oxygen at 250 °C at 1×10^{-6} Torr for one hour.

think that once the surface reaches the lowest energy “hill and valley” period, the film would grow thicker, filling the Mo diffusion paths (Fig. 8.8). Then it would be likely that the growth would change to the logarithmic growth curve from the Cabrera and Mott theory of ion current limited oxide growth. However, this is speculation since we have no *in situ* means to measure the oxide thickness.

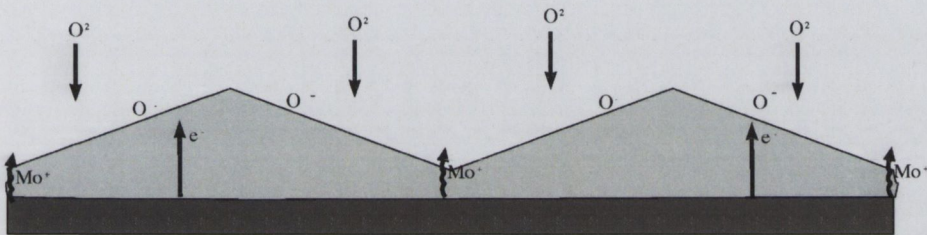


Fig. 8.8: Possible growth mechanism once the diffusion paths are filled.

Bibliography

- [1] L. P. H. Jeurgens, W. G. Sloof, F. D. Tichelaar, and E. J. Mittemeijer, *J. Appl. Phys.* **92**, 1649 (2002).
- [2] N. Cabrera and N. F. Mott, *Rep. Prog. Phys.* **12**, 163 (1949).
- [3] A. T. Fromhold and E. L. Cook, *Phys. Rev.* **163**, 650 (1967).
- [4] K. R. Lawless, *Rep. Prog. Phys.* **37**, 231 (1974).
- [5] K. Reuter and M. Scheffler, *Appl. Phys. A* **78**, 793 (2004).
- [6] T. N. Rhodin, *JACS* **73**, 3143 (1951).
- [7] A. T. Fromhold and E. L. Cook, *Phys. Rev.* **175**, 877 (1968).
- [8] B. E. Deal and A. S. Grove, *J. Appl. Phys.* **36**, 3770 (1965).

Chapter 9

MoO₂ Nanowire Growth on

Mo(110)/Al₂O₃(11-20)

In order to be able to characterise the electrical properties of conducting nanowires, they must be on an insulating substrate. Refractory metals such as Molybdenum are known to grow in the (110) orientation on Sapphire, Al₂O₃ (1 1 -2 0) (1; 2). Therefore, if thin films of Mo(110) were grown on sapphire, with such a thickness that when oxidized the majority of the Mo in this film was incorporated into the oxide wires, the result would be MoO₂ nanowires on Al₂O₃.

From the literature, it has been reported that both MBE and PLD can produce epitaxial Mo(110) films with near perfect surfaces. The epitaxial relationship between bcc-Mo(110) and Al₂O₃ (1 1 -2 0) is Mo[111] || Al₂O₃ [0001] and Mo [112] || Al₂O₃ [1100] (1; 2). For MBE films grown at 800 °C, the initial growth of Mo has been shown to be three dimensional, poorly ordered island growth. This is attributed to a large 6.5% mismatch between the film and substrate. With further deposition, the films become smooth and by 25 nm thickness, are of excellent quality (2). An

alternate method of growth by PLD at 200 °C, followed by an 800 °C anneal, produced 7.5 nm thick atomically flat films as characterised by AFM XRD and RHEED (1). Using these recipes as a guideline, we were able to produce high quality Mo(110) films via magnetron sputtering. In this chapter, I will describe our method of using magnetron sputtering followed by high temperature annealing to produce high quality Mo(110) films. The chapter will conclude with some experimental results of MoO₂ wires grown on these films.

9.1 Mo Film Growth

The first step was to out-gas the Sapphire substrates in UHV by annealing at 900 °C for several hours. They were then transferred to the magnetron chamber for further out-gassing at 1×10^{-7} Torr and 600 °C for two hours. The Mo films were then grown on the substrate at 600 °C at a rate of 0.4 Å/s as measured by a quartz crystal balance at a pressure of 1×10^{-5} Torr Ar and a DC power of 30 W. After the film growth, they were transferred in air, placed in a sample holder and introduced into the UHV chamber for characterisation.

9.2 Film Characterisation

One of the main problems encountered with this process was maintaining a good electrical contact between the film and sample holder. Unfortunately, the machining process involved with making the sample caps leaves the inside of the cap tapered such that the film or sample surface is only in contact with the sample cap at the very edge of the sample. With oxidation and high temperature treatments, this contact is quickly

eroded and we are no longer able to probe the sample with electrons. The best solution so far is to use a washer made from Molybdenum foil placed in between the sample and cap to help increase the contact area between the film and cap. It was still found that the film seems to vanish under the contact areas at temperatures above ~ 1300 °C, possibly due to the metal migrating from the sapphire to the washer, resulting in the loss of electrical contact. This connection could be temporarily restored, probably through a static discharge with LEED at beam energies greater than 200 eV, and a pattern would appear but then disappear once the energy was lowered below around 100 eV. Therefore, we have some good LEED images of clean and oxidized Mo(110) on sapphire treated in a similar fashion as the single crystal, but no STM or AES data (Fig 9.1). Therefore, we are reasonably confident that this method will work. However, thus far, we have no conclusive STM data for the growth of high quality oxide nanowires like that shown on the single crystal.

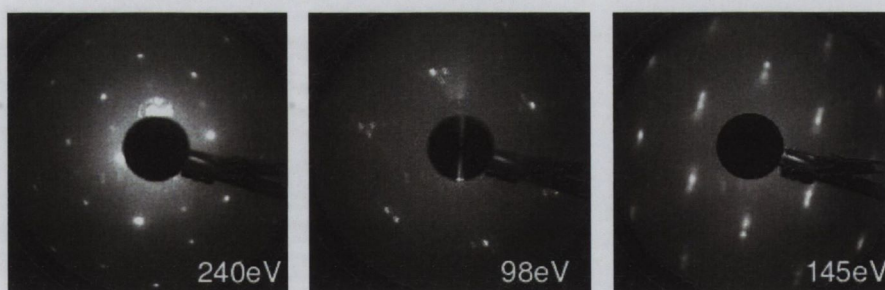


Fig. 9.1: LEED images of a clean 60 nm Mo(110) film on Al_2O_3 , a MoO_2 (010) surface oxide on a 60 nm Mo(110) film on Al_2O_3 , and of a periodically faceted MoO_2 surface oxide on a 60 nm Mo(110) film on Al_2O_3 , respectively

We developed a cleaning and oxidation process that doesn't exceed ~ 1300 °C. Once the samples were reintroduced into the UHV system, each step of the procedure was characterised with LEED, AES and STM.

The as received films did not produce a LEED pattern or any respectable STM images due to large amounts of contamination at the surface absent of any structural order. The black trace labeled “as received” in Figure 9.2 shows the Auger spectra of a 50 nm thick film after introduction into the chamber. The relative concentrations of the species present at the surface are presented in Table 9.1. From this table, one can see that the surface is very dirty, most notably is the S content of 42 % at 150 eV and a small amount of Ti at 383 eV. However, the S content is likely overestimated due to an overlap with a minor Mo peak located at 148 eV (for comparison see spectra labeled annealed and flashed in fig 9.2). Because the peak to peak height of the sum of two overlapping spectra is non-linear, it is only possible to extract the individual contributions provided that standards of both species are available (3). In any case the exact amount of S on the surface is unimportant.

Species	Percent concentration
Mo	23 %
O	17 %
C	47 %
Ti	1.3 %
S	42 %

Table 9.1: Auger Concentrations

This film was then annealed overnight at 700 °C (the maximum temperature of the resistive heater) to flatten the surface and achieve a monocrystalline film (1). Figure 9.3 shows a STM image of the Mo film surface after one such anneal. As you can see in this image, the surface has formed atomic terraces of a height expected for Mo(110) ($2.3 \pm 0.2 \text{ \AA}$ tall) and $\sim 20 \text{ nm}$ wide. The surface is also covered with small islands of the same height as the terraces. These islands are most likely Mo islands

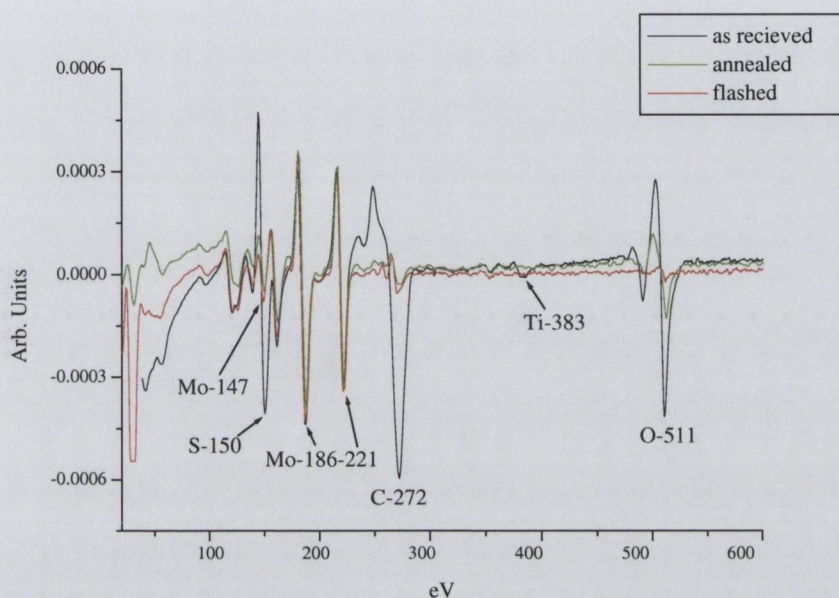


Fig. 9.2: Auger spectra of as received, annealed and flashed Mo(110) films on Al_2O_3 .

that are yet to coalesce into the terraces. It was noted that while annealing the films at temperatures up to $700\text{ }^\circ\text{C}$ improved the quality of the films, a temperature above $800\text{ }^\circ\text{C}$ was necessary to produce long-range crystal coherence and surface flatness (1).

What is more interesting is the LEED image in the bottom right corner of the figure, taken at 47 eV , which shows a $(5\sqrt{3} \times 3)$ superstructure on the Mo(110) surface. In real space, such a structure would have dimensions of 13.35 \AA in the Mo[1-1 0] and 15.75 \AA in the Mo[0 0-1] directions. It is understood from the literature that the Mo (110) surface of bulk crystals or MBE grown films is free of any reconstructions or $(5\sqrt{3} \times 3)$ adsorbate structure. However, Fruchart et. al did see similar structures by RHEED on Mo(110) grown by PLD on sapphire (1). This structure, which they called a (6×15) , would describe a superstructure

or similar shape and dimension as in figure 9.3 but rotated by $\sim 35^\circ$ with respect to the Mo $p(1 \times 1)$. They attributed this to the presence of a contamination diffusing to the surface during the anneal but could not detect it with Auger. They further noted that by annealing their sample above 800°C , the superstructures disappeared.

The Auger spectrum of this film is shown in Fig. 9.2 by the green trace labeled "anneal". The spectrum only shows the usual contaminants, O and C. Therefore, the 700°C anneal was sufficient to remove the S and Ti contaminants in addition to a large amount of the carbon and some oxygen (table 9.2). However, the composition of this superstructure is still unknown.

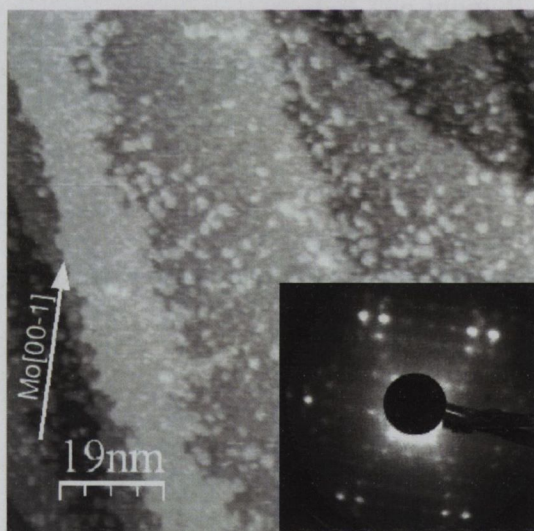


Fig. 9.3: STM image of the Mo(110) film surface grown on Al_2O_3 after annealing

By annealing the sample at 1000°C , with flashes to 1300°C , the superstructure disappears, similar to results obtained by Fruchart (1). Large scale STM images show an atomically flat surface with 2.3 ± 0.2 Å tall atomic terraces (fig 9.4). The LEED pattern in the bottom right

Species	Percent concentration
Mo	72%
O	15%
C	13%

Table 9.2: Auger Concentrations

corner of figure 9.4 shows a diffuse Mo(110) $p(1 \times 1)$ pattern, indicating a monocrystalline Mo(110) film with a diffuse pattern from adsorbates randomly distributed on the surface. On the smaller scale, the STM image in figure 9.5 shows the disordered adsorbates in the upper right region, as well as possible evidence of the superstructure discussed above. This structure, which is better visible in a close-up in the bottom right corner of figure 9.5, is a rectangular mesh with dimensions of 13.1 ± 1 Å along Mo $[-1 -1 0]$ by 14.3 ± 1 Å along Mo $[0 0-1]$ giving a dimension and orientation of that imaged by LEED in figure 9.3. The corrugation of this structure was measured by STM to be 0.08 Å.

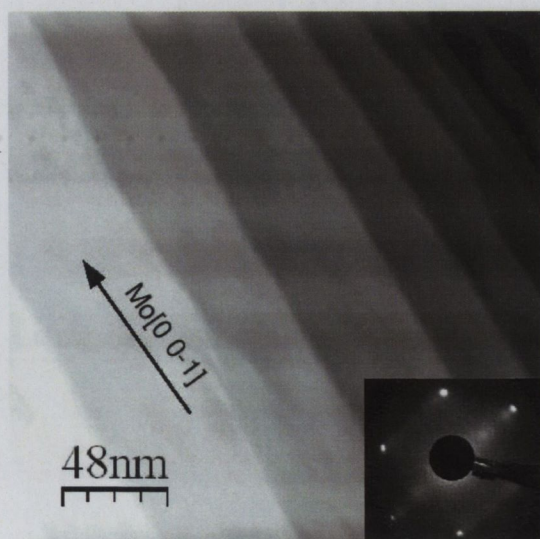


Fig. 9.4: STM and LEED images after annealing at 1000 °C, with flashes to 1300 °C

The sample was then annealed in 1×10^{-6} Torr oxygen at 1100 °C for

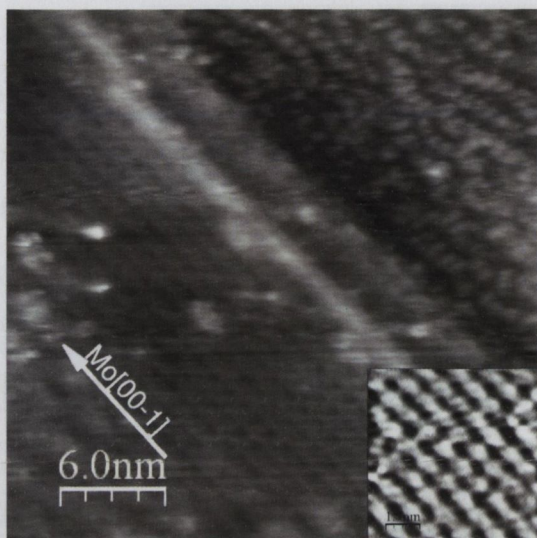


Fig. 9.5: STM image of the Mo(110) film surface grown on Al_2O_3 after flashing

one hour to remove the carbon and then flashed to $1300\text{ }^\circ\text{C}$ several times to clean surface of the residual carboxides and oxides. The STM data shows the surface is now free of the clusters which were seen in figure 9.3 and it is now a smooth film with atomic terraces. The LEED pattern is a diffuse Mo(110) with some streaking on the Mo[1-1 3] and Mo[1-1-3] directions indicating some residual surface oxide. The Auger data (fig 9.2 red trace, labeled flash), shows a small concentration of carbon and oxygen. As expected, flashing to $1300\text{ }^\circ\text{C}$ is not enough to completely remove all of the surface carbon and oxygen contamination.

9.3 MoO_2 Wires Grown on Mo(110)/ Al_2O_3

Next, the sample was oxidized at 1×10^{-6} Torr oxygen at $900\text{ }^\circ\text{C}$ for 30 min. The STM image in figure 9.7 shows MoO_2 nanowire growth. These wires have the same dimensions as the smallest wires seen on the Mo(110) single crystals (Fig. 7.1). These wires are of poor quality and

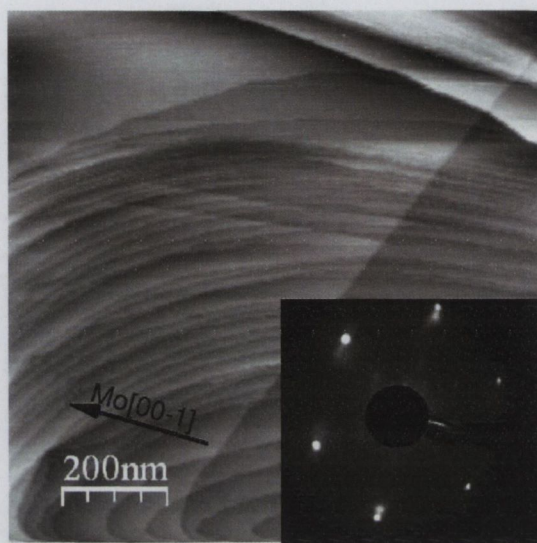


Fig. 9.6: LEED and STM image of the Mo(110) film surface grown on Al_2O_3 after annealing and flashing

appear contaminated with small clusters. The LEED pattern shown in the bottom right corner of this image is diffuse but representative of small wires. The Auger data shows there is considerable Carbon present on the surface. This carbon contamination is likely to be responsible for the poor quality of the wires.

This sample was flashed again to $1300\text{ }^\circ\text{C}$ several times to remove the oxide and carbon contamination and re-oxidised at 1×10^{-6} Torr oxygen at $900\text{ }^\circ\text{C}$ for 30 min. Figure 9.8a shows the STM image of the nanowires formed after this oxidation. They appear to be better quality than the previous oxidation but only slightly larger.

In an attempt to assess the viability of these wires at ambient conditions, the STM tip was retracted and STM chamber was vented with dry N_2 gas. The STM tip was extended and Figure 9.8b shows that these wires are still present on the surface. Next, the tip was again retracted and the chamber was opened to air. The tip was re-extended but sta-

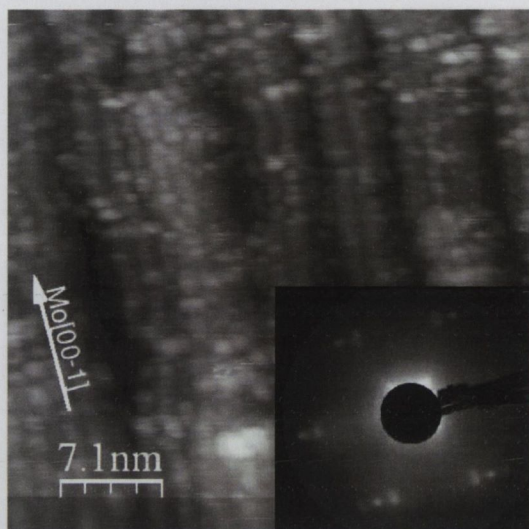


Fig. 9.7: The STM and LEED image of Mo(110) film oxidized at 1×10^{-6} Torr oxygen at $900 \text{ }^\circ\text{C}$ for 30 min.

ble tunneling conditions were not achieved and as a result, the images obtained were very noisy. Furthermore, nanowires could not be imaged. Because a W tip was used in this experiment, it itself will oxidize when the chamber is vented and the loss of image quality could be due to the degradation of the tip in addition to the film surface.

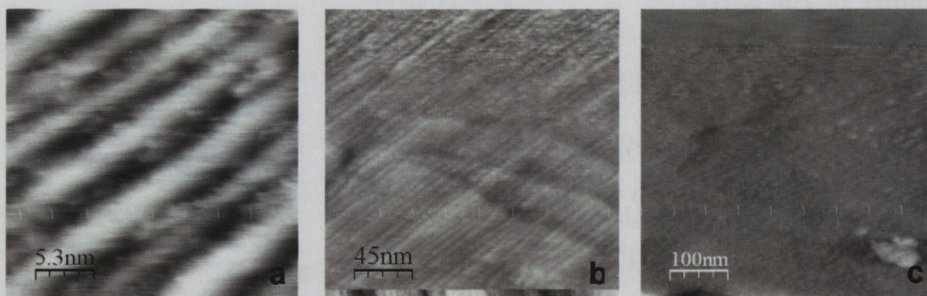


Fig. 9.8: STM images of oxidized Mo(110) film. (a) is in UHV. (b) is in N_2 . (c) is in air.

We have demonstrated that magnetron sputtering can produce good quality Mo(110) films on the Al_2O_3 (1 1 -2 0) surface. These films show promise for the development of MoO_2 nanowires on an insulating sub-

strate. Future work will be to grow thinner Mo films and oxidise the film down to the substrate.

Bibliography

- [1] O. Fruchart, S. Jaren, and J. Rothman, *Appl. Surf. Sci.* **135**, 218 (1998).
- [2] R. Ward, E. Grier, and A. Petford-Long, *J. Mater. Sci. - Mater. Electron.* **14** (2003).
- [3] J. K. O. Asante, W. D. Roos, and M. F. Maritz, *Surf. Interface Anal.* **31**, 856 (2001).

Chapter 10

Conclusions and Future Work

10.1 Conclusions

The oxidation of Mo(110) was studied and it was found that a bulk like oxide of MoO₂ (010) grows epitaxially on the surface at 1000 °C and 1 x 10⁻⁶ Torr oxygen pressure. LEED and STM data were used to give a detailed analysis of the oxide surface structure. From this experimental data, a model was built and through the use of DFT calculations, we showed that a strained bulk like MoO₂(010) film is in excellent agreement with the experimental data. The coincidence structure can be described in matrix notation by:

$$\begin{bmatrix} 1 & 8 \\ -4 & 2 \end{bmatrix}$$

giving a MoO₂ overlayer with MoO₂[201] || Mo[1-1-3] and MoO₂[100] || Mo[00-1]. The oxide overlayer is strained by ~5.5 % and skewed by 4.9°. The DFT calculations suggest that the most stable configuration for the interfacial oxygen is in the 3-fold coordination. Furthermore, it was found that while this oxide phase readily grew into thicker 3-dimensional MoO₂ single crystalline thin films, only the surface oxide was stable up to 1000

°C in UHV. This indicates that there is an increase in thermodynamic stability given by the adhesion energy. The origin of this strong adhesion between the film and substrate can be related to the charge redistribution at the interface. An electron density difference map of the interface was used to illustrate the charge redistribution for this system. Furthermore, we employed DFT calculations to estimate the work of adhesion for this system and there is indeed a strong interaction between the film and substrate as expected. The calculated work of adhesion around 7 J / m^2 .

After continuing to anneal this surface at $900 \text{ }^\circ\text{C}$ and 1×10^{-6} Torr oxygen, MoO_2 nanowires begin to form. These wires grow at a constant rate until a maximum size of $\sim 30 \text{ nm}$ by $\sim 6 \text{ nm}$ is reached. Through the use of LEED, AES, STM and DFT we have fully characterised the growth of these wires. The general idea is that the initial MoO_2 (010) layer is close enough to the interface such that a charge redistribution at the interface can sufficiently modify the surface charge density and stabilize the film. This effect is such that the film fully wets the substrate. As the oxide grows thicker however, this (010) oxide surface orientation is classified as a polar, Tasker type III, surface and requires a surface modification to be energetically favourable.

As this film continues to grow it develops various sizes of nanowires and eventually develops into a periodically faceted surface made of MoO_2 (0 2 1) and (0 2 -1) faces. Employing ab-initio calculations, we show that this faceted surface has a lower surface free energy than the initial growth orientation. Furthermore, with the theory of periodically faceted surfaces, we showed that it is likely that the periodicity of the facets is D_{min} for this surface.

We have shown that the oxidation rate of MoO_2 on $\text{Mo}(110)$ under

these conditions follows a linear curve. With the use of the theories of oxidation we have shown that this linear rate is most likely related to the rate of adsorption or dissociation of oxygen at the surface of the oxide.

Furthermore, we have shown that magnetron sputtered Mo(110) thin films grown on Al_2O_3 can be of high quality. These films show promise for the production of MoO_2 nanowires on an insulating substrate.

10.2 Future Work

Growth rate vs. pressure measurements need to be made in order to conclusively say that the oxide growth rate is limited by oxygen adsorption. From this, we can determine the oxygen sticking coefficient for MoO_2 (021) at this temperature.

Further work is needed to produce high quality nanowires on Al_2O_3 . Furthermore, it needs to be determined whether the nanowires survive in ambient. If necessary a capping layer might be required to protect the wires.

Other metals such as V(110) need to be tested to investigate if this growth mechanism is more general or specific to the Mo(110) surface.

Appendix

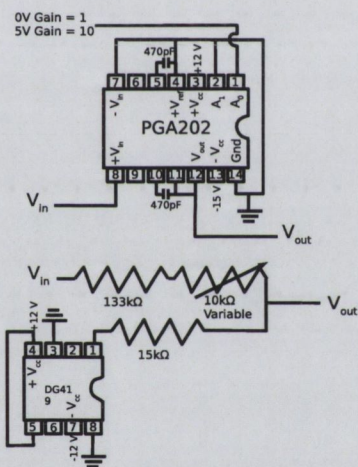


Fig. 1: Circuit diagram of the inline box to switch the STM current gain by 10 and divide the tunneling bias by 1/10.

List of Publications and Patents

K. Radican, N. Berdunov, and I. V. Shvets. Studies of the periodic faceting of epitaxial molybdenum oxide grown on Mo(110) Phys. Rev. B 77, 085417 2008.

S. Murphy, K. Radican, I. V. Shvets, A. N. Chaika, V. N. Semenov, S. S. Nazin, and S. I. Bozhko. *Asymmetry effects in atomically resolved STM images of Cu(014)O and W(100)O surfaces measured with MnNi tips.* Phys. Rev. B 76, 245423 2007.

A. N. Chaika, V. N. Semenov, S. S. Nazin, S. I. Bozhko, S. Murphy, K. Radican, I. V. Shvets. *Atomic row doubling in the STM images of Cu(014)O obtained with MnNi tips.* Phys. Rev. Lett. 98, (20), 206101, 2007.

K. Radican, N. Berdunov, I. V. Shvets. *Epitaxial molybdenum oxide grown on Mo(110): LEED, STM, and density functional theory calculations.* Phys. Rev. B 75, (15), 2007.

K. Radican, N. Berdunov, I. V. Shvets, S. Murphy. Patent Number: WO2006125826A1. *Nanowire assembly for electronic switching device including transistor, preferably field effect transistor, comprises substrate having oxidized surface forming nanotrenches with peaks and troughs, and conducting nanowires.*